UNIVERSIDAD DE VALENCIA
Departamento de Física Aplicada y Electromagnetismo

# Optical properties of III-V nanowires and their application for charge transport and single-photon emission

By

Michael Möller

Supervised by:

Andrés Cantarero Sáez
Mauricio Morais de Lima, Jr.

VALENCIA
July 2012

PROGRAMA DE DOCTORAT EN NANOCIÈNCIA I NANOTECNOLOGIA

*no pain, no gain*

# Contents

# 1. Introduction

Semiconducting nanowires are attracting considerable attention due to their promising potential as building blocks for advanced electronic and optoelectronic devices [1]. Nanowires can be described as nanostructures with tiny diameters (up to hundreds of nanometers) and a high length to diameter aspect ratio. They are often referred to as one-dimensional nanostructures, which can exhibit particular properties like surface related effects or quantum confinement effects [2]. They have been proposed for a wide range of applications varying from interconnects to active device elements. Due to advances in growth and fabrication methodologies, nanowires can be grown in very controlled manners which opens up new opportunities towards understanding and utilizing the unique physical properties of these low-dimensional systems.

In nanowire photodetectors, for example, one can take advantage of the large surface-to-volume ratio of nanowires. Since in semiconductors the atoms are mostly covalently bonded, the surfaces exhibit various dangling bonds – unsatisfied, “free” atom bonds – whose energy states often lie within the semiconductor band gap. For high surface state densities within the gap, the Fermi level gets pinned by the surface states, which leads to a band bending and in most cases to a depletion layer at the surface that separates electrons and holes spatially from each other [3, 4]. This prevents their recombination and enhances the photocarrier lifetime leading to a photoconductive gain, which is very suitable for photosensing applications and enables the design of novel photodetector architectures. Nanowires have been used as well as bridging wires in field-effect transistors (FETs) that connect to larger scale metalization [5] and have been seen as potential alternatives to planar metal-oxide semiconductor FETs [6]. In addition, nanowire-based FETs were utilized for electrical detection of single viruses [7] and for chemical and gas sensors [8, 9]. Further applications of nanowires have been realized in light-emitting diodes (LEDs) [10, 11], lasers [12], solar cells [13, 14] and logic gates [15].

In the last two decades, large research efforts have been made to control size, shape and composition of nanowires [16] which define and enable control over physical properties of the resulting material [17]. The size of nanowires affects strongly their physical properties. If the diameter of the nanowires becomes smaller than the exciton Bohr radius, the electron motion becomes limited and quantum confinement effects occur. These effects alter the optical and electronic properties of the nanowires. In the case of InP [18] and GaAs [19] nanowires, for example, a clear blue-shift of the photoluminescence (PL) with diameters smaller than 20 nm has been observed. This is due to the quantum confinement which leads to quantized energy states and results in an increase of the band gap energy. More recently, it has been reported that sub-5 nm Si nanowire FETs show an increased hole mobility due to quantum confinement that enhances the performance of the device [20, 21]. Besides, drastic effects on the optical properties of semiconductor nanowires already occur for diameters much less than the electromagnetic wavelength (e.g. $< 100$ nm for visible, infrared and microwave spectra). Due to dielectric mismatches between the dielectric permittivity of the nanowire material and its surrounding (mostly air), light becomes polarized inside the nanowire along the axis which leads to a polarization anisotropy of the absorption and emission in nanowires [22].

Furthermore, it has been shown that the shape of the nanowires has an influence on their optical properties. For different cross-sections of nanowires, a shift of phonon modes [23] and a change of the surface optical (SO) phonon dispersion [24] have been reported.

The control of the composition opens a wide range of future optoelectronic applications. Ternary alloys, for example, offer the advantage of the ability to tune the band gap energy by adjusting the relative composition of the alloy. The potential of this tuning, first observed in bulk, can be applied as well in nanowires and has been shown for single-crystalline $In_xGa_{1-x}N$ nanowires where the composition has been controlled for the entire range from $x = 0$ to 1. The latter leads to a tunable emission from the near-ultraviolet to the near-infrared region [25], thus making them suitable for solid-state lighting and photovoltaics.

In addition, controlling the nanowire composition enables the growth of nanowire heterostructures. The control over axial and lateral growth allows the fabrication of axial and radial heterostructures; the latter are as well related to as *core/shell* nanowires. Recently, a lot of attention has been attracted to axial and radial quantum well structures, superlattices or axial single quantum dot structures formed within nanowires. In the case of radial nanowire heterostructures, the controlled growth of one or more shells can passivate existing surface states or enable the nanowires for electronic or photonic devices. The passivation of surface states has been observed, for example, in GaAs/AlGaAs core/shell nanowires, where the optical absorption and PL emission efficiency from the GaAs core is strongly enhanced compared to bare GaAs nanowires [26, 27], making them suitable for optoelectronic devices such as solar cells or photodetectors [28]. Furthermore, radial heterostructure nanowires have shown high carrier mobilities in comparison with their corresponding bulk counterparts. In InAs/InP core/shell nanowires the electron mobility has been significantly increased compared to InAs nanowire FETs [29] and in Si/Ge core/shell nanowires utilized in FETs, an substantial enhancement of the hole mobility compared to Si FETs has been reported [6, 30]. Further applications in devices have been achieved with core/multishell nanowires which have been integrated in LEDs [31] and used for lasing [32].

Axial heterostructures play an important role in future semiconductor devices due to the possibility to integrate heterostructures with rather large lattice mismatches [33, 34] and to form abrupt and structurally perfect heterojunctions [35, 36]. The latter has a large impact on the electrical and optical properties of the nanowire since defects, dislocations, cracks or stacking faults often act as nonradiative recombination centers or electrical shorts. In addition, high potential for optoelectronic devices has been attributed to the growth of nanowires with embedded heterostructure quantum dots. The axial geometry allows for controllable injection of electrons and holes into the precisely defined active region with the additional advantage of high light-extraction efficiency since the optically active region is not embedded in a high refractive index material and the nanowire can act as a waveguide for the quantum dot emission [37]. Recently, such quantum dot structures have been utilized for the emission of single-photons offering novel opportunities for the development of tunable and efficient single-photon sources [38–40].

Besides the several efforts in semiconductor nanowire growth mentioned so far, another striking advantage is the possibility of epitaxial growth of nanowires with wurtzite or zincblende structure, or a combination of both (e.g. ideally zincblende/wurtzite superlattices, wurtzite/zincblende/wurtzite quantum well structures or crystal phase quantum dots in nanowires). Most bulk III-V semiconductors crystallize either in the cubic zincblende structure (phosphides, arsenides and antimonides) or in the hexagonal wurtzite phase (nitrides). However, it has been shown that nanowires can exhibit a different crystal structure than its bulk counterpart [41–46]. The transition between both phases corresponds to a modification in the stacking sequence along the direction of one of the bonds (the [111] direction in the case of the zinc-blende structure or the [0001] direction in the wurtzite structure). The change in crystal structure alters the optical and electronic properties of the material and results in different fundamental physical parameters such as the band gap energy, exciton binding energy and phonon energies. As a consequence of the novelty brought by the nanowire growth, even for GaAs, which is among the most well-known materials, an ample controversy regarding the band gap energy of the wurtzite structure still exists. While some authors have reported that the band gap of the GaAs wurtzite structure is larger than that of the zincblende one [47–53], others have claimed that the wurtzite band gap is lower or at the same level [54–58]. In the case of InAs – whose electronic and optical properties are studied in this work – much less information is available and scarce experimental data about the wurtzite band gap [59, 60] and wurtzite phonon energies [61] have been published.

Among the III-V compounds, GaAs and InAs nanowires have emerged as promising candidates for optoelectronic device applications. These materials have direct band gaps and high electron mobilities [62]. The GaAs material system is currently of great importance in the electronics and optoelectronics industries, and accordingly, GaAs nanowires are prime candidates for electrically and optically active nanowire devices [63]. InAs features a very high electron mobility and a small electron effective mass [64], which are particularly convenient for high-frequency electronic applications [2].

This work covers the optical characterization of III-V semiconductor nanowires and their application for charge transport and for single-photon emission. InAs nanowires have been investigated by Raman scattering and PL spectroscopy. The possibility to grow nanowires with a crystal structure different from its bulk counterpart has aroused a lot of interest in their optical and electronic properties. Here, the optical phonon modes of wurtzite InAs nanowires have been studied by polarized Raman scattering. For the first time, Raman measurements on a single InAs nanowire have revealed the $A_1$(TO) and $E_2^{H}$ optical phonon modes of the wurtzite structure. Additional resonant Raman scattering experiments have shown that the electronic $E_1^{G}$ transition in the wurtzite structure (close to the A point along the [0001] direction) is approximately 100 meV smaller than that for the zincblende phase (near the L point along the [111] direction). PL measurements of InAs ensembles have shown that the band gap of wurtzite InAs nanowires is substantially larger than the zincblende bulk band gap (0.415 eV) and a lower bound for the wurtzite gap has been estimated (0.458 eV). The measurements are in good agreement with available theoretical studies [47, 48, 54]. Experimental works obtained by extrapolating photocurrent measurements on $InAs_{1-x}P_x$ nanowires [59] and carried out on 2-dimensional wurtzite structures [60] suggest values of 0.54 eV and 0.52 eV, respectively. A more recent work on predominant zincblende InAs nanowires indicates a wurtzite band gap of 0.50 eV [65]. However, to the author's knowledge no band gap value on pure wurtzite nanowires has been published so far.

In order to demonstrate the potential of nanowires in optoelectronic devices, GaAs/AlGaAs core/shell nanowires have been used for the acoustic transport of photoexcited carriers along the nanowire axis. In contrast to InAs, the advantages of this highly investigated GaAs/AlGaAs nanowires are the optical emission in the near infrared region – where optical detection is more efficient – and the high PL emission efficiency [26, 27].

The acoustic transport has been realized by surface acoustic waves (SAWs). These waves, also known as *elastic surface waves*, were first described theoretically by Lord Rayleigh in 1885 [66]. A particular type of these SAWs is the *Rayleigh wave*, named after his discoverer, which has been applied in this work. Rayleigh SAWs are localized near the surface and consist of the superposition of a longitudinal acoustic mode polarized parallel to the propagation direction and a transversal mode polarized perpendicular to the surface. This leads to alternating regions of tensile and compressive strain along the propagation direction. Due to the strain and its corresponding piezoelectric potential, a dynamic type-II modulation of the electronic band edges is imposed that can be used to transport carriers at the velocity of sound in quantum well structures [67–69].

These SAWs have been applied to GaAs/AlGaAs core/shell nanowires transferred to a $LiNbO_3$ substrate in order to transport photoexcited carriers along the nanowire axis to a second location, leading to remote emission of sub-nanosecond light pulses synchronized with the SAW phase. The high-frequency contactless manipulation of carriers by SAWs opens new perspectives for applications of nanowires in optoelectronic devices operating at GHz frequencies. The potential of this approach is demonstrated by the realization of a high-frequency source of anti-bunched photons based on the acoustic transport of electrons and holes in (In,Ga)As/GaAs axial nanowires with AlGaAs shell.

The thesis is organized as follows: Chapter 2 reviews basic concepts of epitaxial growth and fundamentals of nanowire growth. Then, the crystal structure of nanowires and the different samples investigated in this work are addressed.

Chapter 3 describes the different used experimental characterization techniques. Firstly, Raman scattering is reviewed theoretically and the application of resonant and polarized Raman scattering and the used setup are introduced. Raman scattering is a powerful nondestructive tool that enables the investigation of structural, optical and electronic properties of nanowires. Secondly, PL spectroscopy and the principal optical transitions, the polarization anisotropy of the absorption and the emission of semiconductor nanowires and the setups utilized for the different measurements are addressed. Finally, the emission of single-photons is reviewed and the Hanbury Brown and Twiss setup is described.

Chapter 4 presents the Raman scattering on single InAs nanowires and the PL results on different InAs nanowire ensembles. Optical wurtzite phonon modes are identified and compared with theory. The electronic $E_1^{\mathrm{G}}$ transition and a lower bound for the wurtzite band gap are determined and discussed.

Chapter 5 exhibits the acoustic carrier transport in single nanowires. The PL results on GaAs nanowires are presented and the transport of photoexcited charge carriers by the oscillating piezoelectric field of a SAW is demonstrated. Time-resolved PL measurements reveal the PL dynamics of the transport process. Polarized PL has been used to address the linear polarization characteristics of the photoexcited carriers along the nanowire. In addition, the question whether optically generated electron spins can be maintained during transport is faced. Finally, the results of the PL measurements and the acoustic carrier transport in (In,Ga)As/GaAs nanowires are presented.

Chapter 6 presents the photon autocorrelation measurements on GaAs/AlGaAs and [(In,Ga)As/GaAs]/AlGaAs core/shell nanowires and demonstrates the realization of a high-frequency source for antibunched photons based on the acoustic transport in (In,Ga)As/GaAs nanowires.

In the final chapter, the conclusions of the work are drawn.

# 2. Synthesis and structure of III-V semiconductor nanowires

The growth of nanowires with perfect crystal structure, well-defined composition and size poses still a challenge in order to make complete use of the beneficial properties of nanowires in electronic and optoelectronic devices. As will be seen later, a change in crystal structure has significant effects on the physical properties of the nanowire. In particular, it will be addressed the wurtzite and zincblende crystal structure of III-V semiconductors, present in the nanowires investigated in this work.

In the next two sections, basic concepts of epitaxial and nanowire growth are reviewed which, in parts, have been taken from the work of K. Dick [2]. Then, the different crystal structures, formed during nanowire growth, and the investigated samples are described.

## 2.1. Basic concepts of epitaxial growth

Before discussing the main growth mechanism of nanowires, some basic concepts of epitaxial growth are presented. Epitaxy describes a form of crystal growth in which the growing crystal takes the crystallographic orientation of the underlying substrate. Common methods are the deposition of gaseous or liquid materials on an appropriate substrate to grow a monocrystalline structure. For vapor phase growth, a constant flux of the desired material is provided continuously to the substrate. The partial pressures of the materials create a constant chemical potential difference on top of the substrate, which acts as the driving force for the deposition, whereas in the liquid phase a gradient in concentrations of the materials generates the difference.

The most common growth technique for nanowires is the vapor phase based epitaxy (VPE). Here, the precipitation takes place from a supersaturated vapor phase. This vapor consists of the pure material or chemical precursors covering a wide range of possible materials. Moreover, the vapor can be continuously replenished turning it into a very common method nowadays [2]. A subtype of this method is the metal organic vapor phase epitaxy (MOVPE) where the precursors are individually provided to the substrate leading to controllable partial pressures of the materials and, therefore, to control of the growth and the stoichiometry. Since metal is often requested to be one of the components, it is provided in a metallorganic compound.

Molecular beam epitaxy (MBE) is a method that operates under (ultra-) high vacuum conditions. Here, the growth material is provided by molecular beams which are produced by evaporation of the material. This technique is characterized by its simplicity and high controllability, making it very useful for fundamental research. However, it requires materials which are liquid or solid in high vacuum and it is a considerably more expensive technique [2]. Chemical beam epitaxy (CBE) is a related technique where one or more beams contain precursor molecules, rather than elemental materials. For III-V semiconductor growth, generally metal-alkyls [e.g. TMIn (trimethylindium) and TEGa (triethylgallium)] and hydrids (e.g. arsine and phosphine) are used as group-III and group-V precursors, respectively.

## 2.2. Nanowire growth

In general, nanowire growth can be classified in two main categories: the *template-assisted* and the *free-standing* one. In template-assisted growth, a pre-defined crystal is formed which consists of an (ordered) nanopore array in order to suppress growth in other directions. This is followed by a filling of these nanopores to grow the nanowire with the selected material [Fig. 2.1(a)]. An alternative type of this growth technique is the growth along the length of the template, as in the v-groove templated technique [Fig. 2.1(b)] [2]. These techniques make use of existing lithographic technologies which provide a high pattern control but also limit the size of the template. A common method to fabricate template-assisted nanowires is the electrochemical synthesis where a radiation track-etched polycarbonate membrane or an anodized alumina membrane with nanopores is used as templates for the chemical or electrochemical deposition of the nanowire material inside the pores of the template [70, 71]. In general, this method is applicable to electrical conductive materials such as metals, alloys, semiconductors, and electrically conductive polymers and oxides [70]. However, the nanowires mostly are not grown epitaxially leading to amorphous or polycrystalline structures with a lot of defects that may limit their technical applications [71].

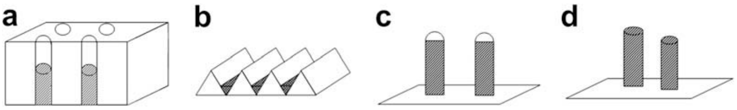

***Figure 2.1.:*** Nanowire growth techniques. (a) Template-assisted nanowire growth. (b) V-groove template-assisted growth. (c) Particle-assisted free-standing nanowire growth. (d) Particle-free free-standing growth. (taken from Ref. [2]).

The growth of free-standing nanowires is normally achieved by means of small metal seed particles (usually gold, Au) [Fig. 2.1(c)]. These particles act as catalysts for the nanowire growth and are normally not consumed during the growth process, although they can be unintentionally incorporated into the nanowire leading to impurities in the pure crystalline structure. This method, first demonstrated in the 1960s by WAGNER AND ELLIS [72], is based on the so called *vapor-liquid-solid* (VLS) mechanism, so called because they used the gaseous precursor $SiCl_4$ and a melted liquid gold-silicon (Au-Si) alloy droplet to form the one-dimensional solid Si-nanowire by precipitation of Si from the droplet. The VLS mechanism – the most commonly used growth mechanism for semiconductor nanowires nowadays – is discussed in more detail in the next subsection. Alternatively, it has been shown in the last few years, that free-standing III-V nanowires can be grown without using foreign seed particles (e.g. in InP [73], InAs [74, 75] and GaAs [76] nanowires)[Fig. 2.1(d)]. Instead, the group-III constituent of the wire material acts as the catalytic droplet. The advantage over the catalyst-assisted method is the avoided contamination of the nanowire from the catalyst to obtain defect-free high purity nanowires [77]. However, the growth behavior of the catalyst-free nanowires is not yet clear [76] and is still under debate.

### VLS growth

Since the first description of the VLS mechanism in 1964 by Wagner and Ellis, the technique has been expanded to fabricate a variety of pure and doped nanowires which include elemental semiconductors, II-VI semiconductors, III-V semiconductors, oxides, nitrides and carbides [78, 79]. The VLS process can be divided in two main steps: 1) the formation of liquid droplets acting as catalysts and 2) the alloying, the nucleation and the growth of the nanowires [71].

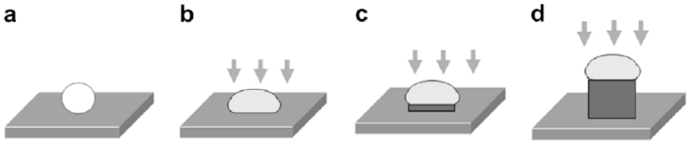

***Figure 2.2.:*** Particle-assisted nanowire growth process. (a) Deposition of solid metal seed particles. (b) Melting of the solid particle and incorporation of supplied nanowire material. (c) Nucleation occurs when supersaturation is reached. (d) nanowire growth occurs at particle-wire interface (taken from Ref. [2]).

First, small metal particles are deposited on a substrate to initiate the growth process [Fig. 2.2(a)]. In this step, it is possible to control the size and the position of the catalytic particle for patterned nanowire growth [71], whereas the size of the catalyst defines the width of the nanowire [80]. After depositing the metal catalyst, a suitable temperature above the eutectic point of the system is chosen according to the binary phase diagram (Fig. 2.3) between the metal and the target material [71].

Second, a gas that contains the growth material is brought in contact with the melted droplet [Fig. 2.2(b)] using techniques like CBE [81], MBE [82], chemical vapor deposition (CVD) [83], laser ablation [84] or MOVPE [85]. Since the sticking coefficient of the liquid droplet surface is higher than the one of the solid substrate, the precursor gas prefers to precipitate at the catalyst surface forming an alloy. The continuing feeding of the catalyst particle yields a supersaturation of the droplet which leads to nucleation of the nanowire material [Fig. 2.2(c)], where the liquid-solid interface acts as a sink causing the continued material incorporation into the lattice and, thereby, the growth of the nanowire with the droplet riding on top [86] [Fig. 2.2(d)]. For this reaction, the difference in the chemical potential of the components is the driving force.

The chemical potentials for the reactants have to be greater than the products, i.e. a supersaturation must exist. If the difference vanishes, the reaction stops and no further growth occurs. Therefore, it is important to maintain a constant flux of the gaseous reactants in order to provide a continuously steady-state nanowire growth [86]. In Fig. 2.3, this process can be illustrated for a simplified binary case where A denominates the metal catalyst droplet (e.g. Au) and B the nanowire material (e.g. Si). Heating the droplet slightly above the eutectic temperature $T_E$, the system will reside in the region "liquid + solid A" (a). After feeding the droplet with reactants the system moves to a more liquid state [(a) → (b)] and a further increase of the amount of reactants in the vapor near the catalyst particle increments the dissolution into the alloy until the composition reaches the *liquidus* line (b). Beyond that point, further feeding of the alloy (if the reactant concentration outside of the droplet is still higher than inside the particle) will lead to an unstable situation yielding to precipitation of the nanowire material in order to re-establish the stable local composition between the metal and the nanowire material (c). In 2001, WU AND YANG observed for the first time the VLS nanowire growth of the Au-Ge system in an in-situ high-temperature transmission electron microscope (TEM) where they could identify the different stages of the growing process (Fig. 2.4) [87].

However, the growth of compound nanowires is more complicated and more difficult to understand. If, for example, III-V semiconductor nanowires are considered, it has to be provided both the group-III and the group-V material in the vapor phase. The difference in the chemical potential is determined by both materials of the compound and, in addition, the ratio of the materials influences the growth [2]. Furthermore, it has been shown that generally just the group-III particles dissolve in significant quantities in the metal droplet [88], whereas the group-V particles have to precipitate on the side facets of the nanowire or the substrate and diffuse to the growth interface [2]; however, for Sb-based materials Au can alloy with both components.

Although the phase diagram for more complex systems is generally more difficult, it has been shown that for GaAs it can be simplified by considering the pseudobinary phase diagram between the metal catalyst (A) and the compound solid material (B) [84].

Beside the VLS technique to grow nanostructures, there are several

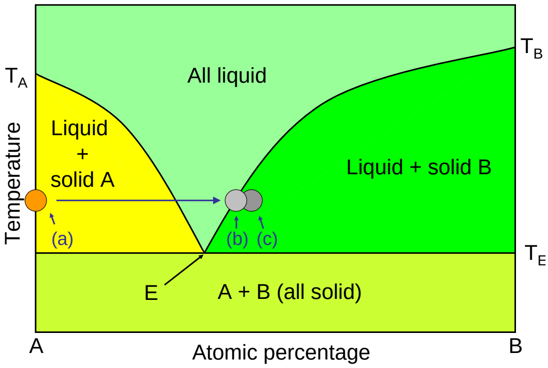

***Figure 2.3.:*** Simple binary phase diagram. The components of the system are A and B. The possible phases in this system are solid A, solid B and a liquid with a composition ranging between pure A and pure B. The compositions are given in $x$-coordinates, ranging from pure A on the left to pure B on the right hand side. The curves separating the region "All liquid" from the regions "Liquid + solid A/B" are called *liquidus*, whereas the separating line between the last mentioned region and "A + B" is named *solidus*. The indicated point E marks the eutectic point of the system where all three phases coexist in equilibrium. The corresponding eutectic temperature is labeled as $T_E$ and the melting temperatures of pure A and B as $T_A$ and $T_B$, respectively. This figure is adapted from Ref. [2].

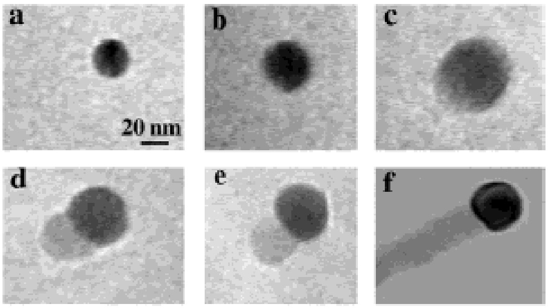

***Figure 2.4.:*** In-situ TEM images during the process of nanowire growth. (a) Au particles in solid state. (b) Alloying initiates. (c) Liquid Au-Ge alloy. (d) Nucleation of Ge on the alloy interface. (e)-(f) nanowire growth (taken from Ref. [87]).

other techniques available such as vapor-solid (VS) growth [89], oxide-assisted growth [90–92] and solution-liquid-solid (SLS) growth [93, 94].

## 2.3. Nanowire structures

In the previous sections, it has been described how nanowires can be grown by several techniques, while the present section addresses different nanowire structures that can be grown with these growth techniques.

First, it is worth to distinguish between axial and lateral growth of the nanowire. Since one is usually interested in a uniform nanowire with a high length to diameter ratio, one has to ensure that axial growth is strongly favored over lateral growth. For example, for III-V semiconductors it has been found that the morphology of the nanowire depends on the growth temperature and the V/III flux* which is applied to the growth system [95–97]. In the case of InAs nanowires grown by MBE [82], by MOVPE [98] or by CBE [99], a lower temperature results in tapered nanowires, whereas a higher temperature yields a more rod-like shape. This is explained by different diffusion lengths of the elements on the lateral nanowire facets [82], being smaller at low temperatures. When the nanowire length exceeds the diffusion length, the elements which impinge on the substrate or at the bottom end of the nanowire cannot reach anymore the catalyst leading to incorporation of the element on the side facets and, hence, to lateral growth. With higher temperature, on the other hand, the diffusion length increases and the nanowire takes a more rod-like shape.

The axial and lateral growth can be used to fabricate axial or radial nanowire heterostructures. The growth of axial nanowire heterostructures uses the concept of the above mentioned growth mechanisms. A switch between the source materials results in an axial heterostructure, for example InAs-InP heterostructures [100, 101]. Radial heterostructures can be fabricated by coating nanowires with a conformal layer of a second material; these core/shell structures, e.g. Ge/Si [86], can be obtained if the vapor deposition/adsorption of the reactants of the second material

---

*The V/III flux denominates the ratio between the group-V and the group-III elements or precursors which contain these elements depending on which growth technique is used. This defines the partial pressures of the respective elements in the system.

continues at the surface of the nanowire (whereas, if the decomposition takes place at the catalyst, the resulting structure is axial).

Moreover, different structures can be achieved within the same material. In the next section the zincblende and the wurtzite structure, the most important crystal phases for various III-V semiconductor materials, are described.

### The wurtzite and the zincblende structure

The feasibility to grow nanowires with different crystal structures has attracted a lot of attention since a change in crystal structure provides the possibility to alter optical and electronic properties within the same material. This work focuses on the cubic (zincblende) and hexagonal (wurtzite) crystal phases since these are the two common polytypes occurring in III-V nanowires at ambient pressure. In Ch. 4, the optical and electronic properties of InAs nanowires with zincblende and wurtzite phases will be investigated and in Ch. 5 it will be seen how the acoustic transport of photoexcited carriers is affected by the crystal structure of GaAs nanowires.

If III-V semiconductor bulk material is considered under normal conditions, it can be observed that some semiconductors crystallize in the wurtzite structure (GaN, AlN, etc.), whereas others crystallize in the zincblende phase (InAs, InP, GaAs, etc.). The structures are very similar and consist of atoms with four tetrahedral bonds. The sequence how these atoms are connected to each other defines their symmetry and, hence, their physical properties. The symmetry of the cubic zincblende structure is given by the space group $T_d^2$ and can be illustrated by two interpenetrating face-centered-cubic (fcc) sublattices displaced from each other by (1/4, 1/4, 1/4)$a$ where $a$ is the cube edge length or the lattice constant. Both sublattices are occupied each by one atomic species which results in two atoms per unit cell.

The hexagonal wurtzite structure belongs to the space group $C_{6v}^4$ and is constituted by two interlocking closed-packed-hexagonal (hcp) Bravais lattices. In this case, the unit cell consists of four atoms. The difference between these structures becomes apparent if one considers the second nearest neighbors. Figure 2.5 shows the stacking sequences of InAs bilayers along the [111] growth direction in zincblende (a) and along

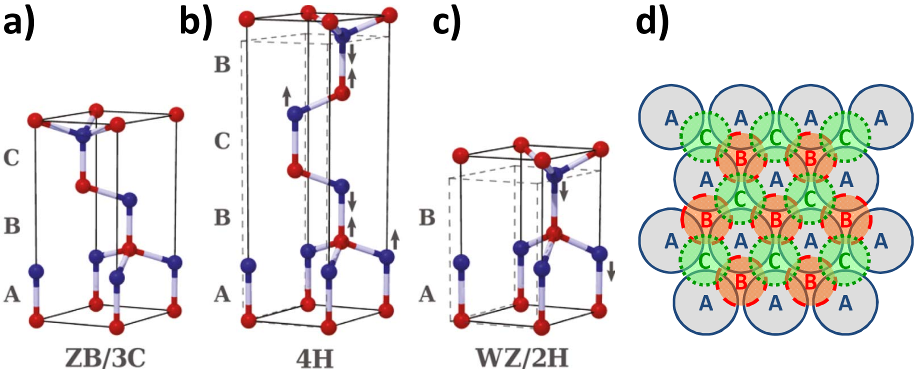

***Figure 2.5.:*** Different crystal structures for III-V nanowires. (a) Zincblende phase with ABCABC layer stacking in [111] direction leading to cubic crystal structure (3C). (b) 4H hexagonal polytype structure with ABCBABCB stacking sequence. (c) Wurtzite phase with ABAB layer stacking oriented in [0001] direction yielding a hexagonal crystal structure (2H). The structures are shown in comparison to the ideal cell constructed from the cubic lattice constant (dashed lines). Red and blue atoms represent the group-III and group-V atoms, respectively {(a-c) taken from Ref. [102]}. (d) Schematic layer by layer growth. If the first layer occupies position A (grey circles), the second layer has the possibility to be placed on the "holes" from the first layer, either on position B (red circles) or C (green circles). The subsequent layer, then, can be set on the same position as the first one (A) or the hole position not occupied by the previous layer, etc.

the [0001] growth direction in wurtzite structure (c), respectively. For the zincblende structure the stacking sequence consists of repeating ABC layers (each containing a group-III and a group-V atomic layer) leading to cubic crystal structure [Fig. 2.5(a)]. However, if the stacking sequence alternates between A and B layers, the crystal structure is hexagonal wurtzite [Fig. 2.5(c)]. For a discrimination of both structures, one has to contemplate at least three layers since the first two layers can be equal in both phases. If the first layer is an A layer, the second can be a B or C layer, as schematically depicted in Fig. 2.5(d). The subsequent layer can be set on the same position as the first A layer (e.g. ABABAB) or at the position not occupied by the former two layers (e.g. ABCABC) and, thus, defines the type of crystal structure.

However, most nanowires do not have perfect crystal structure and possess some layers that differ from the predominant stacking sequence.

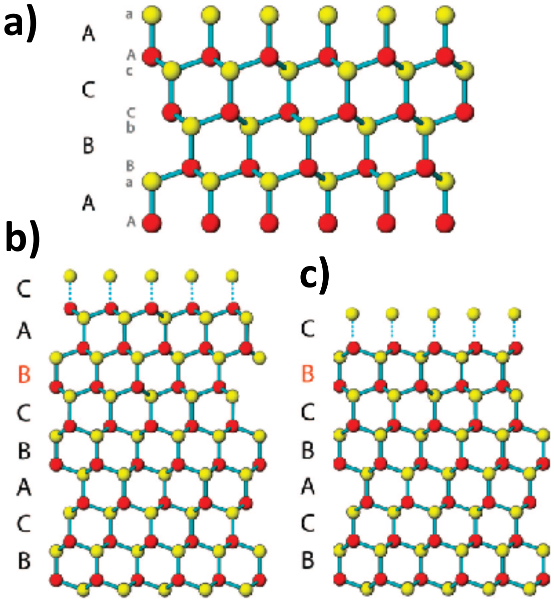

***Figure 2.6:*** Possible stacking sequences during nanowire growth. a) Cubic zincblende structure. In b) and c), the first fault plane on top of a zincblende region is indicated in red. If the stacking sequence continues with layer A and C (b), a twin segment is formed and the stacking sequence is mirrored around the C layer under the fault plane. If, on the other hand, another fault plane forms on the top of the red-marked B layer (c), wurtzite phase starts to form (taken from Ref. [103]).

If during growth a fault plane *B* occurs, for example in the zincblende structure ABC*B*, it depends on the successive layer whether the structure continues with the wurtzite structure (ABCBC) – i.e. with the creation of another fault plane – or whether a rotation or reflection of the original structure takes place (ABCBAC) – leading to a so-called *twin plane* – illustrated for nanowires in Fig. 2.6. In the former case, the layer stacking continues with the BC sequence and a change in crystal structure is observed while in the latter the zincblende structure is maintained and a stacking fault is inserted which represents a rotation of the crystal around the growth axis.

In addition to the wurtzite and zincblende phase, alternative repeating stacking sequences can occur in nanowire growth. These polytype structures are less common due to the difficulty of perfect polytype crystal growth. However, recently InAs nanowires have been grown with ABCBABCB stacking [see Fig. 2.5(b)] which enables the fabrication of polytypic heterostructures within the same material [102].

The reason why several nanowires exhibit polytypes or zincblende and wurtzite structure although the bulk material only exists in one phase under normal conditions is up to now not completely understood and still under debate in the literature. Nanowires usually contain a large number of stacking faults; however, in the case of certain well-defined growth conditions, a rather defect-free nanostructure can be formed [97, 104]. Glas et al. [105] suggest that the formation of wurtzite structure of III-V semiconductors, that crystallize in zincblende under normal conditions, depends on the interface energies of the different structures at the triple phase line (the boundary where the liquid nanoparticle, the solid nanowire and the vapor meet). Here, the wurtzite and zincblende structure present major differences due to their different geometries of side and top facets. In order to favor wurtzite phase growth, the energy barrier for nucleation of a wurtzite layer has to be lower than that of a zincblende one. A high supersaturation, for example, increases the difference of chemical potential from equilibrium and can overcome the energy barrier for nucleation of a wurtzite plane (which acts as a fault plane in zincblende bulk material) while low supersaturation favors the nucleation of zincblende structure [103]. For it, they assume that nucleation occurs at the triple phase line, as verified experimentally [104]. Further conditions to favor a specific structure are given by temperature [106], nanowire radii [105] and the step energies of materials – the energy difference between forming a fault plane instead of an ordinary plane according to the stacking sequence [103].

## 2.4. Nanowire samples

Regarding the specific nanowire samples investigated in this work, the growth processes and their characterization by electron microscopy are presented in the remaining part of this chapter.

### InAs nanowires

The growth of InAs nanowires were performed in the group of Mônica A. Cotta in Campinas, Brazil.[†] The nanowires have been grown with the VLS method in a CBE system using gold nanoparticles as catalysts which are dispersed in water. The nanoparticle water solution is cast on a GaAs(100)

---

[†] Owing to the collaboration with Fernando Iikawa, Thalita Chiaramonte and Mônica A. Cotta at the Physics Institute “Gleb Wataghin”, UNICAMP, Campinas, SP, Brazil.

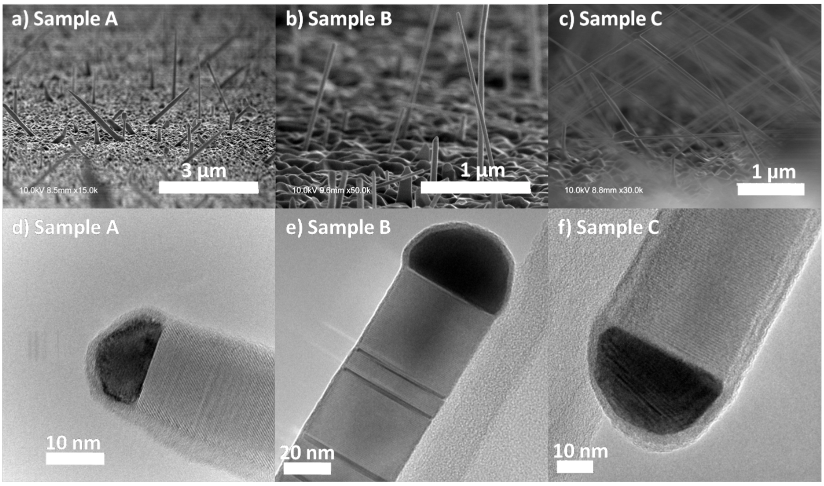

***Figure 2.7.:*** SEM images of InAs nanowires grown at (a) 420 °C, (b) 450 °C and (c) 480 °C. Corresponding TEM images of the sample A (d), sample B (e) and sample C (f).

substrate. After approximately 10 minutes the substrate is cleaned with deionized water. Growth precursors are trimethyl indium [TMI, $(CH_3)_3In$] with hydrogen ($H_2$) as carrier gas and thermally decomposed arsine ($AsH_3$) [99].

Three samples grown at different temperatures – 420 °C (sample A), 450 °C (sample B) and 480 °C (sample C) – have been analyzed. To characterize the nanowires, scanning electron microscopy (SEM) and transmission electron microscopy (TEM) studies have been performed.[‡] Typical images of the nanowires for the samples A, B and C are presented in Fig. 2.7. The nanowires of sample A show a needle-like shape [Fig. 2.7(a)] while the nanowires of samples B and C have a rod-like shape [Fig. 2.7(b) and (c)]. The average diameters of the nanowires are $103 \pm 22$ nm, $71 \pm 14$ nm and $51 \pm 18$ nm [see Fig. 2.8(a)] with average lengths of $1.5 \pm 0.5$ µm, $1.9 \pm 0.9$ µm and $3.4 \pm 2.9$ µm for sample A, B and C, respectively (a summary of the values is given in Tab. 2.1). The large variation of the length of sample C is due to the wide length/diameter distribution of nanowires from that sample, as can be seen in Fig. 2.8(b).

---

[‡] TEM studies have been performed by the group of Campinas, Brazil.

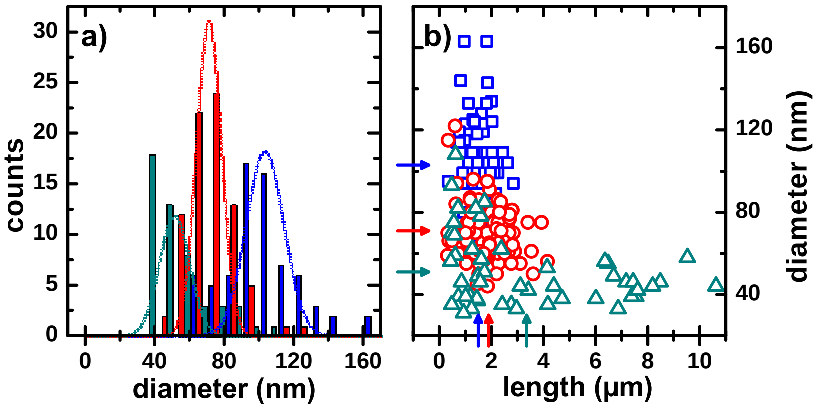

***Figure 2.8.:*** Statistics of nanowire dimensions for the InAs samples A (blue), B (red) and C (green). (a) Diameter distribution of the nanowire samples. The solid lines represent the corresponding Gaussian distribution. (b) Relation between nanowire length and diameter across the samples. Nanowires are short and thick for sample A and become longer and thinner when increasing the growth temperature (sample B). For sample C, the nanowires are in average very thin and long, but show the widest length/diameter distribution of all samples.

Some nanowires exhibit large diameters and short lengths and are comparable to the ones from sample A and B. Other nanowires, however, are very long and thin. Possible reasons for this may be unstable growth conditions such as a variation of the growth temperature or V/III flux or an unstable supersaturation. The TEM measurements [Figs. 2.7(d-f)] present nanowire examples with very thin diameters. In the case of sample A, the diameter close to the tip can be as small as 15 nm. The nanowires of all samples exhibit a predominantly wurtzite structure; in some cases the presence of zincblende stripes (stacking faults) has been observed. However, for a more precise and clear determination of the crystal structure of the nanowires across the samples, further TEM investigations have to be carried out. All nanowires were grown along the [0001] (wurtzite) and [111] (zincblende) direction, respectively.

In order to measure the Raman scattering of single nanowires, they have been mechanically transferred onto a GaAs substrate coated with a 1 µm thick Al film. The mechanic transfer consists of rubbing the sample against the substrate such that individual nanowires from the sample

| Samples | diameter | length | shape |
|---|---|---|---|
| Sample A | $103 \pm 22\,\mathrm{nm}$ | $1.5 \pm 0.5\,\mu\mathrm{m}$ | needle-like |
| Sample B | $71 \pm 14\,\mathrm{nm}$ | $1.9 \pm 0.9\,\mu\mathrm{m}$ | rod-like |
| Sample C | $51 \pm 18\,\mathrm{nm}$ | $3.4 \pm 2.9\,\mu\mathrm{m}$ | rod-like |

***Table 2.1.:*** Average diameter, length and shape of InAs nanowires from samples A, B and C.

break and fall onto the substrate. This technique has been used as well for the samples D and E (see below) in order to transfer nanowires onto a SAW delay line. The Al-coating of the substrate has been used to block the background of the GaAs bulk material in order to prevent the appearance of GaAs Raman modes.

### GaAs nanowires

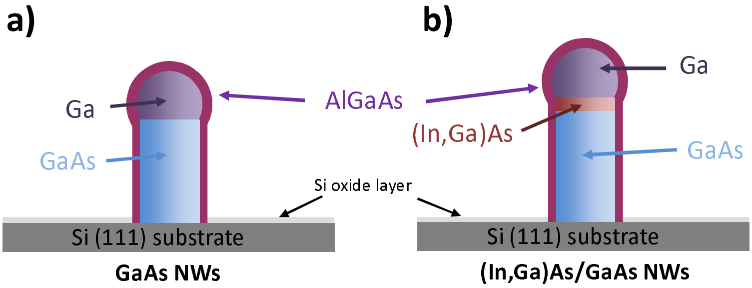

***Figure 2.9.:*** Schematic drawings of the (a) GaAs nanowires and (b) the (In,Ga)As/GaAs nanowires.

The growth of GaAs nanowires was performed by Steffen Breuer in the group of Lutz Geelhaar in Berlin, Germany.[§] A more extensive description and the suitability of the nanowires for optoelectronic devices are presented in detail in Ref. [107]. The nanowires were prepared on phosphorous-doped Si(111) ±1 ° substrates. The native substrate oxide was removed by HF, and the substrates were loaded into the preparation

---

[§] Owing to the collaboration with Paulo V. Santos at the *Paul-Drude-Institut für Festkörperelektronik*, Berlin, Germany.

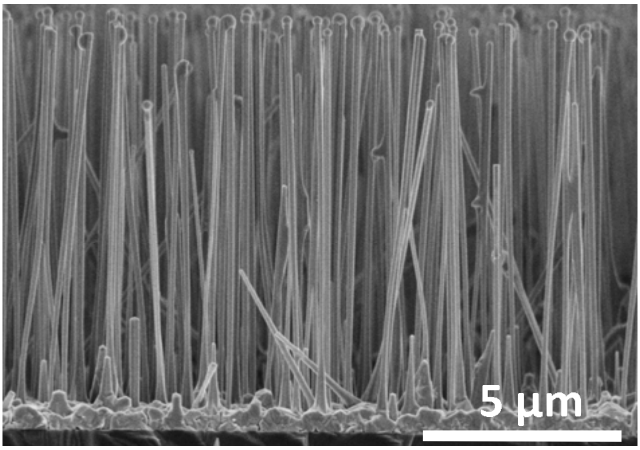

***Figure 2.10:*** SEM image of GaAs nanowires from sample D.

chamber for water desorption at 300 °C. In a MBE epitaxy system, the self-assisted VLS nanowires were grown for 1 h at 580 °C substrate temperature with an atomic flux ratio of $F_{\mathrm{As}}/F_{\mathrm{Ga}} = 1$. The atomic fluxes of Ga, Al, and As had been calibrated by reflection high-energy electron diffraction (RHEED) oscillations during GaAs(001) layer growth. After half the growth time, growth of the nominally $\mathrm{Al_{0.1}Ga_{0.9}As}$ shell was initiated by opening the Al shutter. The total volume was equivalent to a layer thickness of 866 nm. A schematic drawing of the nanowires is presented in Fig. 2.9(a).

The nanowires considered in this work (sample D) are $9 \pm 1$ µm long and consist of an undoped GaAs core of $106 \pm 18$ nm coated with a $22 \pm 9$ nm $\mathrm{Al_{0.1}Ga_{0.9}As}$ shell (see Figs. 2.10) [107]. For the acoustic transport studies, the nanowires were mechanically transferred onto the surface of a SAW delay line on a $\mathrm{LiNbO_3}$ crystal and measurements were performed on those nanowires which were incidentally aligned with the SAW propagation direction. These GaAs/AlGaAs core/shell nanowires are referred to as GaAs nanowires throughout the work.

### (In,Ga)As/GaAs nanowires

The InGaAs/GaAs nanowire growth were performed by Claudio Somaschini in the group of Lutz Geelhaar in Berlin, Germany. The GaAs nanowire cores were grown in the same manner as the former nanowires.

However, in the last steps of MBE deposition In and As fluxes are exposed (sample E). This leads to a formation of a short approximately 300 nm long section containing In inclusions [see Figs. 2.11(a) and (b)] which, in the following, is denoted as the (In,Ga)As section. Because of the modified MBE growth conditions, the (In,Ga)As segments have a larger diameter (200 nm) as well as a higher density of planar defects compared to sample D, as confirmed by TEM [Fig. 2.11(b)]. As for sample D, an $Al_{0.1}Ga_{0.9}As$ shell has been grown in the final step. The average length of the nanowires in this sample is approximately 7µm. A schematic drawing of these [(In,Ga)As/GaAs]/AlGaAs core/shell nanowires is displayed in Fig. 2.9(b). These nanowires are referred to as (In,Ga)As/GaAs nanowires throughout the work.

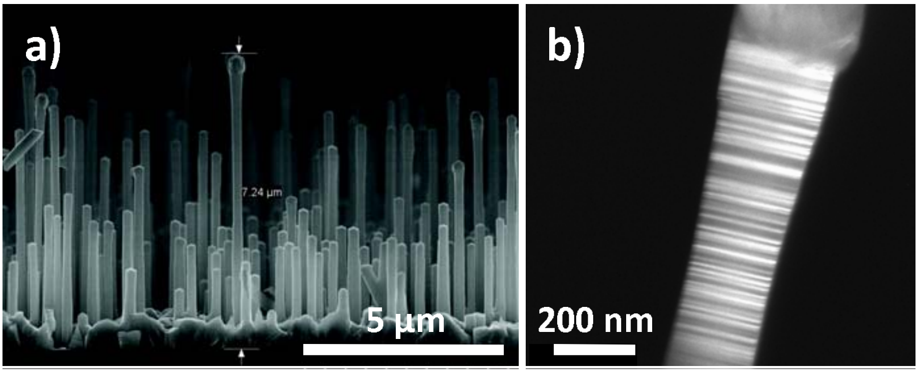

***Figure 2.11.:*** (a) SEM image of (In,Ga)As/GaAs nanowires of sample E. (b) TEM image of the segment close to the nanowire tip.

# 3. Characterization techniques

In this chapter, the different experimental techniques to characterize the optical and electronic properties of the investigated nanowires are described. The theoretical background is focused on the light-matter interaction which is the key aspect to understand the optical properties of the nanowires investigated in the next chapters. In the following sections, the inelastic scattering (e.g. Raman or Brillouin scattering) and the luminescence of a semiconductor are described.

In the first section, the Raman scattering process, the Raman selection rules for the zincblende and wurtzite structure and the used experimental setup are presented. The second section describes the PL spectroscopy, the linear polarization anisotropy of the absorption and emission of nanowires and the used experimental setups. Finally, the single photon emission, its detection and the Hanbury Brown and Twiss setup are described.

## 3.1. Raman spectroscopy

Raman scattering is a standard nondestructive contactless characterization technique that allows to investigate the structural, optical and electronic properties of a material. The technique is based on the inelastic scattering process of optical phonons during irradiation of materials, particularly solids. Similar techniques originating from elastic scattering processes and inelastic scattering of acoustic phonons are referred to as *Rayleigh scattering* and *Brillouin scattering*, respectively.

### 3.1.1. Theoretical aspects

In this section, the Raman scattering process will be considered theoretically. For simplicity a more qualitative description is presented which gives insight into the main relevant processes of Raman scattering for this work (such as polarization selection rules and resonance conditions) and follows roughly the book of Yu and Cardona [108] where a more detailed description can be found.

If the corresponding energies and momenta in the scattering process in a crystalline solid are taken into account, the following energy and quasi-momentum conservation laws hold:

$$\begin{aligned} \hbar\omega_{\mathrm{S}} &= \hbar\omega_{\mathrm{L}} \mp \hbar\omega_{\mathrm{p}}, && (3.1) \\ \hbar\boldsymbol{k}_{\mathrm{S}} &= \hbar\boldsymbol{k}_{\mathrm{L}} \mp \hbar\boldsymbol{k}_{\mathrm{p}}. && (3.2) \end{aligned}$$

Here, the indices denominate the scattered (S) and incident (L) light as well as the phonon (p) energy and momentum, respectively. The minus sign stands for those scattering processes in which a phonon is generated (*Stokes process*), whereas an annihilation of a phonon is described by the plus sign (*anti-Stokes process*). The two conservation laws state that only a certain combination of energy and momentum can be transferred to the sample. Assuming visible lasers as radiation sources, $k_{\mathrm{L}}$ is in the order of $10^6\,\mathrm{cm}^{-1}$. This is about one thousandth of the size of the Brillouin zone in a semiconductor. Hence, for first-order scattering by optical phonons the energy transfer $\hbar\omega_{\mathrm{p}}$ (also referred to as *Raman frequency* or *Raman shift*) is almost independent of the incident energy $\hbar\omega_{\mathrm{L}}$ since the phonon dispersion can be neglected near the center of the Brillouin zone. In this sense, first-order Raman scattering is sensitive to phonons at the $\Gamma$ point of the Brillouin zone.

To describe the Raman effect, it is considered an infinite medium with electric susceptibility $\chi(\omega_{\mathrm{L}})$ at laser frequency $\omega_{\mathrm{L}}$. In general, $\chi$ is a second rank tensor, but for simplicity the medium is assumed to be isotropic such that $\chi$ can be represented by a scalar. When a plane electromagnetic wave

$$E(t) = E_{\mathrm{L}} e^{-i\omega_{\mathrm{L}} t}$$

encounters this medium, a sinusoidal polarization will be induced:

$$P = \chi(\omega_{\mathrm{L}}) E_{\mathrm{L}} e^{-i\omega_{\mathrm{L}} t}. \tag{3.3}$$

Phonons, that are normal modes of atomic vibrations in a crystal, are quantized with wave vector $\boldsymbol{k}_{\mathrm{p}}$ and frequency $\omega_{\mathrm{p}}$. These atomic displacements $Q(t)$ modify the electric susceptibility. If the characteristic frequencies $\omega_{\mathrm{L}}$, which determine $\chi$, are much larger than $\omega_{\mathrm{p}}$, $\chi(\omega_{\mathrm{L}})$ can be expanded in power series of the phonon displacement $Q$. This is known as the quasi-static or adiabatic approximation [108]. Assuming a plane wave for $Q(t) = Q_0 e^{-i\omega_{\mathrm{p}} t}$ and keeping only the first-order terms, results in

$$\chi(\omega_{\mathrm{L}}, Q(t)) = \chi(\omega_{\mathrm{L}}) + \frac{d\chi(\omega_{\mathrm{L}})}{dQ} \cdot Q(t). \tag{3.4}$$

The first term on the right hand side denotes the susceptibility of the medium with no fluctuations, whereas the second term represents an oscillating susceptibility induced by the lattice wave $Q(t)$. Substituting Eq. 3.4 into Eq. 3.3, the induced polarization can be expressed as

$$P = \chi(\omega_{\mathrm{L}}) E_{\mathrm{L}} e^{-i\omega_{\mathrm{L}} t} + \frac{d\chi(\omega_{\mathrm{L}})}{dQ} \cdot E_{\mathrm{L}} e^{-i(\omega_{\mathrm{L}} \mp \omega_{\mathrm{p}})t} \cdot Q_0. \tag{3.5}$$

In this equation, the first term corresponds to the polarization vibrating in phase with the incident light, i.e. the term is responsible for elastic light scattering. The second term denotes a polarization varying with $(\omega_{\mathrm{L}} \mp \omega_{\mathrm{p}})t$, an induced oscillation which generates dipole radiation at the Stokes and anti-Stokes frequencies.[*]

So far, $\chi$ and $d\chi/dQ$ have been handled as scalars, but in general they are tensors. If one assumes that $\boldsymbol{Q}$ is the vector displacement of a given atom induced by the phonon and $\hat{\boldsymbol{Q}} = \boldsymbol{Q}/|\boldsymbol{Q}|$ is a unit vector parallel to the phonon displacement, then one can define a second rank tensor [108]

$$\boldsymbol{R} = (d\chi/d\boldsymbol{Q})\hat{\boldsymbol{Q}}. \tag{3.6}$$

$\boldsymbol{R}$ is known as the *Raman tensor*. The intensity of the scattered radiation can be calculated from the time-averaged power radiated by the induced polarizations (second term on the right hand side of Eq. 3.5) into the solid angle. This scattered intensity $I_{\mathrm{S}}$ is proportional to [109]

$$I_{\mathrm{S}} \propto \omega_{\mathrm{S}}^4 \, |\hat{e}_{\mathrm{L}} \cdot \boldsymbol{R} \cdot \hat{e}_{\mathrm{S}}|^2 \tag{3.7}$$

where $\hat{e}_{\mathrm{L}}$ and $\hat{e}_{\mathrm{S}}$ denote the polarization of the incident and scattered radiation, respectively. It is worth noting that in Eq. 3.7 the scattered

---

[*] The expansion to higher terms in Eq. 3.4 induces polarizations at higher frequencies giving rise to second order Raman scattering or Raman overtones. Actually, the Stokes term must be multiplied by a factor $n_p + 1$ and the anti-Stokes by $n_p$. These factors can only be obtained from a quantum-mechanical treatment of the light scattering process.

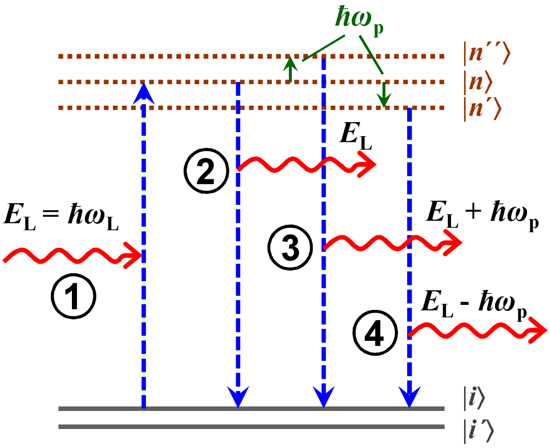

***Figure 3.1:*** Energy level diagram for a Raman process. In a first step (1), the system in the ground state $|i\rangle$ is excited to an intermediate state $|n\rangle$ under absorption of a photon with energy $\hbar\omega_L$. An electron-hole pair is generated which recombines (2) with emission of a photon (Rayleigh). In the Raman scattering process the electron-hole pair (1) is scattered to another state $|n''\rangle$ (3) or $|n'\rangle$ (4) under annihilation (Stokes) or creation (anti-Stokes) of a phonon with energy $\hbar\omega_p$. Subsequent recombination from the excited states leads to the emission of the scattered photon.

intensity is dependent on the fourth power of $\omega_S$. By measuring the dependence of the scattered intensity on the incident and scattered polarizations, one can deduce the symmetry of the Raman tensor and, hence, the symmetry of the corresponding Raman-active phonon. Thus, Raman scattering gives information about the frequency and symmetry of the zone-center phonon modes.

The Raman tensor is taken as a symmetric tensor since $\chi$ is a symmetric tensor.[†] The symmetry requirement involves that for certain choices of scattering geometries and polarizations, $\hat{e}_L$ and $\hat{e}_S$, the scattering radiation vanishes. These so-called Raman selection rules are the topic of the next section.

Before going into detail of the selection rules, it is worth to consider the Raman process quantum mechanically [Fig. 3.1(a)]. The scattering process happens in three steps. Firstly, an incident photon excites the

---

[†] This is only correct if one can neglect the slight difference in frequency between incident and scattered radiation. Within this approximation, antisymmetric components in the Raman tensor can be introduced only by magnetic fields [108]. Since most semiconductors are nonmagnetic, one can assume that the Raman tensor is symmetric.

material from the initial state $|i\rangle$ into an intermediate state $|n\rangle$ by creation of an electron-hole pair (1). Secondly, the electron-hole pair is scattered to another state $|n'\rangle$ by generation of a phonon. Finally, the electron-hole pair in the state $|n'\rangle$ recombine radiatively state under emission of the Stokes scattered photon (4). If in the process an electron-hole $(e-h)$ pair gets scattered to the state $|n''\rangle$ by annihilation of a phonon (3), a photon with higher energy is emitted and an anti-Stokes process appears. In the case that no electron-lattice interaction takes place (2) – i.e. no phonon scattering –, a Rayleigh process is observed and the energies of incident and emitted photons are equal. In the following, only Stokes processes are taken into account.[‡]

Since the interactions in the Raman scattering process are weak, the scattering probability can be calculated with third-order perturbation theory [111]. Here, only the mentioned Raman Stokes process is included.[§] The probability $P_{\mathrm{ph}}(\omega_{\mathrm{S}})$ for scattering a system from the initial state to the final state can be derived, as usual, via the Fermi Golden Rule and is given by [108]

$$P_{\mathrm{ph}}(\omega_{\mathrm{S}}) =$$

$$\left(\frac{2\pi}{\hbar}\right)\left|\sum_{n,\,n'} \frac{\langle i \mid H_{\mathrm{eR}}(\omega_{\mathrm{S}}) \mid n'\rangle\ \langle n' \mid H_{\mathrm{eL}}(\omega_{\mathrm{p}}) \mid n\rangle\ \langle n \mid H_{\mathrm{eR}}(\omega_{\mathrm{L}}) \mid i\rangle}{\left[\hbar\omega_{\mathrm{L}} - (E_n - E_i)\right]\left[\hbar\omega_{\mathrm{L}} - \hbar\omega_{\mathrm{p}} - (E_{n'} - E_i)\right]}\right|^2$$

$$\times\ \delta\left[\hbar\omega_{\mathrm{L}} - \hbar\omega_{\mathrm{p}} - \hbar\omega_{\mathrm{S}}\right]. \tag{3.8}$$

where $H_{\mathrm{eR}}$ and $H_{\mathrm{eL}}$ denote the interaction Hamiltonian between electron and photon (radiation) and between electron and phonon (lattice) according to the three steps of Stokes scattering. Other information about the medium, such as the electronic transitions, can be deduced from Eq. 3.8. This is in general very difficult due to the summation over all intermediate

---

[‡] Stokes processes are most commonly detected since the ratio of scattering intensities between Stokes ($I_{\mathrm{S}}$) and anti-Stokes ($I_{\mathrm{AS}}$) is given by [110] $I_{\mathrm{S}}/I_{\mathrm{AS}} = [(\omega_{\mathrm{L}} + \omega_{\mathrm{p}})/(\omega_{\mathrm{L}} - \omega_{\mathrm{p}})]^4\, e^{-\hbar\omega_{\mathrm{p}}/(k_{\mathrm{B}}T)}$. For room temperature measurements the anti-Stokes intensity is usually much weaker than the Stokes intensity.

[§] Further Raman processes, usually illustrated by Feynman diagrams, leading to the same final state, are not taken into account and can be found elsewhere [108, 112].

states in Eq. 3.8. But, one way to achieve this is by tuning the incident laser to resonate with a strong electronic interband transition. This is known as *resonant Raman scattering.* If $|a\rangle$ is a real discrete intermediate state with finite lifetime $\tau_a$ and $E_a$ is the transition energy, the Raman scattering probability for a given phonon mode in the vicinity of $E_a$ can be written as [108]

$$P_{\mathrm{ph}}(\omega_{\mathrm{S}}) \approx \left(\frac{2\pi}{\hbar}\right) \left| \frac{\langle i \mid H_{\mathrm{eR}} \mid a\rangle \quad \langle a \mid H_{\mathrm{eL}} \mid a\rangle \quad \langle a \mid H_{\mathrm{eR}} \mid i\rangle}{(E_a - \hbar\omega_{\mathrm{L}} - i\Gamma_a)\,(E_a - \hbar\omega_{\mathrm{S}} - i\Gamma_a)} \right|^2, \tag{3.9}$$

where $\Gamma_a$ is the damping constant related to $\tau_a$ by $\Gamma_a = \hbar/\tau_a$. Thus, a resonance enhancement can be observed when the incident ($\hbar\omega_{\mathrm{L}}$) or scattered light energy ($\hbar\omega_{\mathrm{S}}$) is close to $E_a$. In the case of a double resonance [113] where the incident and scattered light are in resonance with different transitions, both denominators are small simultaneously leading to a strong enhancement of the Raman intensity. The case of $\hbar\omega_{\mathrm{L}} = E_a$ is referred to as *incoming resonance* while $\hbar\omega_{\mathrm{S}} = E_a$ is an *outgoing resonance.*

In this work, the investigated transition is denoted as $E_1^{\mathrm{G}}$ in order to avoid confusion with the $\mathrm{E}_1$ optical phonon. $E_1^{\mathrm{G}}$ describes the transition at a *critical point*, also referred to as *van Hove singularity*, near the L point in the zincblende structure [114]. A critical point exists when the condition

$$|\nabla_{\boldsymbol{k}}(E_{\mathrm{c}} - E_{\mathrm{v}})| = 0 \tag{3.10}$$

is fulfilled [115], where $E_{\mathrm{c}}$ and $E_{\mathrm{v}}$ denote the energy of the conduction and valence band, respectively, and $\boldsymbol{k}$ the wave vector. These points can be easily identified in electronic band diagrams and occur where the conduction and valence bands are parallel, for example at the $\Gamma$ point – the valence band has a maximum and the conduction band a minimum – or close to the L point of the zincblende structure of InAs, as can be seen in Fig. 4.1(b). At these points the excitonic transitions are enhanced [108]. The $E_1^{\mathrm{G}}$ critical point is also referred to as saddle point since the plots of their energies versus wave vector resemble a saddle. This $E_1^{\mathrm{G}}$ transition energy is determined in Ch. 4 for the InAs zincblende and wurtzite structure by means of resonant Raman scattering.

### 3.1.2. Raman selection rules

The scattering intensity is dependent on the scattering geometry and the polarizations of the incident and scattered light. Using Eq. 3.7, one can calculate the polarization dependence of the scattered intensity, also referred to as the Raman selection rules. Since the Raman tensor in Eq. 3.7 includes the information about the crystal symmetry, one obtains different selection rules for distinct crystal structures. Thus, the polarization dependence provides a proper tool to distinguish different crystal structures from each other. In particular, for III-V nanowires, where the growth direction is mostly known, one can deduce the crystal phase from the polarization dependence of the Raman scattering. In order to distinguish the wurtzite and zincblende structure by polarized Raman scattering, first, the polarization dependence of the theoretical scattered intensities of zincblende bulk material is considered; then the theoretical results of zincblende and wurtzite nanowires are presented. Note that due to the symmetry nanowires possess an additional degree of freedom, i.e. although the growth direction of nanowires is known, the orientation of the other two coordinate axis is generally unidentified.

#### Zincblende bulk structure

The Raman selection rules can be derived from Eq. 3.7. For zincblende crystal optical phonons polarized along the directions $\hat{e}_1 = (100) \parallel x$, $\hat{e}_2 = (010) \parallel y$ or $\hat{e}_3 = (001) \parallel z$, their Raman tensors $\mathcal{R}_{e_1}$, $\mathcal{R}_{e_2}$ and $\mathcal{R}_{e_3}$ can be represented by a $(3 \times 3)$ matrix with nonzero elements $d$

$$\mathcal{R}_{e_1} = \begin{pmatrix} 0 & 0 & 0 \\ 0 & 0 & d \\ 0 & d & 0 \end{pmatrix}, \quad \mathcal{R}_{e_2} = \begin{pmatrix} 0 & 0 & d \\ 0 & 0 & 0 \\ d & 0 & 0 \end{pmatrix} \quad \text{and} \quad \mathcal{R}_{e_3} = \begin{pmatrix} 0 & d & 0 \\ d & 0 & 0 \\ 0 & 0 & 0 \end{pmatrix}. \tag{3.11}$$

The zone-center optical phonon is split into a longitudinal optical (LO) and two transverse optical (TO) modes. Note that, due to the macroscopic longitudinal electric field, the Raman tensor elements $d$ are different for the TO and the LO mode.

If one considers, for example, the (100) and the (111) surface, then the LO mode can be observed in backscattering configuration on both surfaces, whereas the TO mode is forbidden in backscattering from the

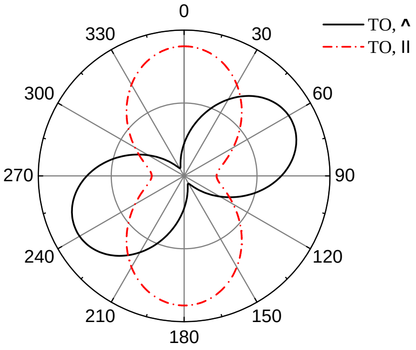

***Figure 3.2:*** Calculated intensity polar patterns of TO phonon mode in backscattering from a bulk substrate (110). The scattered light intensities polarized perpendicular ($I_\perp$) and parallel ($I_\parallel$) to the [111] direction is displayed as a function of the angle $\phi$ of the incident polarization with respect to the [111] direction. The LO phonon mode is forbidden in this configuration.

(100) surface. In order to obtain the selection rules for a crystal coordinate system $\{\hat{x}'_1, \hat{x}'_2, \hat{x}'_3\}$ different from the laboratory one, the Raman tensors have to be transformed in two steps. Firstly, the Raman tensors are transformed into the laboratory coordinate system with basis $\{\hat{e}_1, \hat{e}_2, \hat{e}_3\}$. Secondly, they are rotated around the $z$ axis by the angle $\theta$ (see Fig. 3.7), in order to account for the additional degree of freedom of the nanowires top surface. If a crystal coordinate system $\{\hat{x}'_1, \hat{x}'_2, \hat{x}'_3\}$ with

$$\hat{x}'_1 = \tfrac{1}{\sqrt{6}}[1,1,\bar{2}], \quad \hat{x}'_2 = \tfrac{1}{\sqrt{2}}[\bar{1},1,0] \quad \text{and} \quad \hat{x}'_3 = \tfrac{1}{\sqrt{3}}[1,1,1],$$

is assumed, the two transformations can be described by the matrices

$$T = \begin{pmatrix} \frac{1}{\sqrt{6}} & \frac{1}{\sqrt{6}} & -\frac{2}{\sqrt{6}} \\ -\frac{1}{\sqrt{2}} & \frac{1}{\sqrt{2}} & 0 \\ \frac{1}{\sqrt{3}} & \frac{1}{\sqrt{3}} & \frac{1}{\sqrt{3}} \end{pmatrix} \quad \text{and} \quad S = \begin{pmatrix} \cos\theta & -\sin\theta & 0 \\ \sin\theta & \cos\theta & 0 \\ 0 & 0 & 1 \end{pmatrix} \quad \text{and}$$

$$\hat{x}'_1 = T^{-1}\hat{e}_1, \quad \hat{x}'_2 = T^{-1}\hat{e}_2 \quad \text{and} \quad \hat{x}'_3 = T^{-1}\hat{e}_3, \tag{3.12}$$

where $T$ denotes the transformation into the basis $\{\hat{e}_1, \hat{e}_2, \hat{e}_3\}$ and $S$ the rotation about the nanowire axis $z$. For reasons of simplicity we define $M = S \cdot T$. The Raman tensors $R_{x'_i}$ for displacements along the directions $x'_i$ in the basis $\{\hat{e}_1, \hat{e}_2, \hat{e}_3\}$ can now be written as

$$\mathcal{R}_{x'_i} = \sum_{j=1}^{3} M_{ij} \mathcal{R}_{e_j}, \quad i = 1,2,3, \tag{3.13}$$

and the Raman tensors $\tilde{\mathcal{R}}_{x'_i}$ in the basis $\{\hat{x}'_1, \hat{x}'_2, \hat{x}'_3\}$ can be described by

$$\tilde{\mathcal{R}}_{x'_i} = M \cdot \mathcal{R}_{x'_i} \cdot M^T, \quad i = 1, 2, 3. \tag{3.14}$$

Here, it is considered a backscattering configuration along the $x$ axis. The polarization $\hat{e}_\mathrm{i}$ of the incident radiation and the polarization $\hat{e}_\mathrm{s}$ of the scattered light take the form (see Fig. 3.7)

$$\hat{e}_\mathrm{i} = \begin{pmatrix} 0 \\ \sin\phi \\ \cos\phi \end{pmatrix}, \hat{e}_\mathrm{s}^{\perp} = \begin{pmatrix} 0 \\ 1 \\ 0 \end{pmatrix}, \hat{e}_\mathrm{s}^{\parallel} = \begin{pmatrix} 0 \\ 0 \\ 1 \end{pmatrix}, \tag{3.15}$$

depending on whether the scattered radiation is analyzed perpendicular ($\hat{e}_\mathrm{s}^{\perp}$) or parallel ($\hat{e}_\mathrm{s}^{\parallel}$) to the wire axis. By inserting the obtained Raman tensors (Eq. 3.14) in Eq. 3.7, the Raman intensities of the zincblende structure for different configurations can be obtained. In Fig. 3.2, the theoretical intensities of the scattered light polarized perpendicular ($I_\perp$) or parallel ($I_\parallel$) to the [111] direction as a function of the angle $\phi$ of the incident polarization with respect to [111] are shown for TO phonons from a bulk substrate (110) in a polar plot taking into account only the contribution of the Raman tensors. For perpendicular analysis ($I_\perp$) the maximum intensity of the TO mode is obtained for an angle of the incident polarization of 63°, while for the parallel analyzed polarization ($I_\parallel$) the maximum intensity is found for 0° with respect to the [111] direction. The LO phonon mode is forbidden in this backscattering configuration.

### Zincblende nanowires

In order to calculate the polar patterns of $I_\mathrm{s}$ for nanowires, one has to take care of the additional degree of freedom associated with the rotation of $\theta$ around the nanowire axis, since it can influence the polar patterns of the optical modes. In the following, the polar patterns of zincblende and wurtzite nanowires grown along the [111] and [0001] direction, respectively, are addressed.

For zincblende nanowires grown in [111] direction, the Raman intensities of the TO and LO modes as a function of the rotation angle $\theta$ and the polarization angle $\phi$ has been calculated for scattered light polarized

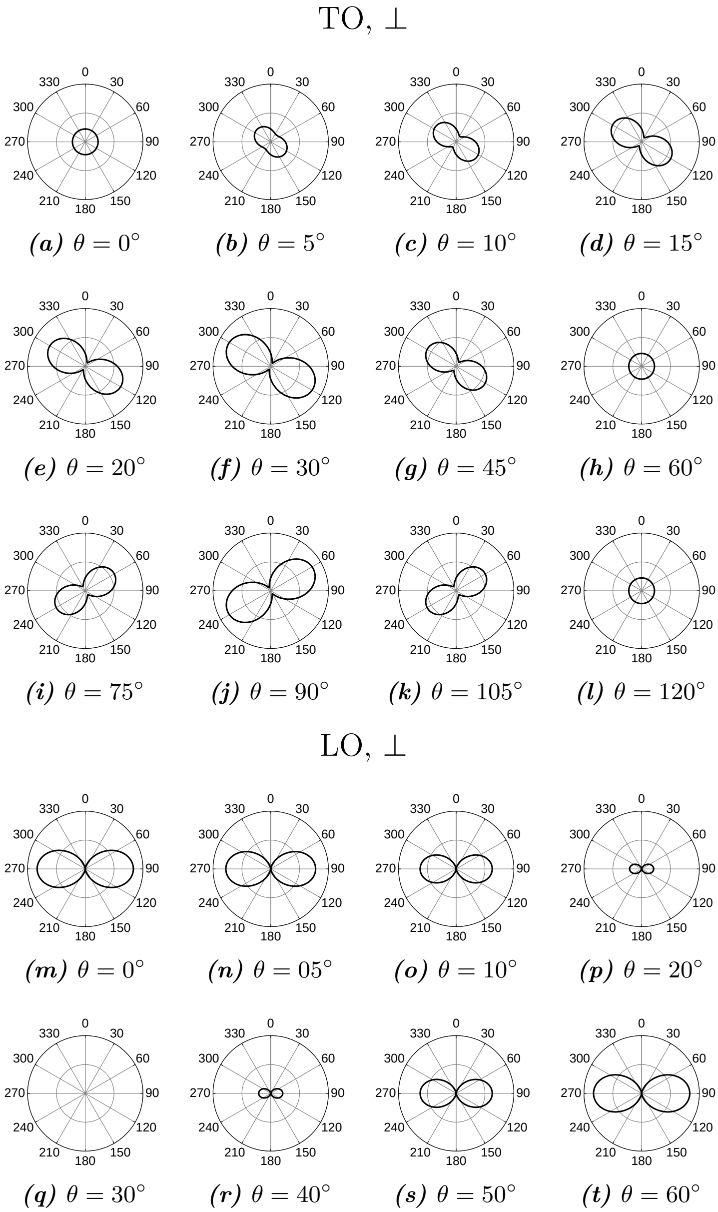

***(a)*** $\theta = 0°$ ***(b)*** $\theta = 5°$ ***(c)*** $\theta = 10°$ ***(d)*** $\theta = 15°$

***(e)*** $\theta = 20°$ ***(f)*** $\theta = 30°$ ***(g)*** $\theta = 45°$ ***(h)*** $\theta = 60°$

***(i)*** $\theta = 75°$ ***(j)*** $\theta = 90°$ ***(k)*** $\theta = 105°$ ***(l)*** $\theta = 120°$

***(m)*** $\theta = 0°$ ***(n)*** $\theta = 05°$ ***(o)*** $\theta = 10°$ ***(p)*** $\theta = 20°$

***(q)*** $\theta = 30°$ ***(r)*** $\theta = 40°$ ***(s)*** $\theta = 50°$ ***(t)*** $\theta = 60°$

***Figure 3.3.:*** Calculated polar patterns of the TO and LO intensities under perpendicular analysis ($\perp$) for different rotation angles $\theta$ for a zincblende nanowire oriented along $\phi = 0°$. The TO patterns present a periodicity of $120°$ and are independent of $\phi$ for $\theta = 0°, 60°, 120°$ while the LO patterns have a periodicity of $60°$ and the Raman signal vanishes for $\theta = 30°$. For $\theta = 0°$ and $\theta = 90°$, the $x_1'$ axis represents the $[11\bar{2}]$ and $[\bar{1}10]$ directions, respectively.

parallel ($\|$) and perpendicular ($\perp$) to the wire axis and are given as

$$I_{\|}^{\mathrm{TO}}(\theta,\phi) = \frac{1}{6} d_{\mathrm{TO}}^2 \left[5 + 3\cos(2\phi)\right], \tag{3.16}$$

$$\begin{aligned} I_{\perp}^{\mathrm{TO}}(\theta,\phi) = {} & \frac{1}{6} d_{\mathrm{TO}}^2 \{3 - \cos(6\theta) - 2\sin(3\theta) \\ & \times \left[\cos(2\phi)\sin(3\theta) + \sqrt{2}\sin(2\phi)\right]\Big\}, \end{aligned} \tag{3.17}$$

$$I_{\|}^{\mathrm{LO}}(\theta,\phi) = 0, \tag{3.18}$$

$$I_{\perp}^{\mathrm{LO}}(\theta,\phi) = \frac{2}{3} d_{\mathrm{LO}}^2 \cos^2(3\theta)\sin^2(\phi). \tag{3.19}$$

The corresponding polar pattern of the TO modes for a parallel analyzer ($\|$) is identical to the one shown in Fig. 3.2 for all rotation angles (independent of $\theta$) while the TO and LO modes for a perpendicular analyzer ($\perp$) do vary with $\theta$. This is illustrated in Fig. 3.3 where the calculated polar patterns are displayed for different rotation angles $\theta$. In this configuration, the directions $[11\bar{2}]$ and $[\bar{1}10]$ correspond to $\theta = 0°$ and $\theta = 90°$, respectively. Note that the polar pattern for the TO mode presents a periodicity of 120° and that, although the polar pattern is circular (*i.e.* independent of the incident polarization) for $\theta = N \times 60° (N = 0, 1, 2\dots)$, for any other angle the scattering is polarized. The maximum scattering intensity is dependent on both the rotation angle $\theta$ and the polarization angle $\phi$. Note that the highest intensities are obtained for polarization angles $\phi_{\max}^{\mathrm{TO}}$ different from 0° and 90° [for example, $\phi_{\max}^{\mathrm{TO}} \in (45°, 63°)$ for $\theta \in (60°, 120°)$]. For the LO mode, the polar patterns have a periodicity of 60° and the LO intensity vanishes for $\theta = 30° + N \times 60° (N = 0, 1, 2\dots)$. For all other rotational angles, the Raman scattering is polarized and the maximum scattering intensities are always obtained for the polarization angles $\phi_{\max}^{\mathrm{LO}} = 90°, 270°$, i.e. the highest intensities can be detected when the incident light polarization is polarized perpendicular to the nanowire. In the case of a parallel analyzer ($\|$), the LO mode is forbidden for all rotation ($\theta$) and polarization ($\phi$) angles. These angular dependences are characteristic for zincblende nanowires and allow to identify the rotation angle of the nanowires.

### Wurtzite nanowires

As described in Sec. 2.3 where the wurtzite and zincblende structure have been introduced, the unit cell of the zincblende phase is approximately twice as large as the one for the wurtzite one [116, 117]. As a consequences, the phonon dispersion of the wurtzite structure can be approximated by simply folding the Brillouin zone of the zincblende phase along the [111] direction. This leads to new allowed Raman modes which belong to the $A_1$, $E_1$ and $E_2$ representations illustrated in Fig. 3.4. The corresponding Raman tensors can be represented by the following $(3 \times 3)$ matrices with nonzero elements $a$, $c$, $e$ and $f$

$$\begin{gathered} A_1(z) = \begin{pmatrix} a & 0 & 0 \\ 0 & a & 0 \\ 0 & 0 & c \end{pmatrix}, \; E_1(x) = \begin{pmatrix} 0 & 0 & e \\ 0 & 0 & 0 \\ e & 0 & 0 \end{pmatrix}, \; E_1(y) = \begin{pmatrix} 0 & 0 & 0 \\ 0 & 0 & e \\ 0 & e & 0 \end{pmatrix}, \\ E_2 = \begin{pmatrix} 0 & f & 0 \\ f & 0 & 0 \\ 0 & 0 & 0 \end{pmatrix} \quad \text{and} \quad E_2 = \begin{pmatrix} f & 0 & 0 \\ 0 & -f & 0 \\ 0 & 0 & 0 \end{pmatrix}. \end{gathered} \tag{3.20}$$

Note that the corresponding coordinate system of theses matrices is the same as the laboratory system used before ($z \parallel [0001]$). Due to its symmetry, the $I_\mathrm{s}$ for wurtzite nanowires grown in [0001] direction does not present any dependence on $\theta$. In Fig. 3.5, the calculated polar patterns of the $A_1$, $E_1$ and $E_2$ modes are shown. For the polar $A_1$(TO) mode, the strongest values of $I_\mathrm{s}$ are obtained in the parallel configurations $\{x(y,y)\bar{x}$, $x(z,z)\bar{x}$, using Porto's notation[¶] [118]$\}$, i.e. when the incident and scattered light polarizations are parallel to each other. On the contrary, the polar $E_1$(TO) mode is strongest in perpendicular configurations, where the incident and scattered light polarizations are perpendicular to each other [$x(y,z)\bar{x}$, $x(z,y)\bar{x}$]. The $E_2$ mode is forbidden for any configuration but $x(y,y)\bar{x}$. Here, the incident and the scattered light polarizations are perpendicular to the wire axis. Furthermore, no LO phonon is allowed.

In Table 3.1 the allowed phonon modes of the zincblende and wurtzite structure for different backscattering scattering configurations are shown.

---

[¶] The letter sequence $i(j,k)l$ represent the direction of the wave vector (propagation) of the incoming light ($i$), its polarization ($j$) and the polarization ($k$) and the propagation direction ($l$) of the analyzed (scattered) radiation, respectively.

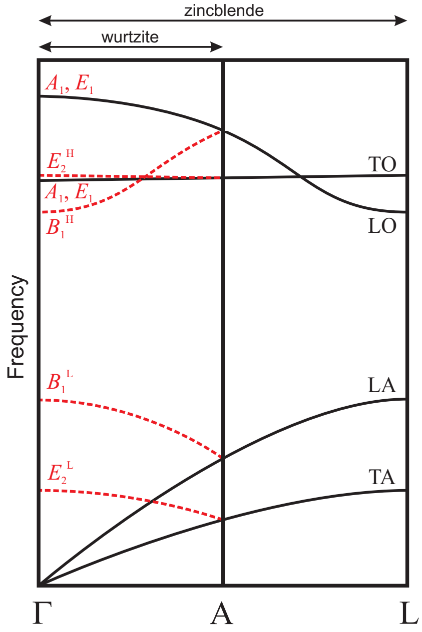

***Figure 3.4:*** Schematic representation of the phonon dispersion in the zincblende and wurtzite structure. Phonon branches along [111] in the zinc blende structure are folded to approximate those of the wurtzite structure along [0001]. Γ, L and A denote the symmetry points at the zone center and at the Brillouin zone boundary along the [111] direction in zincblende and the [0001] direction in wurtzite structure, respectively.

| Surface | $\hat{e}_\mathrm{i}$ | $\hat{e}_\mathrm{s}$ | Porto notation | Allowed modes | |
|---|---|---|---|---|---|
| | | | | Cubic | Hexagonal |
| (001) | [100] | [010] | $z(x,y)\bar{z}$ | LO | $E_2$ |
| | [100] | [010] | $z(x,y)\bar{z}$ | - | $A_1$(LO), $E_2$ |
| $(1\bar{1}0)$ | $[11\bar{2}]$ | $[11\bar{2}]$ | $x'(y,y)\bar{x}'$ | TO | $A_1$(TO), $E_2$ |
| | $[11\bar{2}]$ | [111] | $x'(y',z')\bar{x}'$ | TO | $E_1$(TO) |
| | [111] | $[11\bar{2}]$ | $x'(z',y')\bar{x}'$ | TO | $E_1$(TO) |
| | [111] | [111] | $x'(z',z')\bar{x}'$ | TO | $A_1$(TO) |

***Table 3.1.:*** Raman selection rules for backscattering configuration. The cubic and hexagonal modes, representative for the zinc blende and wurtzite structure, respectively, for different polarization configurations are given. ($x$ = [100], $y$ = [010], $z$ = [001], $x'$ = $[1\bar{1}0]$, $y'$ = $[11\bar{2}]$ and $z'$ = [111].

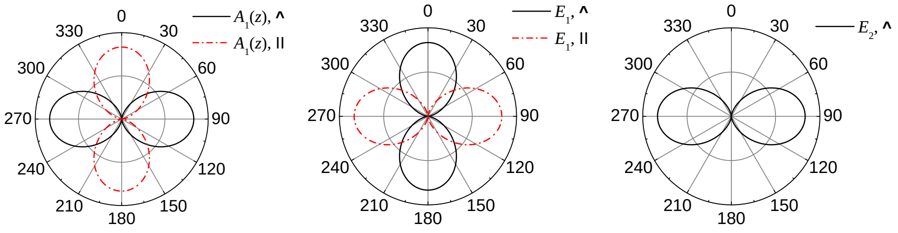

***(a)*** A₁(TO) mode ***(b)*** E₁(TO) mode ***(c)*** E₂ mode

***Figure 3.5.:*** Calculated intensity polar patterns of the wurtzite modes for a nanowire oriented along $\phi = 0°$. The $E_2$ intensity is zero for parallel analysis (∥). While the maximum intensity for the $A_1$ mode is obtained in parallel configurations, the highest intensity of the $E_1$ mode is achieved for crossed polarizations.

Besides the symmetry considerations discussed so far, J. R. Madureira[‖], collaborator of this work, calculated the phonon dispersion for the InAs wurtzite structure using an extended 11-parameter rigid-ion-model. This method allows to calculate the phonons in a wurtzite structure parameterizing a known phonon dispersion relation of a zincblende structure. Thus, from the fit of the experimental phonon dispersion data of zincblende InAs from Ref. [119], it was calculated the phonon dispersion as well as the two-phonon density of states of the wurtzite structure. The obtained optical phonon modes at the Γ point of the wurtzite structure are presented in Tab. 3.2. Note that the calculated values of the phonon energies are supposed to be higher than the experimental Raman phonon energies since the fitting of the zincblende data [119] obtained by X-ray thermal diffuse scattering exhibit $\sim 7 - 9\,\text{cm}^{-1}$ higher phonon energies than the zincblende InAs Raman data [120].

***Table 3.2.:*** Optical phonon modes and their frequencies in wurtzite InAs calculated by an extended 11-parameter rigid-ion-model (J. R. Madureira).

| WZ mode | $E_1$(LO) | $A_1$(LO) | $E_1$(TO) | $A_1$(TO) | $E_2^{H}$ | $E_2^{L}$ |
|---|---|---|---|---|---|---|
| $\nu$ (cm$^{-1}$) | 246.8 | 246.3 | 226.0 | 225.5 | 219.2 | 43.6 |

---

[‖] Owing to a collaboration with the *Faculdade de Ciências Integradas do Pontal da Universidade Federal de Uberlândia* in Ituiutaba-MG, Brazil.

These results show that the calculated $E_2^{\mathrm{H}}$ mode is similar in frequency to the $\mathrm{A}_1$(TO) and $\mathrm{E}_1$(TO) modes. The slight splitting between the $E_2^{\mathrm{H}}$ and the $\mathrm{A}_1$(TO) mode is only 6.3 cm$^{-1}$. This is expected due to the fact that the TO phonon dispersion along the [111] direction of the zincblende structure is nearly horizontal [119].

## 3.1.3. Experimental Raman setup

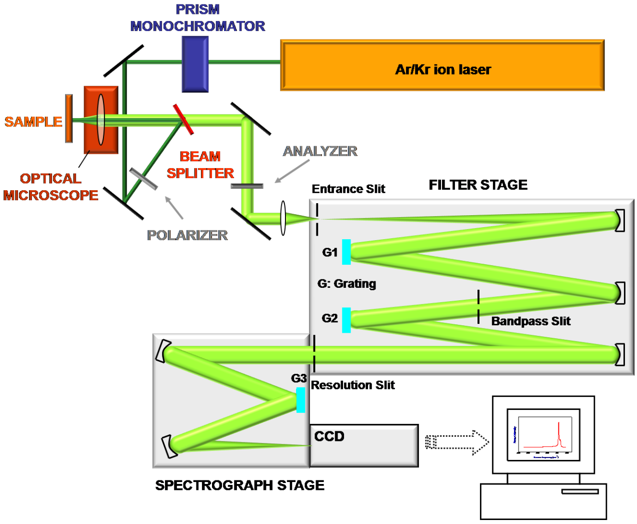

***Figure 3.6.:*** Schematic experimental Raman setup used in this work.

In this section the essential parts of the used Raman setup are presented. The basic problems of Raman detection are the low intensity of the Raman scattering and the much larger intensity of the Rayleigh scattering which is normally very close in energy to the Raman scattered light. The first problem can be resolved by using lasers which can provide monochromatic light of high intensities, whereas in the second case double or triple monochromators can be used to separate the strong Rayleigh scattered light from the relatively weak Raman scattered one. All measurements have been performed in backscattering geometry. To get a better understanding of the setup, the optical path and the different elements are illustrated in Fig. 3.6.

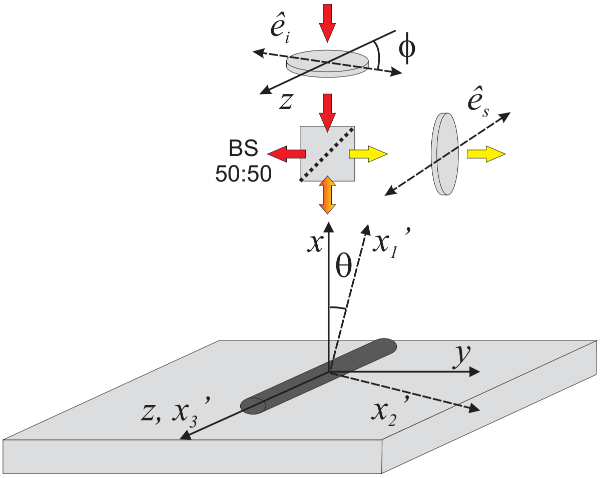

***Figure 3.7:*** Schematic diagram of the used coordinate systems ($x$,$y$,$z$) and ($x_1'$,$x_2'$,$x_3'$) in backscattering geometry. $\hat{e}_\mathrm{i}$ and $\hat{e}_\mathrm{s}$ are the incident and scattered light polarizations, respectively.

The lines of an Ar/Kr ion laser were used for excitation at a relatively low laser power (∼ 600 µW) in order to avoid sample heating. The scattered light was dispersed by a Jobin Yvon T64000 spectrometer and detected with a liquid-nitrogen-cooled charge coupled device (CCD). In order to perform polarization dependent measurements, the incident light passes through a $\lambda/2$ plate so that its polarization $\hat{e}_\mathrm{i}$ can be rotated by an angle $\phi$ with respect to the growth axis of the nanowire. Before being focused on the nanowire by a 50× objective, the light passes a beam splitter. In addition, an analyzer — set either parallel or perpendicular to the nanowire axis — was used to filter the polarization of the scattered light $\hat{e}_\mathrm{s}$. With this setup equivalent experiments with a fixed incident polarization and a rotatable analyzer can be carried out. A schematic diagram of the setup is shown in Fig. 3.7. Two coordinate systems are introduced: the laboratory coordinates system ($x$,$y$,$z$) and the crystal coordinates system of the nanowire ($x_1'$,$x_2'$,$x_3'$). $z$ and $x_3'$ are parallel to the growth axis of the nanowire while $x_1'$ is rotated by an angle $\theta$ with respect to the $x$ axis in the $x$-$y$ plane.

## 3.2. Photoluminescence Spectroscopy

In the previous section, it has been described that the light scattering by phonons in a semiconductor can be used to obtain information about the structural, optical and electronic properties of a material. In this section it will be focused on the optical emission of a semiconductor. When an $e-h$ pair in a semiconductor gets excited with energy higher than the band gap, this pair can recombine radiatively emitting a photon with energy lower than the one of excitation (luminescence). If the initial excitation of electrons is achieved by an external current, by electron bombardment, via heating or by photoexcitation of the sample, the method is known as *electroluminescence*, *cathodoluminescence*, *thermoluminescence* or *photoluminescence* (PL), respectively. The latter has been investigated for different nanowire samples in this work.

As mentioned before, PL represents the radiative recombinations of photoexcited $e-h$ pairs. If these $e-h$ pairs are located in different energy states, their radiative recombination leads to the emission of photons with distinct energies which correspond to different transitions in the semiconductor. These transitions provide information about the electronic bands or states in semiconductors. Therefore, PL spectroscopy is a powerful and contactless nondestructive method of probing the electronic band structure.

First of all, the PL and the most common radiative recombination processes are highlighted. Then, the polarization dependence of the absorption and emission of light from nanowires is presented. It will be seen that the crystal structure varies the absorption and emission characteristics of nanowires. These characteristics have been used to distinguish the crystal structure of nanowires. Finally, the experimental setups used in this work are described.

### 3.2.1. Photoluminescence

The process of PL requires a non-equilibrium carrier concentration in the electronic bands or in the electronic states of a defect structure which is obtained by photoexciting $e-h$ pairs in a semiconductor. In most cases the carriers thermalize (energy loss due to interaction with phonons) and reach the lowest excited state (conduction/valence band or defect/impurity states in the band gap) where they recombine radiatively. Thus, the luminescence process involves three separate steps: excitation, thermalization and recombination.

In Fig. 3.8, some often observed radiative recombination processes are schematically depicted which are briefly described in the following. For a more comprehensive discussion, see Refs. [108, 110].

**Band-to-band transitions** In a perfect semiconductor, the excited $e - h$ pairs will thermalize to the band edges of the conduction and valence band where they tend to recombine. For this recombination process, the conservation of energy and momentum holds and, therefore, the emitted photon energy is the energy difference between electron and hole states. This process is illustrated in Fig. 3.8(a). Electrons and holes that have thermalized to the conduction band minimum (CBM) and valence band maximum (VBM) at $\mathbf{k} = \mathbf{0}$, respectively, can recombine radiatively [transition (i)]. This is referred to as a *direct transition.* Since photons have a negligible small momentum comparable to phonons, these transitions occur vertical in the band structure schematic. In contrast, an *indirect transition* [transition (ii)] takes place when the transition happens under participation of a phonon. These recombinations occur vertical *and* horizontal in the band structure schematic. In this case, the recombination process requires the interaction with a phonon with wave vector $\mathbf{q}_{\mathrm{ph}}$, leading to an exchange of energy and momentum with the crystal lattice. If the CBM and VBM are both located at $\mathbf{k} = \mathbf{0}$, the semiconductor has a *direct band gap.* In a situation where the location of the extrema are not identical [as can be seen in Fig. 3.8(a)], the semiconductor is referred to as *indirect* or has an *indirect band gap.* For indirect semiconductors the electron states near $\mathbf{k} = \mathbf{0}$ are not occupied efficiently since the CBM is located at a different position. Electrons in the CBM cannot recombine with holes in the VBM without interaction of a phonon due to momentum conservation. Thus, radiative recombinations in indirect semiconductors, such as Si and Ge, are much less probable than in direct ones, like GaAs and InAs, and the radiative recombination times of $e - h$ pairs in semiconductors with indirect band gaps are much larger than those with direct gaps. For intrinsic semiconductors at room temperature, for example, the radiative carrier lifetime for Si and GaAs are 4.6 h and 2.8 µs, respectively [108]. These values exhibit a difference of more than five orders of magnitude. For this reason, mostly semiconductors with direct band gap are utilized in optoelectronic devices.

The recombination of electrons and holes, that are located in the conduc-

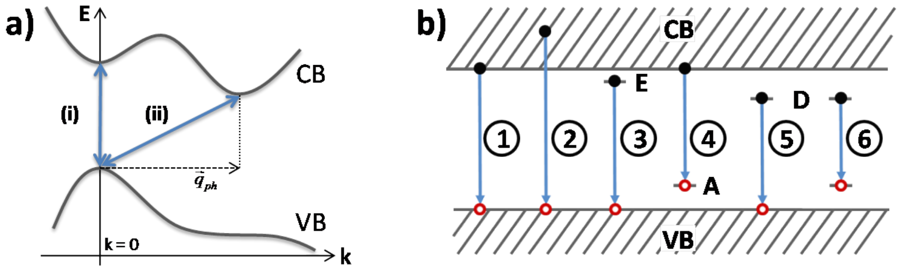

***Figure 3.8.:*** Schematic diagrams of (a) a direct (i) and an (ii) indirect transition between the conduction (CB) and valence band (VB) and (b) possible radiative transitions in semiconductors. The transitions ① and ② correspond to band-to-band transitions, ③ is an excitonic transitions, ④ and ⑤ are free-to-bound transitions and ⑥ represents the donor-acceptor pair transition (E: exciton, D: donor, A: acceptor). (b) has been adapted from Ref. [110].

tion and valence bands, respectively [transitions ① and ② of Fig. 3.8(b)], are referred to as *band-to-band transitions*.

**Excitonic transitions** In high purity semiconductors and low temperatures, photoexcited free electrons and free holes can be attracted to one another by the Coulomb interactions forming a hydrogenic-like *free exciton*. When this $e-h$ pair recombines, it emits a narrow spectral line with the energy $E_{\mathrm{FX}} = E_{\mathrm{g}} - E_{\mathrm{X}}$ where $E_{\mathrm{g}}$ is the band gap energy and $E_{\mathrm{X}}$ the exciton binding energy (transition ③). When the sample contains low donor or acceptor concentrations, as well as a low density of defects, the photoexcited carriers are not only attracted by each other, but also to the neutral donors and acceptors via the van der Waals interaction. Since the additional attraction reduces the exciton binding energy, the neutral impurities are efficient in trapping excitons to form *bound excitons* at low temperature, denoted as ($\mathrm{D}^0$,X) and ($\mathrm{A}^0$,X) for neutral donors and acceptors, respectively.

**Free-to-bound transitions** At sufficiently low temperature, carriers are frozen on impurities, i.e. holes and electrons can be trapped on the acceptor and donor sites, respectively. If a free carrier is generated, for example in a PL experiment, it can recombine radiatively with the carriers bound to impurities (e. g. an electron in the conduction band with a hole trapped on the acceptor) which is referred to as *free-to-bound transition* (transitions ④ and ⑤). Thus, at low temperatures the free-to-bound transition is expected to dominate the PL spectra. When the temperature rises, the frozen carriers get excited to the band edges and the band-to-band transition appear. At high enough temperatures, as more carriers are excited to the band edges, the spectra will be dominated by the band-to-band transition.

**Donor-acceptor pair transition** Quite often, a semiconductor contain both donors and acceptors. Under equilibrium conditions, the electrons from the donor will be captured by the acceptors which leads to ionized donors ($D^+$) and acceptors ($A^-$). If an exciton is generated by optical excitation, the electrons and holes can be trapped by the ($D^+$) and ($A^-$) sites. Some of the electrons on the neutral donors ($D^0$) can subsequently recombine radiatively with the holes on the neutral acceptors ($A^0$). This process is known as *donor-acceptor pair transition* (transition ⑥).

### Quantum confinement effects

For semiconductors where one dimension has a length comparable or smaller than their exciton Bohr radius, quantum confinement effects can occur. Dependent on whether the carriers are confined in one, two or three directions, the semiconductor is referred to as quantum well, quantum wire or quantum dot, respectively. One of the most notable aspects of these structures is the size dependence of the semiconductor band gap. If the size decreases, the band gap increases opening many possibilities for applications of tunable nanostructures in optoelectronic devices.

In this work, wurtzite/zincblende quantum well structures have been considered in III-V nanowires. As will be seen later, thin sections in an alternating wurtzite/zincblende sequence along a nanowire can exhibit quantum confined states.

### Time-resolved PL spectroscopy

Recording the time evolution of the occurring PL processes in a semiconductor can get insight into the carrier dynamics. Beside the optical pump-probe spectroscopy – where two laser pulses with variable time delay are used to photoexcite the sample (pump) and to interrogate the excited state population (probe) by recording its change in absorbance –, time-resolved PL (TRPL) spectroscopy is very suitable to investigate the recombination dynamics of photoexcited carriers which are essential for the characterization of the system. With a pulsed laser in TRPL measurements, it is possible to study processes that occur on very short time scales down to femtoseconds. For it, a laser with very small pulse width and a time-gated camera with high temporal resolution is needed. If a short laser pulse photoexcites an amount of carriers in a semiconductor, a fraction of the $e-h$ pairs recombine radiatively and the PL can be recorded temporally providing information about the carrier lifetime. This allows, for example, to study the dynamics of excitons, spins and their lifetimes in nanowires.

In this work, TRPL has been used to investigate the recombination dynamics of photoexcited electrons and holes in GaAs and InGaAs/GaAs nanowires that are acoustically transferred along the wire axis to a second location where they recombine.

## 3.2.2. Polarized photoluminescence characteristics of nanowires

The large ratio between length and diameter in nanowires leads to a polarization anisotropy of the absorption and emission of light in the quasistatic limit, i. e., when the diameter of the nanowire is much smaller than the wavelength of the incident and emitted light.

If a cylindrical wire is placed in an external electric field $\boldsymbol{E}^{\text{ext}}$, its parallel component, $E_{\|}^{\text{ext}}$, being continuous at the interface, remains the same inside the wire [22],

$$E_{\|} = E_{\|}^{\text{ext}}. \tag{3.21}$$

At the same time, the component normal to the wire axis, $E_{\perp}$, will be essentially suppressed inside the wire due to the boundary conditions at

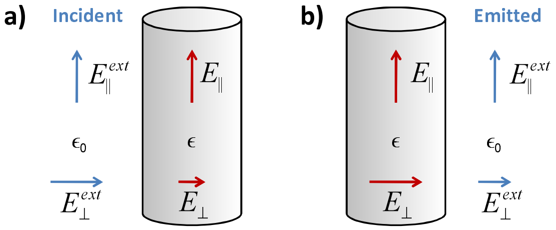

***Figure 3.9.:*** (a) The electric field inside the wire with isotropic excitation. (b) The electric field of the emission from the wire with an isotropic electric field inside the wire. The lengths of the arrows represent the strength of the electric fields.

the wire-surrounding interface [22] (see Fig. 3.9a)

$$E_{\perp} = \frac{2\epsilon_0}{\epsilon + \epsilon_0} E_{\perp}^{\text{ext}} \tag{3.22}$$

where $\epsilon_0$ and $\epsilon$ are the dielectric constants of the surrounding and the wire material, respectively. The fraction of the absorbed intensity by the wire will be proportional to the field inside the wire. Thus, the polarization anisotropy for absorption $\rho_{\text{abs}}$ can be expressed by

$$\rho_{\text{abs}} = \frac{\left|E_{\parallel}\right|^2 - |E_{\perp}|^2}{\left|E_{\parallel}\right|^2 + |E_{\perp}|^2}. \tag{3.23}$$

For a homogeneous incident field, the absorption anisotropy can be rewritten by using Eqs. 3.21 and 3.22 to

$$\rho_{\text{abs}} = \frac{\left|(\epsilon/\epsilon_0)^2 + 1\right|^2 - 4}{\left|(\epsilon/\epsilon_0)^2 + 1\right|^2 + 4} \tag{3.24}$$

Using the dielectric constant for bulk InAs ($\epsilon_{\text{InAs}} = 15.15$) and GaAs ($\epsilon_{\text{GaAs}} = 12.4$), the theoretical calculated polarization anisotropies are 0.97 and 0.95, respectively. In the case of the anisotropy of the emission, the effect is qualitatively similar to the property of absorption but the magnitude of the polarization ratio is different. If an isotropic distribution of photons polarized parallel and perpendicular to the wire axis is assumed (see Fig. 3.9b), the polarization anisotropy for the emission, $\rho_{\text{em}}$, is given by [22]

$$\rho_{\mathrm{em}} = \frac{I_{\parallel}^{\mathrm{ext}}}{I_{\perp}^{\mathrm{ext}}} = \frac{(\epsilon/\epsilon_0 + 1)^2 + 2}{6} \tag{3.25}$$

where $I_{\parallel}^{\mathrm{ext}}$ and $I_{\perp}^{\mathrm{ext}}$ are the intensities emitted with the polarization parallel and perpendicular to the long axis of the wire.

These considerations are valid for all wires independent of their crystal structure. However, if the electronic band structure is considered, differences in the absorption and emission exist between wires with zincblende and wurtzite phase. At the $\Gamma$ point of the zincblende structure, the s-like electrons in the conduction band have $\Gamma_6$ symmetry, the p-like light and heavy holes have $\Gamma_8$ symmetry and the split-off hole has $\Gamma_7$ symmetry, as illustrated in Fig. 3.10. According to selection rules [108], the recombination $\Gamma_{6\mathrm{C}} \rightarrow \Gamma_{8\mathrm{V}}$ of electrons from the conduction band with $\Gamma_6$ symmetry and holes from the valence band with $\Gamma_8$ symmetry are dipole-allowed and unpolarized. This means that the polarization anisotropy in zincblende wires is governed only by the dielectric contrast between wire and surrounding material.

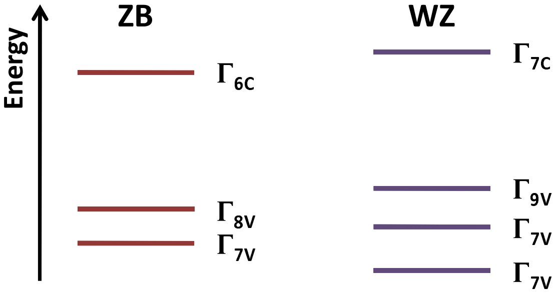

***Figure 3.10.:*** Symmetry of the valence and conduction bands at the $\Gamma$ point of the zincblende (ZB) and wurtzite (WZ) structure, respectively.

If the wire has wurtzite structure, the situation is different. The combination of the crystal field splitting and the spin orbit coupling splits the valence band into the $\Gamma_9$ heavy-hole, the $\Gamma_7$ light-hole and the $\Gamma_7$ split-off bands (see Fig. 3.10). Here, the selection rules are different and the lowest energy recombination $\Gamma_{7\mathrm{C}} \rightarrow \Gamma_{9\mathrm{V}}$ is only dipole-allowed if the electric field is perpendicular to the $c$-axis of the wire [116, 121], while the $\Gamma_{7\mathrm{C}} \rightarrow \Gamma_{7\mathrm{V}}$ transitions are dipole-allowed and unpolarized. In most cases, the wires are grown in [0001] direction so that the *c*-axis is parallel to the growth direction of the wire. That means that due to the dielectric contrast between the wire and surrounding material, absorption and emission of light polarized along the nanowire axis is favored, but the selection rules only allow the $\Gamma_{7\mathrm{C}} \rightarrow \Gamma_{9\mathrm{V}}$ emission and absorption of light polarized perpendicular to the wire axis. Thus, the emission and absorption parallel to the wire becomes suppressed for wurtzite nanowires.

### 3.2.3. Photoluminescence and acoustic transport

As seen in the last sections, photoexcited electrons and holes can recombine under emission of light. In order to transport photoexcited carriers, one has to prevent their recombination and has to move them away from the generation site. Both can be realized by Rayleigh SAWs which are described in more detail in Appendix A. The SAWs are localized near the surface and consist of the superposition of a longitudinal acoustic mode polarized parallel to the propagation direction of the SAW and a transversal mode polarized perpendicular to the surface. This leads to a displacement field and to alternating regions of tensile and compressive strain along the propagation direction. Due to the strain and its corresponding piezoelectric potential, a dynamic type-II modulation of the electronic band edges is imposed as schematically depicted in Fig. 3.11.

It has been shown that these “traveling potential wells” can be used to transport electrons at the velocity of sound in quantum well structures [67–69]. First, a laser pulse photoexcites $e-h$ pairs (①). These can be separated by the piezoelectric potential that, thereafter, stores the separated electrons and holes in the maxima and minima of the moving potential (②), as reported by Rocke *et al.* [122] for photoexcited carriers in a quantum well. The spatial separation reduces dramatically the recombination probability and increases the radiative lifetime by several orders of magnitude as compared to the unperturbed case. This allows to transport the trapped $e-h$ pairs over macroscopic distances of some millimeters (③) to a remote position where the electrons and holes can recombine [122]. The efficiency of the transport process, however, is affected by various parameters. The binding energy of $e-h$ pairs, for example, have to be overcome to dissociate electron and holes. Carriers may be bounded and exhibit different ionization energies. Several defect states can trap the

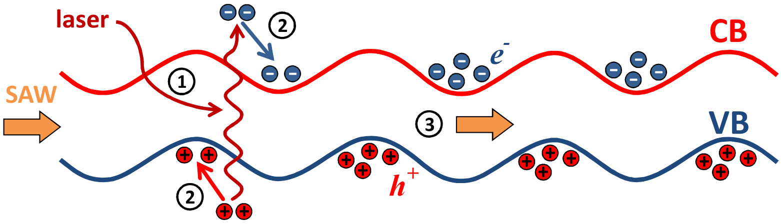

***Figure 3.11.:*** Induced type-II modulation of the band edges by a SAW. An incident laser pulse photoexcites $e-h$ pairs (①) which dissociate due to the modulated conduction (CB) and valence band (VB) structure. The electrons move to local CB minima and the holes to local VB maxima (②) which are separated spatially from each other. This prevents the recombination of the carriers and allows to transport the carriers in the SAW propagation direction (③). The dynamic type-II modulation of the band edges is referred to as well as “traveling potential wells”.

separated carriers and hamper their transport. Phonon interaction with carriers is dependent on temperature and becomes important for higher temperatures where the scattering rate gets high. In addition, the applied acoustic power is significant since the acoustic excitation modulates the band edges.

This mechanism has been used in this work to transport photogenerated electrons and holes in GaAs and (In,Ga)As/GaAs nanowires along the wire axis to a second position where their recombination leads to remote PL pulses (see Ch. 5). The acoustic transport mechanism has been proposed to be a building block for single photon sources [123, 124]. This method has been applied to (In,Ga)As/GaAs nanowires in Ch. 6 where a high-frequency source of antibunched photons has been realized.

### 3.2.4. Experimental photoluminescence setups

In the following, the different experimental setups used in this work for the PL measurements are presented. Since the band gap energy of InAs (~ 3 μm) is much lower than the one of GaAs (~ 818 nm), different setups were used.

**PL setup for InAs nanowires** The PL measurements were carried out using a pulsed Ti-sapphire laser as excitation source with a pulse width of ~ 3 ps and a repetition rate of ~ 80 MHz in order to avoid nanowire heating. The laser was syntonized at 760 nm and focused on a spot of approximately 1 mm$^2$. The luminescence was detected by a 0.5 m monochromator with 300 g/mm, blazed at 2 µm and a liquid-N$_2$ cooled InSb photodiode providing excellent performance in the 1 to 5.5 µm wavelength region. The sample was cooled with a cold-finger He cryostat with CaF$_2$ optical windows where the temperature was varied from 5 K to 100 K. In Fig. 3.12 a schematic diagram of the used setup is displayed and in Tab. 3.3 basic parameters for the PL measurements are presented.

| Laser | Monochromator | Detector | Sample temperature |
|---|---|---|---|
| Pulsed Ti-sapphire (760 nm) | 300 g/mm | InSb photodiode (1 – 5.5 µm range) | 5 K – 100 K |

***Table 3.3.:*** Basic parameters for the PL measurements on InAs nanowires.

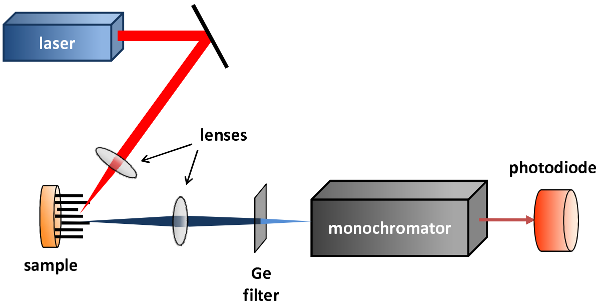

***Figure 3.12.:*** Schematic diagram of the setup for the PL measurements on InAs nanowire ensembles.

**PL setup for GaAs and (In,Ga)As/GaAs nanowires** The optical measurements were carried out on GaAs and (In,Ga)As/GaAs nanowires dispersed on the surface of a SAW delay line, that is described below, with the growth axis incidentally aligned with the SAW propagation direction, as illustrated in the magnification of the sample in Fig. 3.13.

The experiments were performed by mounting the sample in a microscope cryostat for spatially resolved PL measurements at a nominal temperature of 20 K (basic setup in Fig. 3.13). A 757 nm diode laser yielding 150 ps wide pulses was used as excitation source. The laser beam was focused onto the nanowires by using a 50× objective. The PL emitted over the length of the nanowire was collected by the same objective, imaged on the entrance slit of a spectrometer and detected with spatial resolution (∼ 1 µm) by a CCD camera.

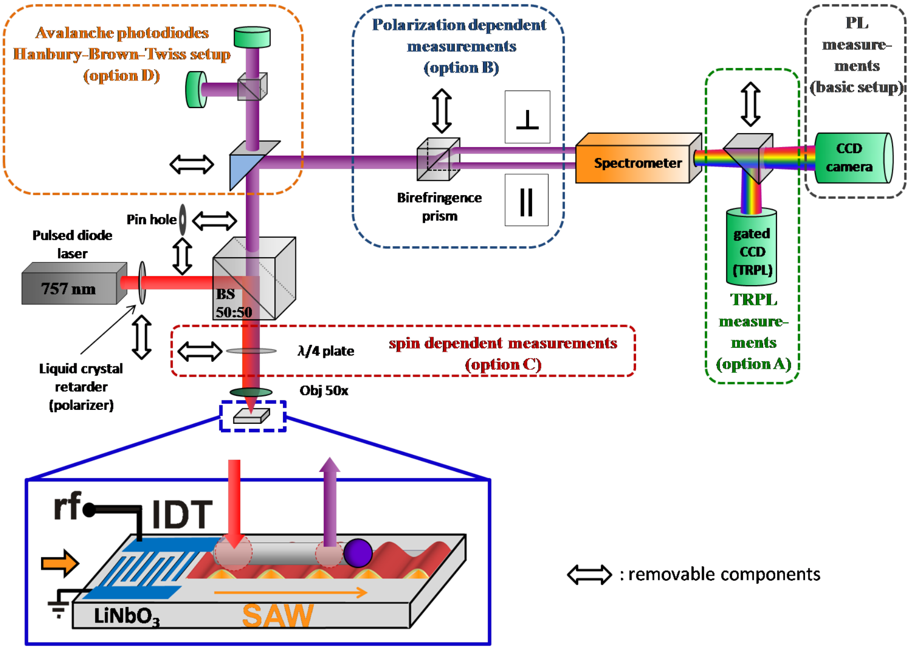

*Figure 3.13.:* Schematic diagram of the setup for the PL measurements on single GaAs and (In,Ga)As/GaAs nanowires. Due to removable components the setup is suitable for PL (basic setup), TRPL (option A), linear polarized PL (option B), spin polarization dependent (option B + C) and photon antibunching measurements (option D).

The time-resolved PL measurements in order to investigate the recombination dynamics of the acoustically transported carriers were performed by a gated CCD camera with a gate time of 500 ps (option A in Fig. 3.13).

For the linear polarized PL measurements, a liquid crystal retarder was used to rotate the incident laser polarization with respect to the nanowire growth axis. The PL emission of the nanowire was split by a birefringence prism into two orthogonally polarized rays (option B in Fig. 3.13). The rays with polarization parallel and perpendicular to the nanowire axis are then detected within one CCD image with the basic setup.

For the spin transport measurements, the same setup as for the linear polarized PL measurements is used. Additionally, a $\lambda/4$ plate was put into the beam path before the objective in order to convert linear polarized light into left-handed circularly polarized one and vice versa (option B + C in Fig. 3.13).

The photon correlation measurements were carried out using a Hanbury Brown and Twiss (HBT) setup consisting of two Si avalanche photodetectors (APDs), each placed at one end of the two output ports of a 50/50 nonpolarizing beam splitter (option D in Fig. 3.13).[**] The following Tab. 3.4 summarizes the different options and parameters of the used setup.

| Setup | Laser | Detector | Sample temperature | Nanowire samples |
|---|---|---|---|---|
| basic | 757 nm | CCD | 20 K | D + E |
| option A | 757 nm | gated CCD | 20 K | D |
| option B | 757 nm | CCD | 20 K | D |
| option B + C | 757 nm | CCD | 20 K | D |
| option D | 757 nm | APDs | 20 K | D + E |

***Table 3.4.:*** Basic parameters for the PL measurements on GaAs (sample D) and (In,Ga)As (sample E) nanowires. The different options correspond to the related setups in Fig. 3.13.

### SAW delay line

The SAW delay line consists of two floating electrode unidirectional transducers [see Fig. A.1(c)] deposited by optical lithography on a 128° rotated Y-cut X-propagating $LiNbO_3$ crystal. These interdigital transducers (IDTs) are designed to generate SAWs at multiple harmonics of the

---

[**] A more detailed description of the HBT effect is given in section 3.3.

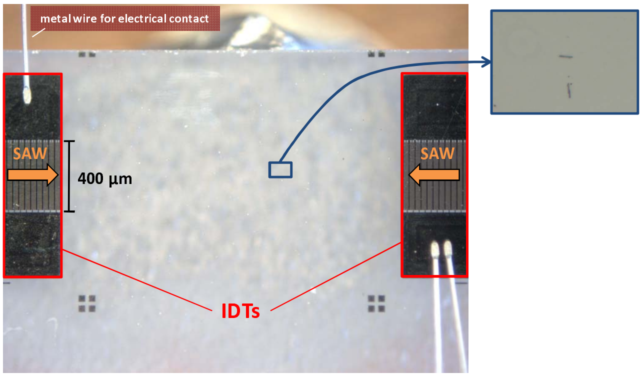

***Figure 3.14:*** The $LiNbO_3$ SAW delay line with two equal IDTs being opposed one to each other in reflection symmetry. The SAW propagation direction of the IDTs is represented by arrows. The inset of the right shows a magnified image of a nanowire aligned with the SAW propagation direction.

fundamental wavelength $\lambda_{\mathrm{SAW}} = 35\,\mu\mathrm{m}$. $LiNbO_3$ single crystals provide a strong piezoelectric field for the manipulation of carriers in semiconductor structures placed on the surface. In addition, they are commonly used as an excellent material for SAW devices (such as filters, oscillators and resonators) and ultrasonic transducers due to the high electro-mechanical coupling factor, low acoustic transmission loss, stable physical and chemical properties. For the experiment the second and third harmonics with $\lambda_{\mathrm{SAW}} = 17.5\,\mu\mathrm{m}$ and $\lambda_{\mathrm{SAW}} = 11.67\,\mu\mathrm{m}$ were used as they show the highest electro-acoustic conversion efficiency. The corresponding frequencies are 220 MHz and 330 MHz at room temperature, respectively. The IDTs have a length of 700 µm and an aperture of 400 µm which is approximately equal to the finger length. The delay line used in this work is displayed in Fig. 3.14. The two equal unidirectional IDTs have been placed opposite to each other on the substrate in reflection symmetry, in such a way that the SAW propagation direction of one IDT is collinear to the other.

In Figs. 3.15(a) and (b), the scattering parameters $s_{11}$ (rf power reflection) and $s_{21}$ (rf power transmission) for these transducers around the 17.5 µm resonance at room temperature are presented. The IDTs have a 3.5 MHz wide emission band, as defined by the frequency range where the transmission is within 3 dBm of its maximum value. The insertion loss of the delay line is 10.6 dBm at the resonance frequency of 226 MHz. Due to the use of two equal IDTs the electro-acoustic conversion efficiency is simply half of the insertion loss determined from the $s_{21}$ maximum rf

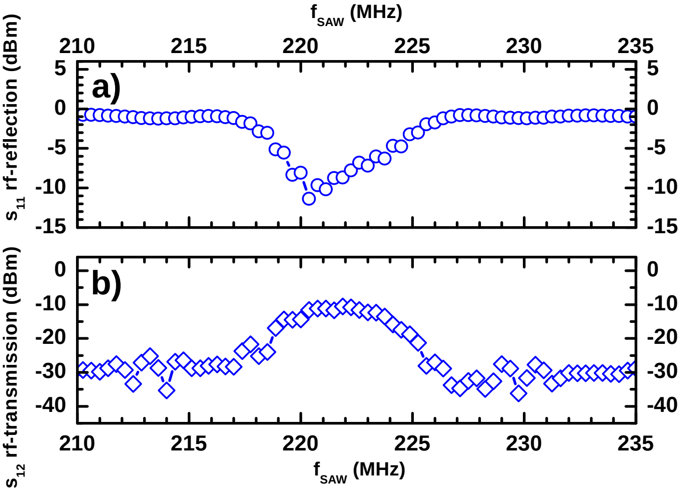

***Figure 3.15.:*** (a) $s_{11}$ rf power reflection coefficient and (b) $s_{21}$ power transmission coefficient of the SAW LinNbO$_3$ delay line.

power transmission, i.e. 5.3 dBm which corresponds to an acousto-electric conversion of 29.5% of the electrical input power applied to the IDT.

## 3.3. Photon correlation measurements

Correlation measurements are often carried out to survey if two events happen independently of each other. This is the case for a single photon source which emits one photon at a time, i.e. no temporal coincidence of emitted photons from the same light source exists. This is generally referred to as *photon antibunching* and is a quantum mechanical effect that does not appear in classical light sources, such as incandescent lamps. Examples for single photon sources are single atoms or quantum dots which have quantized discrete energy states. This can be visualized for an electron in a simplified two level system. If an electron gets excited to the higher energy level, it can return to its ground state by emitting a photon. For a generation of a further photon, however, the electron has to be excited again such that it is impossible to detect two photons together. Such an ideal single photon source is actually difficult to realize since in these structures various energy levels exist and one has to focus

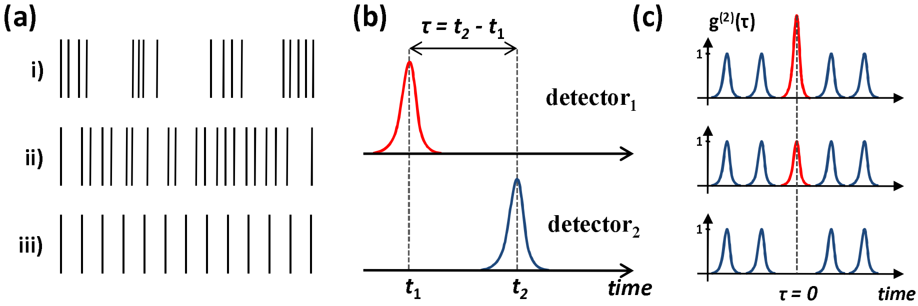

***Figure 3.16.:*** (a) Schematic representation of detected photons for (i) a chaotic (thermal) light source, (ii) a coherent (laser) source and a non-classical (single-photon) source. (b) Emitted photon pulses observed at the detectors after time $t_1$ and $t_2$. (c) Second-order intensity correlation function $g^{(2)}(\tau)$ for a pulsed thermal, coherent and single-photon source, respectively. For $\tau = 0$ the thermal emitter exhibits a high probability to detect bunched photons $g^{(2)}(0) > 1$, the coherent emitter reveals no photon correlation $g^{(2)}(0) = 1$ and the single photon source shows a perfect antibunching $g^{(2)}(0) = 0$.

on one atom or quantum dot requiring a setup to detect very low emission intensities. In order to determine if a light source emits single photons, one measures the second-order intensity correlation function which is defined in the following section.

### 3.3.1. Correlation function

The second-order intensity correlation function gives the likelihood $g^{(2)}(\tau)$ of a second photon observation event at time $t + \tau$ given an initial photon detection at time $t(\tau = 0)$ and is defined as [125]:

$$g^{(2)}(\tau) = \frac{\langle I(t+\tau)I(t)\rangle}{\langle I(t)\rangle^2} \tag{3.26}$$

where $I$ is the average intensity. For an ideal single photon source the likelihood to detect two photons at the same time is zero, i.e. $g^{(2)}(0) = 0$. For a light source with random emission times, e.g. a laser source, $g^{(2)}(\tau)$ is flat and $g^{(2)}(\tau) = 1$ for all $\tau$. If a source has an emission characteristic where $g^{(2)}(0) > 1$ it is referred to as *bunched* since there is an increased probability to detect more than one photon within very short time. This is displayed in Figs. 3.16(a-c). For thermal light sources [(i) in

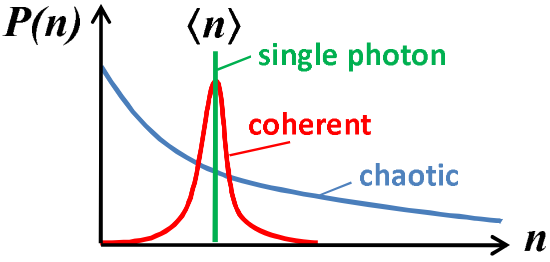

***Figure 3.17:*** Probability $P$ to detect $n$ photons in a given time interval for a chaotic thermal light (blue), a coherent laser source (red) and an ideal single photon source. $\langle n \rangle$ denotes the average amount of detected photons in the time interval.

Fig. 3.16(a)], one observes that photons are correlated and emitted in bunches. This is due to the Bose-Einstein statistics of photons which can describe the photon statistics for very short time scales. In this case, the probability distribution $[P(n)]$ is large and the probability that no photon is detected $[P(0)]$ in short time intervals is highest (see Fig. 3.17). That means that, for example, for an average phonon density $\langle n \rangle = 1$ there exist intervals where no photons are detected and some intervals where more than one photon is detected. For a coherent light source (e.g. laser), the fluctuations in the intervals are much smaller (Fig. 3.17) and the photons are uncorrelated leading to a random distribution of detected photons [(ii) in Fig. 3.16(a)]. In contrast, an ideal single photon source only emits one photon per time with short time intervals between each detected photon [(iii) in Fig. 3.16(a)]. However, in real photon emitter more than one photon is generally generated in average, leading to a non-vanishing correlation function given by

$$g^{(2)}(0) = 1 - 1/\langle n \rangle < 1, \tag{3.27}$$

where $\langle n \rangle$ is the average number of emitted photons. Further detailed information of single photon emission and the photon statistics can be found in the Refs. [125–128].

For the measurement of the second-order intensity correlation function a Hanbury Brown and Twiss setup has been used and will be described in the next section.

### 3.3.2. Hanbury Brown and Twiss setup

This setup proposed by Hanbury Brown and Twiss in 1956 [129] consists of a non-polarizing 50/50 beam splitter and two detectors equally

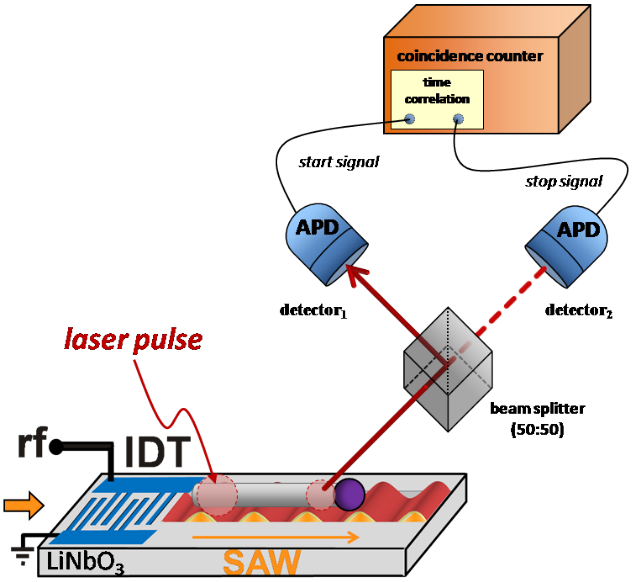

***Figure 3.18:*** Hanbury Brown and Twiss setup. The signal is split by a non-polarizing 50/50 beam splitter in two parts. The detection of a photon with detector$_1$ tiggers detector$_2$ in providing a *start* signal. After the detection of a second photon at detector$_2$ a *stop* signal is sent to the correlator which generates a histogram of the time delay between the detection of the photons and the coincidence of second detected photons.

placed at equal distances from the beam splitter (see Fig. 3.18). As detectors two silicon avalanche photodiodes (APD) have been used. In the measurements, detector$_1$ triggers the detection of detector$_2$, i.e. the arrival of a photon at time $t_1$ at detector$_1$ provides a *start* signal for detector$_2$ that detects a successive photon at time $t_2$ – providing the *stop* signal – with a time delay $\tau = t_2 - t_1$. This is illustrated in Fig. 3.16(b), where the detection of a first pulse (red) at time $t_1$ with detector$_1$ provides the *start* signal for the detection of a second pulse (blue) at time $t_2$ with detector$_2$ and a time delay $\tau$. This has the advantage that the deadtime of one detector is compensated. By measuring the *start/stop* signal, a histogram of the time delay $\tau$ between two photons and the number of second detected photons can be generated. This is displayed in Fig. 3.16(c) for a pulsed light source of a thermal, a coherent and a single photon emitter. $g^{(2)}(\tau)$ is depicted as a function of the time delay $\tau$ between the detection of the first photon at detector$_1$ and the second photon at detector$_2$. For $\tau \approx 0$, the thermal emitter exhibits a high probability of bunched photons [$g^{(2)}(0) > 1$] due to the fluctuations of the thermal source, whereas the coherent emitter reveals a random distribution without photon correlation [$g^{(2)}(0) = 1$] and the single photon source an ideal antibunching behavior [$g^{(2)}(0) = 0$].

When detector$_1$ is triggered by the laser pulses, the same setup can be used to record time-resolved PL profiles of the emission.

# 4. Optical properties of InAs nanowires

In this chapter, the experimental results for InAs nanowires are presented. The fundamental issue, here, is the determination of the optical properties of wurtzite InAs nanowires. Since scarce experimental data has been reported on the optical phonons and the band gap of wurtzite InAs so far, this is currently a hot topic. A reason for the small amount of experimental publications are, on the one hand, the flat transverse optical (TO) phonon dispersion for zincblende InAs – which results in similar phonon energies for the wurtzite $A_1$(TO), $E_1$(TO) and $E_2^H$ modes (as illustrated in Fig. 3.4) and complicates their determination (see Sec. 4.1.2) – and, on the other hand, the fundamental gap energy in the infrared region ($\sim$ 3 μm) – infrared photodetectors in the near to middle infrared region possess a much lower optical efficiency and lower signal-to-noise ratio than, for example, Ge detectors. The latter has particular importance for PL measurements on single InAs nanowires where the emission is weak due to the reduced dimensions. Therefore, PL measurements have been carried out on InAs nanowire ensembles. PL experiments on single InAs nanowires has not been published so far and are still a challenge to be overcome.

In the next section, the experimental Raman scattering from single InAs nanowires has been investigated. Then, the PL results for InAs nanowire ensembles are presented. In a final section, the results will be summarized.

## 4.1. Raman scattering on single InAs nanowires

This section is focused on the Raman scattering on single InAs nanowires. All measurements were performed in backscattering configuration (see Fig. 3.7) where the wave vectors of the incident and scattered light ($k_\mathrm{i}$, $k_\mathrm{s}$) are collinear. In addition, both have been always kept perpendicular to the nanowire axis. Unless otherwise stated, the results have been obtained from sample C from which one representative nanowire has been investigated intensively. The advantage of nanowires from this sample is their large length which facilitates their optical search and alignment prior to the Raman measurements. Similar measurements of single nanowires from sample A and B have also been performed. However, when their results are discussed in the text, an explicit mention to the source sample is given.

In the first subsection, the experimental resonant Raman scattering results on InAs nanowires are presented. They shed light on the electronic properties of the nanowires due to the enhancement effect close to electronic band transitions. These results are compared with an ab-initio calculation of the electronic band structures of zincblende and wurtzite InAs. Then, the experimental polarized Raman scattering results are addressed. First-order Raman scattering allows to access the optical phonon modes at the Γ point and gives information about the structure of the investigated material since the crystal structure belongs to a certain symmetry which emerges in the symmetry of the Raman tensor [130]. Finally, the observation of a surface optical (SO) phonon is presented.

### 4.1.1. Resonant Raman scattering

As mentioned in Sec. 3.1.1, the Raman scattering intensity is enhanced when the exciting laser energy is close to an electronic band transition in the investigated material. It is predicted that the electronic band structure of the zincblende phase of InAs is different from the wurtzite one of the same material [48, 54] which leads to different transition energies. In the following, it will be focused on the $E_1^{\mathrm{G}}$ transition of InAs whose energy is in the range of laser excitation energies used in this work. Ab-initio calculations of the electronic band structure, using the WIEN2k code [131] with a modified Becke-Johnson (mBJ) potential [132], along the [0001] growth direction of the wurtzite phase [from Γ to A, Fig. 4.1(a)] and along the [111] growth direction of the zincblende phase [from Γ to L, Fig. 4.1(b)] have been performed by Luis C. O. Dacal* in order to give theoretical background to these experimental results. The arrows in Fig. 4.1 denote the energy separation at the corresponding symmetry

---

[*] Owing to a collaboration with the *Instituto de Estudos Avançados (IEAv)*, CTA, São José dos Campos, SP, Brazil.

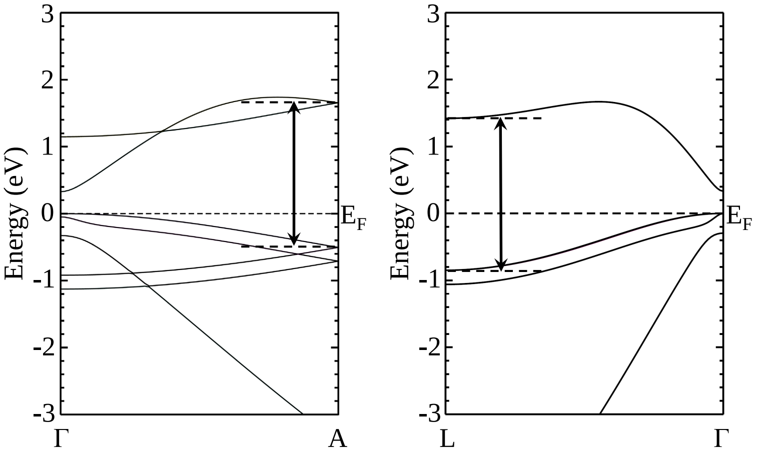

*(a)* Wurtzite *(b)* Zincblende

***Figure 4.1.:*** Ab-initio calculations of the electronic band structure of wurtzite (a) and zincblende (b) InAs along the directions Γ-A and Γ-L, respectively. The arrows denote the electronic transition energies at the corresponding symmetry points.

points. The calculations reveal a transition energy for the zincblende structure of approximately 110 meV larger than for the wurtzite structure. The $E_1^{\mathrm{G}}$ transition of the cubic crystal structure takes place close to the L point between two parallel sections in the band structure [Fig. 4.1(b)]. As seen in Sec. 3.1.2, the wurtzite structure from Γ to A can be approximated by simply folding the one for the zincblende phase from from Γ to L. This folding leads to parallel sections in the band structure near the A point of the wurtzite phase, as can be seen in the calculations [Fig. 4.1(a)]. Thus, the $E_1^{\mathrm{G}}$ transition is expected to occur close to the A point and to be approximately 110 meV smaller than that of the zincblende phase.

Resonant Raman scattering has been measured in order to determine the $E_1^{\mathrm{G}}$ transition energies. A typical Raman spectrum in $x(y,y)\bar{x}$ configuration[†] is shown in Fig. 4.2(a). Besides, the clearly visible TO and longitudinal optical (LO) mode, a surface optical (SO) mode, which will be discussed later, also appears. To determine the resonance, the Raman

---

[†] The Porto notation is described in footnote ¶ on page 36.

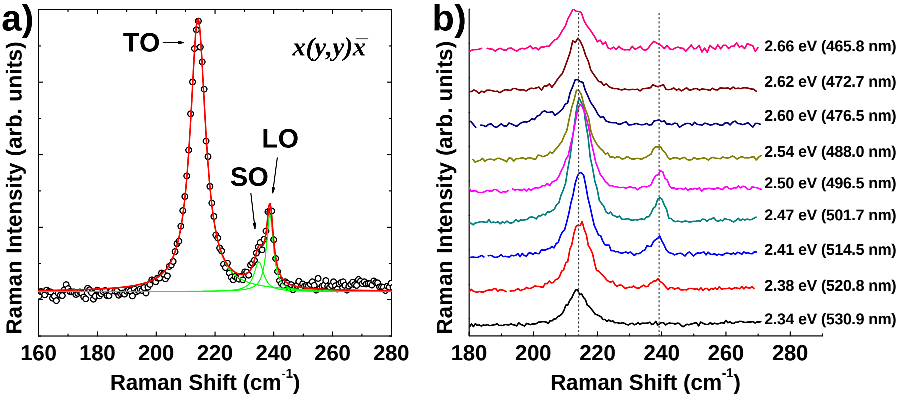

***Figure 4.2.:*** (a) Typical Raman spectrum in $x(y,y)\bar{x}$ configuration from an InAs nanowire using the 514.5 nm excitation line. Beside the TO and LO mode, a SO mode appears. (b) Series of Raman spectra from an InAs nanowire measured as a function of the laser energy. A resonance enhancement of the TO and LO modes is clearly visible. The dashed lines serve as a guide to the eye.

measurements were performed with nine lines of the Ar/Kr ion laser (2.34 – 2.66 eV) on a single nanowire. A series of Raman spectra, measured as a function of the laser excitation energy, is shown in Fig. 4.2(b). The spectra were taken in a parallel polarization configuration $x(y,y)\bar{x}$. All spectra were corrected according to the $\omega^4$ law (Eq. 3.7). Two modes at $214\,\text{cm}^{-1}$ (TO) and $239\,\text{cm}^{-1}$ (LO) can be clearly identified. All measured spectra were fitted with Lorentzian functions after the removal of the background contribution.

For the four main polarization configurations [$x(y,y)\bar{x}$, $x(y,z)\bar{x}$, $x(z,y)\bar{x}$ and $x(z,z)\bar{x}$, see Fig. 4.3], the integrated Raman intensities of the TO mode (open symbols) as a function of the laser excitation energy is shown in Fig. 4.4(a). The standard deviation of at least three measurements is used as error bar.[‡] The integrated Raman intensities of the LO mode is displayed only for the $x(y,y)\bar{x}$ configuration (cross symbols) due to

---

[‡] For every excitation energy the Raman intensity was measured at least three times. Since the diameter of the nanowires (50 – 200 nm) is very small, the Raman scattering intensity depends crucially on the laser spot position on the nanowire and the mechanical stability of the system. To get a representative picture, every repetition was performed after new alignment of the laser spot on the nanowire.

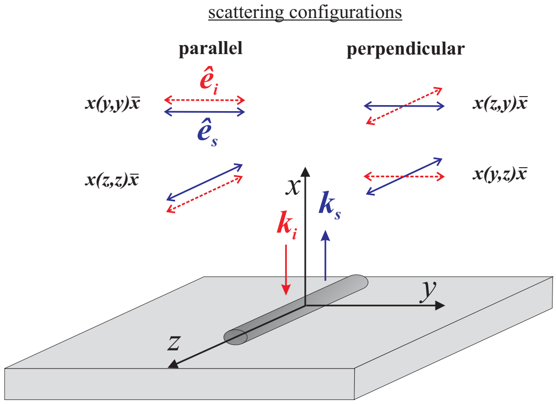

***Figure 4.3:*** The four main polarization configurations used in this work. The wave vectors $\mathbf{k}_\mathrm{i}$ and $\mathbf{k}_\mathrm{s}$ of the incident and scattered light, respectively, are perpendicular to the lying nanowire on the substrate. The corresponding light polarizations are denoted $\hat{e}_\mathrm{i}$ and $\hat{e}_\mathrm{s}$, respectively. In the parallel configurations $[x(y,y)\bar{x}$ and $x(z,z)\bar{x}]$ the incident and scattered light are parallel to each other while in the crossed configurations $[x(y,z)\bar{x}$ and $x(z,y)\bar{x}]$ they are perpendicular to each other.

the vanishing Raman signal in other configurations. The data were corrected with respect to the different responses of the grating and the beam splitter due to the different polarizations and incident laser excitation wavelengths $\lambda_\mathrm{L}$. For the parallel polarization configurations $[x(y,y)\bar{x},\ x(z,z)\bar{x}]$, an enhancement of the Raman scattering intensity for the TO mode with a maximum at 2.47 eV (Gaussian fit) is observed, whereas for the crossed polarization configurations $[x(y,z)\bar{x},\ x(z,y)\bar{x}]$ the Raman signal is within the noise. Figure 4.4(b) shows as a reference the integrated Raman scattering intensities from zincblende InAs bulk with a peak at 2.57 eV in agreement with previous publications [133–136]. The resonance energy obtained experimentally for the nanowire is red-shifted as compared to the one obtained for bulk zincblende InAs. Additional resonant Raman measurements on a single nanowire of sample A under the same conditions reveal a resonance maximum at 2.45 eV in $x(y,y)\bar{x}$ configuration (see Appendix C, Fig. C.1) supporting the observed red-shift.

These values are consistent with the calculated energy difference of $\sim 110\,\mathrm{meV}$ between the $E_1^\mathrm{G}$ transitions of the zincblende and wurtzite structures. The integrated Raman intensities of the LO mode corroborate the result. However, due to the reduced signal intensity ($\sim$0.25 counts/s in resonance), the LO phonon can mostly be observed in the $x(y,y)\bar{x}$

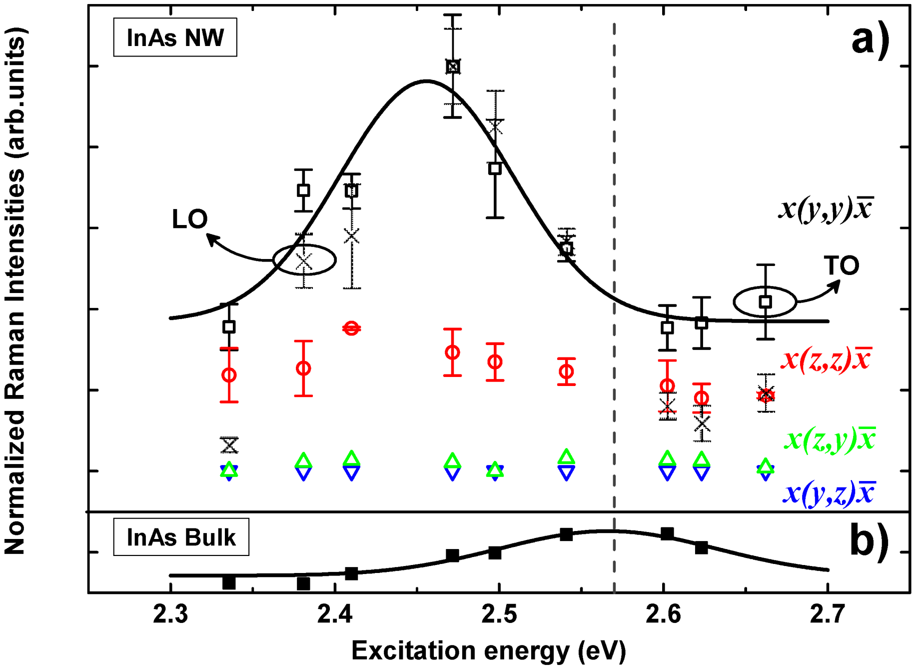

***Figure 4.4.:*** (a) Resonant Raman scattering from an InAs nanowire as a function of the laser excitation energy for the TO mode in the four main polarization configurations (open symbols) and the LO mode in $x(y,y)\bar{x}$ configuration (cross symbols, ×). The solid line represents a Gaussian fit to the open squares. The standard deviation of at least three measurements is used as error bars. (b) Reference measurement from InAs bulk material (filled squares).

configuration and disappears far from resonance (see Fig. 4.2(b)). This behavior is due to the Fröhlich interaction which describes the coupling of excitons with the macroscopic electric field generated by a LO phonon in a polar semiconductor [108]. The coupling provokes that the forbidden LO phonon in wurtzite structure (see Sec. 3.1.2) can be activated and strongly enhanced near resonances [137], particularly when the incident and scattered light polarizations are parallel to each other [138]. It was found that the enhancement in resonance of forbidden LO phonon modes can even be stronger than the one for allowed (according to the selection rules in Sec. 3.1.2) LO phonons [138]. This makes the forbidden LO phonon very sensible to resonances [cf. Fig. 4.4(a)]. However, the appearance of the LO mode only in $x(y,y)\bar{x}$ configuration, a configuration where the LO phonon is allowed for certain rotation angles $\theta$ in the zincblende structure (see Fig. 3.3), may indicate that the Raman signal comes from the zincblende phase. A slight contribution of this phase cannot be excluded due to the presence of zincblende stripes in the nanowires, but the complete disappearance of the LO mode far from resonance for the $x(y,y)\bar{x}$ configuration (see Fig. 4.2(b)) suggests that the origin stems from the forbidden LO phonon of the wurtzite phase.

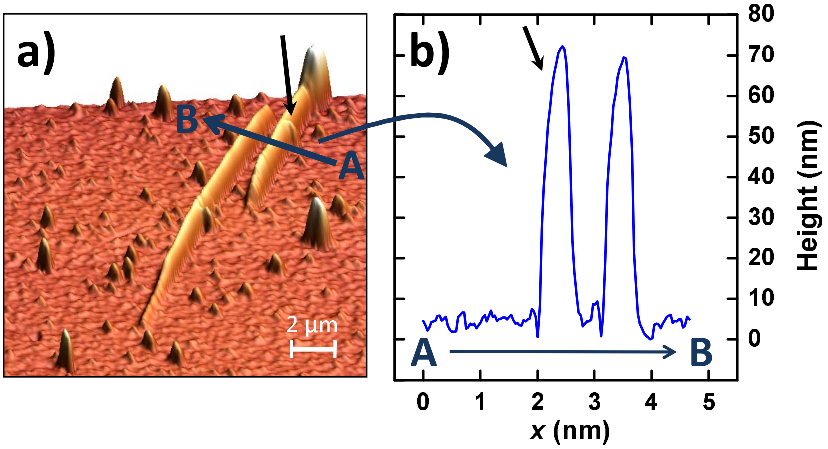

***Figure 4.5.:*** (a) AFM image of the investigated nanowire (black arrow) after the nanowire has been unintentionally cut and moved along the sample by the AFM tip. (b) Height profile of the nanowires in (a) along the blue line.

Furthermore, the investigated nanowire has been studied by atomic force microscopy (AFM) in order to determine its diameter. During the measurements the nanowire has been unintentionally cut and moved by the AFM tip. The obtained AFM image of the investigated nanowire (black arrow) is displayed in Fig. 4.5(a) and shows that the damages have not affected the rod-like shape of the nanowire. The diameter can be taken from the height profile in Fig. 4.5(b), along the blue line in Fig. 4.5(a), and has been determined to 70-80 nm in average. This excludes confinement or strain effects in this nanowire.

### 4.1.2. Polarized Raman scattering

In this section, the experimental polarized Raman scattering results are presented. Initially, polarized Raman scattering in backscattering geometry on a bulk InAs (110) substrate has been performed in order to get a reference measurement. The polar patterns for the experimental results of the TO and LO phonon are shown in Figs. 4.6(a) and (b), respectively. The experimental data for the TO mode show good agreement with the theoretical results obtained in Sec. 3.1.2. For comparison the calculated polar pattern from Fig. 3.2 is reproduced in Fig. 4.6(c). The small shifts of the TO intensity maxima of about 8° are attributed to an inclination of the polarization direction of the light with respect to the crystallographic axis of the substrate. The selection rules for the LO mode – forbidden from a (110) surface – are not fulfilled. This is attributed to the fact that the laser excitation energy (2.41 eV) is close to the $E_1^{\mathrm{G}}$ Raman transition of InAs bulk (2.57 eV) which provokes the appearance of the forbidden LO mode due to the Fröhlich interaction, as mentioned before.

In the following, the results of the Raman scattering experiments from the same individual InAs nanowire investigated in the previous section are presented. A typical Raman spectrum has been displayed in Fig. 4.2(a). All measured spectra were fitted with Lorentzian functions after the removal of the background contribution. The standard deviation of at least three measurements is used as error bar. Although the experimental linewidths of the measured TO modes ($\sim 6 - 13\,\mathrm{cm^{-1}}$) for distinct scattering configurations are too large for a direct identification of the different wurtzite modes, the detailed polarization dependence analysis performed provides useful information on this regard. In Fig. 4.7, the polar pattern of the InAs nanowire with the 514.5 nm excitation line for the TO mode (a) and the LO mode (b) are displayed. For both the TO and LO modes, the measured intensities for a perpendicular ($I_\perp$) and parallel ($I_\|$) analyzer [cf. Fig. 4.6(d)] are normalized to the highest measured mode intensity under perpendicular analysis. Here, the measured TO mode intensity is a factor of 10 higher than the LO intensity. Additional similar measurements of the TO and LO mode with a fixed incident polarization and a rotational analyzer [$x(z,\phi)\bar{x}$, $x(y,\phi)\bar{x}$, cf. Fig. 3.7] on the same nanowire have led to the same results – expected due to symmetry.

The results shown in Fig. 4.7(a) reveal that the TO mode is detected

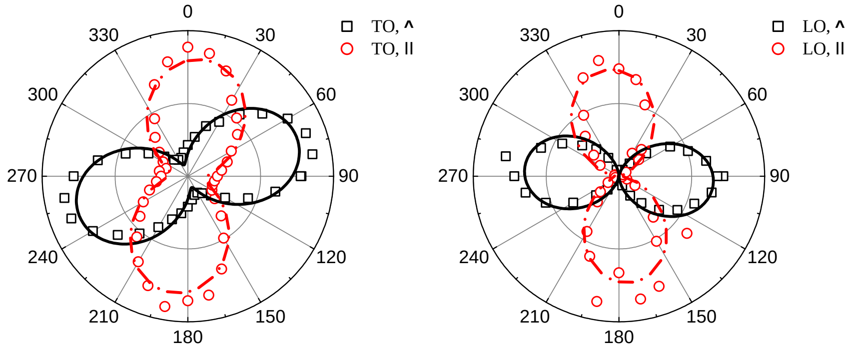

***(a)*** Experimental InAs(110) TO ***(b)*** Experimental InAs(110) LO

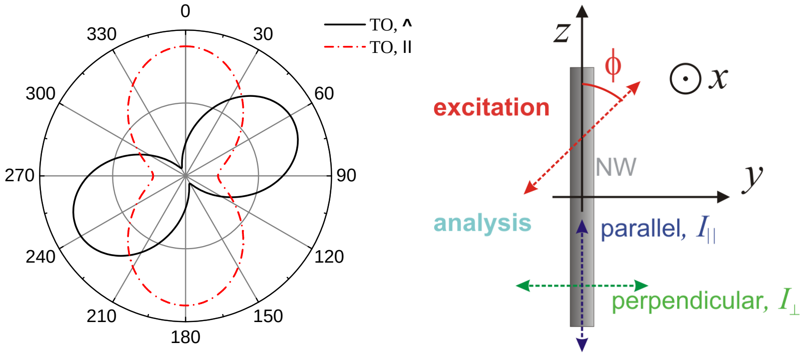

***(c)*** Calculated InAs(110) TO ***(d)*** Scattering geometry

***Figure 4.6.:*** Polarized Raman scattering of the TO mode (a) and the LO mode (b) measured for a reference bulk InAs (110) substrate excited with the 514.5 nm Ar line. Open squares and spheres represent the experimental Raman scattering intensities for perpendicular ($I_{\perp}$) and parallel ($I_{||}$) analysis with respect to the [111] direction. Solid curves are squared cosine fits to the data. (c) Corresponding calculated polar pattern for the TO mode (cf. Fig. 3.2). The LO mode is forbidden from a (110) surface. (d) Scattering geometry of the measurements. The incident light polarization (red) is rotated by the angle $\phi$ with respect to the nanowire axis $z$. The scattered light is detected by a analyzer set perpendicular ($I_{\perp}$, green) or parallel ($I_{||}$, blue) to the wire axis.

much stronger in parallel configurations $[x(y,y)\bar{x},\ x(z,z)\bar{x}]$, i.e. when the incident and the scattered light polarizations are parallel to each other. Additionally, the observed intensity in $x(y,y)\bar{x}$ configuration is much higher than in $x(z,z)\bar{x}$ configuration. This is consistent with the resonant Raman scattering results in the last subsection where the resonance enhancement of the Raman signal was obtained only for parallel configurations. These results are in accordance with the calculated polar patterns for the $A_1$(TO) and $E_2$ modes [Figs. 3.5(a) and 3.5(c)] from Sec. 3.1.2 reproduced for comparison in Figs. 4.7(c) and 4.7(e), respectively. Therefore, we attribute the denoted TO signal to the combined signal coming from the $A_1$(TO) and $E_2^{\mathrm{H}}$ modes. Note that the maximum Raman intensity for $I_\perp$ is higher than for $I_\parallel$ since for $I_\perp$ both modes contribute to the Raman signal [solid curves in Figs. 4.7(c) and 4.7(e)] while for $I_\parallel$ only the $A_1$(TO) mode accounts for the polar pattern [dashed curve in Fig. 4.7(c)]. Furthermore, the $E_1$(TO) mode, that theoretically contributes in crossed polarization configurations [Fig. 4.7(d)], does not appear in these experiments. The reason for this is still unclear. The Raman intensities for the TO mode [Fig. 4.7(a)] exhibit a weak signal for crossed polarization configurations {cf. $\phi = 90°, 270°$ for $I_\parallel$ [$x(y,z)\bar{x}$] and $\phi = 0°, 180°$ for $I_\perp$ [$x(z,y)\bar{x}$]} which do not appear in the calculated polar patterns for the $A_1$(TO) and $E_2$ modes where $I_\parallel$ and $I_\perp$ are zero [cf. Figs. 4.7(c) and (e)]. The weak signal may be due to a low contribution of the $E_1$(TO) mode since this is the only mode allowed in these configurations [see Fig. 4.7(d)]. Indeed, the calculated $A_1$(TO), $E_1$(TO) and $E_2^{\mathrm{H}}$ phonon modes presented in Tab. 3.2, which exhibit a maximum splitting of 6.8 cm$^{-1}$, suggest that all modes emerge together in the observed TO mode with experimental line-width between 6 and 13 cm$^{-1}$. However, more measurements are needed to clarify this issue. Low temperature Raman measurements, for example, reduce the experimental line-width of the modes and may allow to resolve the different phonon modes and their exact frequencies.

A contribution to the Raman signal coming from the zincblende portions of the nanowire, although cannot be completely ruled out in both the TO and LO peaks, is believed to be marginal, except for $x(z,z)\bar{x}$ configuration. For cubic GaAs nanowires grown in [111] direction, it was reported that the TO Raman signal is much stronger for the $x(z,z)\bar{x}$ than any other configuration [139]. A contribution is, therefore, mainly expected in that configuration. To investigate if the zincblende sections in the nanowire contribute to the signal, the Raman shift and the full width of half maximum (FWHM) of the TO mode, displayed in Figs. 4.8(a) and (b),

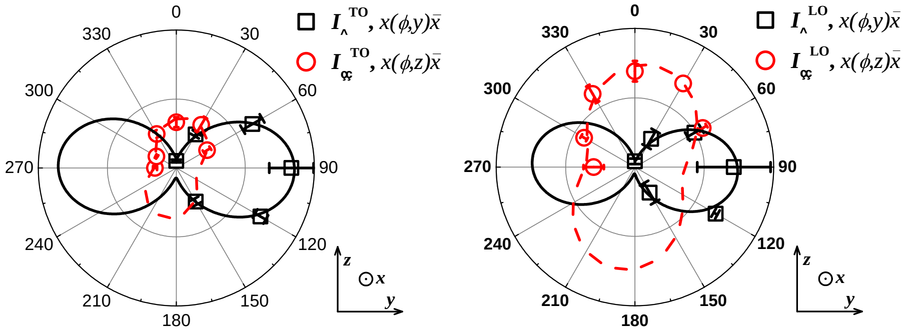

***(a)*** TO mode ***(b)*** LO mode

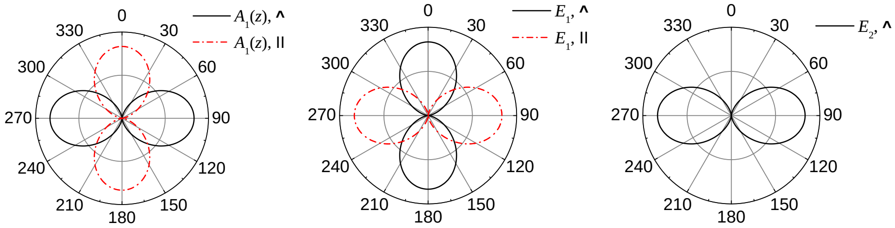

***(c)*** A₁(TO) mode ***(d)*** E₁(TO) mode ***(e)*** $E_2$ mode

***Figure 4.7.:*** Experimental polar patterns for the TO (a) and LO (b) mode for a nanowire from sample C and excitation line of 514.5 nm. Solid and dashed curves are $\cos^2(\phi)$ fits to the data. $\phi$ denotes the angle between the polarization of the incident light and the nanowire axis. Open squares and spheres represent the perpendicular and parallel analysis of the scattered light with respect to the nanowire axis (oriented along $z$, $\phi = 0\,°$). The standard deviation of at least three measurements is used as error bars. Corresponding calculated polar patterns for the $A_1$ (c), $E_1$ (d) and $E_2$ (e) modes (cf. Fig. 3.5).

are considered. It can be seen that the TO mode is constant for all configurations, but $x(z,z)\bar{x}$ ($\phi = 0°$). In this configuration, the TO peak shifts to higher wavenumbers and it gets broadened. The shift may be due to a contribution from the zincblende phase since the zincblende TO phonon (bulk) is located at higher wavenumbers (217.3 cm$^{-1}$ [140]). Indeed, the broadening of the peak (almost doubled) suggests that there are two contributions to the Raman signal in $x(z,z)\bar{x}$ configuration which most likely originate from the TO mode of the zincblende structure and the

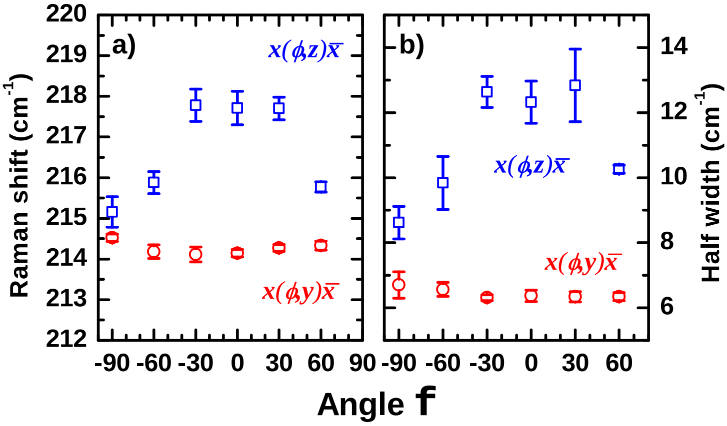

***Figure 4.8.:*** (a) Phonon frequencies and (b) the full width at half maximum of the TO mode as function of the angle $\phi$ between the polarization of the incident light and the nanowire axis. For $x(z,z)\bar{x}$ ($\phi = 0°$) configuration, the TO mode shifts to higher wavenumbers and gets broadened.

$A_1$(TO) mode of the wurtzite phase. A combination of these modes to the signal can explain the shift and the broadening of the peak. A contribution of the zincblende TO mode in other configurations can be excluded or is marginal since it is located at higher wavenumbers (approximately 217.3 cm$^{-1}$) and no peak shift can be observed in these configurations. Furthermore, the constant FWHM suggests only a contribution from the wurtzite phase. This corroborates the observations obtained in zincblende GaAs nanowires [139], where the TO Raman signal is much stronger for the $x(z,z)\bar{x}$ than any other configuration.

The polarization dependence of the much less pronounced LO peak shown in Fig. 4.7(b) also displays maximum intensities for detection under parallel configurations [$x(y,y)\bar{x}$, $x(z,z)\bar{x}$]. Taking into account only the symmetry of the wurtzite structure, the LO mode should not be present in backscattering experiments. The breaking of this selection rule is attributed to the fact that in these measurements the excitation energy (2.41 eV) is in the vicinity of the $E_1^G$ electronic transition of the wurtzite structure. As seen in the last section, the $E_1^G$ transition of the investigated nanowire is red-shifted by 100 meV from the bulk value (2.57 eV). The resonance (2.47 eV), shifted towards the laser excitation energy (2.41 eV), intensifies the appearance of the forbidden LO modes due to the high sensitivity of the LO phonon near resonances. Moreover, the ratio between the integrated intensity of the LO and the TO modes, obtained for the nanowire, is twice as large as the one obtained for the bulk InAs since the excitation energy of 2.41 eV used in these experiments is much closer to the $E_1^\mathrm{G}$ transition in the nanowire than to that in bulk InAs. Thus, the red-shift of the $E_1^\mathrm{G}$ resonance is likely to activate the $\mathrm{A}_1$(LO) and $\mathrm{E}_1$(LO) modes of the wurtzite structure.

### Surface optical phonon

For most semiconductors, the atoms are covalently bonded which leads to various dangling bonds or reconstructions at the surface. This affects the surface phonons and changes their energies. Surface optical (SO) phonons have been studied in thin films [141] and microcrystals [142] and, recently, more attention has been devoted to nanowires. It has been showed that the shape (diameter [143] and the cross section [24]) of the nanowire, the surrounding medium [144] and the defect density [145] of the nanowire influences the SO mode. Thus, the SO mode shifts to lower wavenumbers when decreasing the diameter of the nanowire.

As mentioned before in Fig. 4.2(a), a third mode at the low frequency side of the LO mode can be observed and is assigned to the SO mode of InAs nanowires [145, 146]. A polarized Raman study on this mode reveals that it only appears in parallel configuration $x(y,y)\bar{x}$ where the incident and scattered light polarization are perpendicular to the wire axis [Fig. 4.9(b)]. Although the polar pattern resembles the one for the $E_2$ mode presented before [see Fig. 3.5(c)], the $E_2$ mode can be excluded since its frequency (see Tab. 3.2) is well below the frequency of the SO mode ($\omega_\mathrm{SO}$ = 235.3 cm$^{-1}$) observed in our measurements. A possible contribution due to two-phonon processes can be ruled out as well because of the low two-phonon density of states (DOS) at this frequency. The two-phonon DOS was calculated by the extended 11-parameter rigid-ion-model mentioned in Sec. 3.1.2 and is shown in Fig. 4.9(a).

Scarce data is available regarding polarized Raman scattering on SO phonons. An SO study of a closepacked 2D array of CdSe nanorods reveals a suppression of the SO phonon when the incident light polarization is perpendicular to the wire axis [147]. This is explained by the modification of the dielectric surrounding due to the closed packing of the nanowires, different from the single nanowire study presented here. In wurtzite GaAs needles, an SO phonon has been proposed in $x(y,y)\bar{x}$ and $x(z,y)\bar{x}$ configuration, but could not be resolved [148]. From individual GaP nanowires it is observed that the SO phonon appears strongest in $x(y,y)\bar{x}$ configuration [149] which is in agreement with our observations.

For an infinitely long cylindrical nanowire, the SO frequency $\omega_{\mathrm{SO}}(q)$ (in the limit where the phonon wave vector $q \gg \omega/c$) can be calculated by the following equation [144]:

$$\omega_{\mathrm{SO}}^2 = \omega_{\mathrm{TO}}^2 + \frac{\tilde{\omega}_{\mathrm{p}}^2}{\epsilon_\infty + \epsilon_{\mathrm{m}} f(x)}; \qquad x = qr, \tag{4.1}$$

where $\tilde{\omega}_{\mathrm{p}}$ is the screened ion plasma frequency given by $\omega_{\mathrm{LO}}^2 = \omega_{\mathrm{TO}}^2 + \tilde{\omega}_{\mathrm{p}}/\epsilon_\infty$, $r$ the radius of the nanowire, $\epsilon_\infty$ the high-frequency dielectric constant of bulk InAs and

$$f(x) = \frac{I_0(x)K_1(x)}{I_1(x)K_0(x)}, \tag{4.2}$$

where $I$ and $K$ are the modified Bessel functions. The calculated dispersion relation $\omega_{\mathrm{SO}}$ as a function of the radius $r$ is plotted in Fig. 4.9(c) considering $q = 2k = 4\pi/\lambda_{\mathrm{L}}$ in backscattering geometry. For the case of InAs nanowires, we used $\epsilon_\infty = 12.25$ [140], $\epsilon_{\mathrm{m}} = 1$ (air) and $\lambda_{\mathrm{L}} = 514.5\,\mathrm{nm}$ (laser wavelength). If the nanowire diameter (70 – 80 nm) measured by AFM (see Fig. 4.5) is assumed, one obtains the SO frequency $\omega_{\mathrm{SO}} = 233.5 \pm 0.3$ cm$^{-1}$, which is slightly lower than the frequency observed experimentally ($235.3 \pm 0.5$ cm$^{-1}$).

Another explanation for the appearance of this mode may be the LO-phonon-plasmon coupling. Due to the presence of an electron surface accumulation layer in InAs [150, 151] (the Fermi level gets pinned at the surface above the conduction band minimum), high free electron concentrations exist at the surface which can couple with LO phonons leading to coupled LO-phonon-plasmons [152, 153]. In highly $n$-doped InAs nanowires, an intense mode, located at approximately 233 cm$^{-1}$, has been observed by Raman spectroscopy which has been attributed to a coupled LO-phonon-plasmon mode [154]. This mode is very close to the one observed in this work. However, their nanowires exhibit high doping

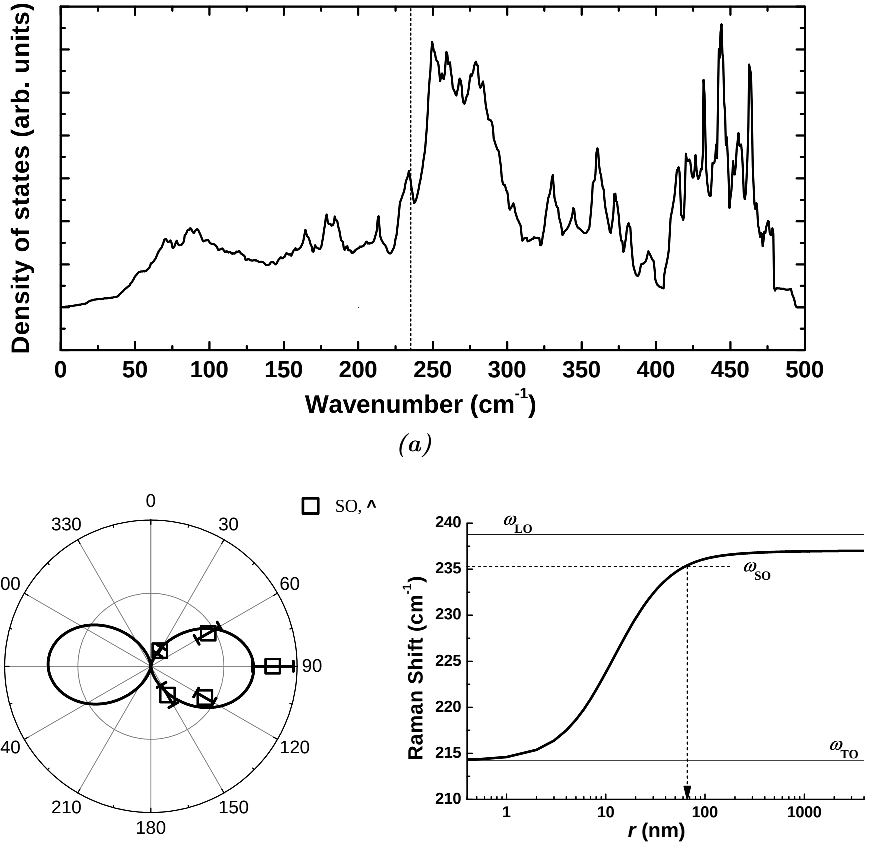

*(a)*

*(b)* *(c)*

***Figure 4.9.:*** (a) Two phonon density of states (DOS) of wurtzite InAs calculated by an extended 11-parameter rigid-ion model. The dashed line represent the frequency of the SO mode observed in our measurements. (b) Experimental polar pattern for the SO mode for an InAs nanowire. The solid curve is a $\cos^2(\phi)$ fit to the data. $\phi$ denotes the angle between the polarization of the incident light and the nanowire axis. Open squares represent the perpendicular analysis of the scattered light with respect to the nanowire axis. The standard deviation of at least three measurements is used as error bars. (c) Calculated SO frequency $\omega_{\mathrm{SO}}$ as a function of the diameter for an InAs nanowire. The horizontal lines represent the TO and LO mode at the zone center and the dashed line the experimental SO frequency.

and the small diameters (15 nm and 40 nm in average) are in contrast to the investigated InAs nanowire in this work (no intentional doping and diameter of 70 – 80 nm).

Altogether, the obtained results about the observed shoulder suggest the attribution to an SO mode, although further experiments would be helpful to achieve a completely unambiguous identification. For instance, a definitive experiment would be the Raman measurement of the nanowire surrounded by different dielectric media ($\epsilon_{\mathrm{m}}$) in which this feature should be shifted as indicated by Eq. 4.1.

## 4.2. Photoluminescence of InAs nanowire ensembles

In this section, the PL results of the InAs nanowire samples A and B are presented. It will be shown that the excitation power and temperature dependent PL measurements of the two InAs nanowire ensembles are in good agreement with the type-II band alignment between the wurtzite and zincblende nanowire sections predicted theoretically. From these results a lower bound for the band gap energy of the InAs wurtzite structure – a hot topic in literature with very few experimental works reported so far – will be estimated. Similar PL measurements have been carried out for sample C. However, the identification of the InAs emission bands were hampered by additional emission centers stemming from the substrate of this sample in the same spectral range.

A few works have adressed the wurtzite band gap of InAs so far. The known theoretical studies predict a wurtzite band gap that is 40 meV [47], 55 meV [48] and 66 meV [54] higher than the one of the zincblende phase. The experimental work of Trägårdh *et al.* has predicted a wurtzite band gap of 0.54 eV by extrapolating fitted photocurrent measurements on $\mathrm{InAs}_{1-x}\mathrm{P}_x$ nanowires[59] and Bao *et al.* have observed a value of 0.52 eV in two-dimensional-like wurtzite structures [60]. More recently, Sun *et al.* have reported the first photoluminescence (PL) characterization of pure wurtzite InAs nanowires in which the observed blue-shifted band gap has been assigned to quantization effects rather than to the difference in crystal structures due to the small diameters of the nanowires [155].

The basic setup of the PL measurements are presented in Fig. 3.12.

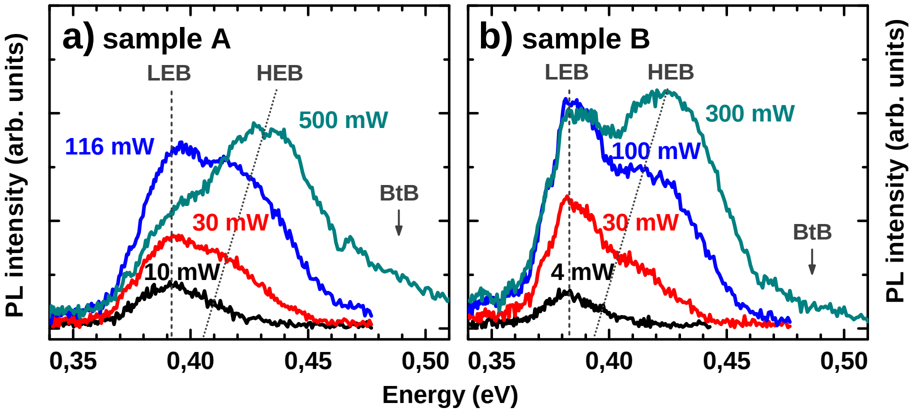

***Figure 4.10.:*** The PL spectra for different excitation powers measured at 5 K are shown from (a) sample A and (b) sample B. Two optical emission bands (LEB, dashed line and HEB, dotted line) can be clearly observed in both samples. For high excitation power a shoulder at the high energy side (BtB) can be identified.

In Fig. 4.10, the PL spectra from sample A [Fig. 4.10(a)] and sample B [Fig. 4.10(b)] measured for different excitation powers at 5 K are presented. Two optical emission bands are observed in both samples. The low energy emission band (LEB, dashed line) does not shift with increasing excitation power while for the high energy emission band (HEB, dotted line) a pronounced blue-shift is detected. In both samples, LEB dominates at low excitation power and HEB dominates for high power, suggesting a saturation effect of the LEB at high excitation power. Additionally, for high excitation power a shoulder at the high energy side (denoted BtB) is identified which has an emission energy of 0.488 eV, far above the zincblende band gap energy of 0.415 eV [156].

The PL spectra at different positions on both samples were fitted with various Gaussian functions. The data between 0.445 eV and 0.485 eV and between 0.369 eV to 0.375 eV were not included in the fit in order to avoid contributions from the water absorption band and a sharp substrate emission band, respectively. The obtained PL peak energies are depicted in Fig. 4.11(a). As mentioned before, for high excitation power the LEB saturates [see Fig. 4.11(c)]. This suggests that impurity-like recombination processes are involved, as previously reported for donor-acceptor pair and band-to-acceptor transitions in bulk InAs [157, 158]. Therefore, the LEB

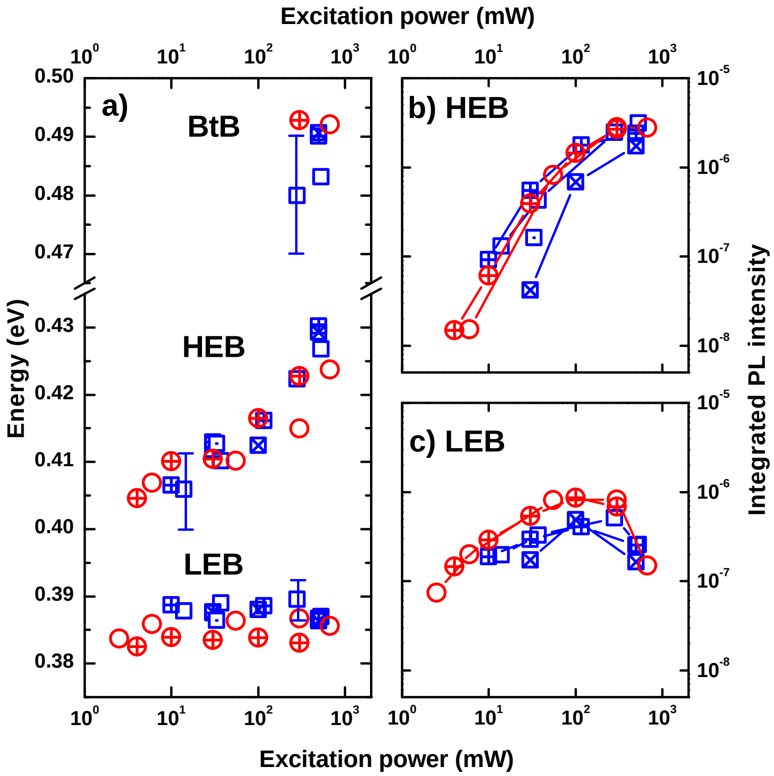

***Figure 4.11.:*** (a) PL peak energies of the low (LEB) and high (HEB) energy emission band as well as the peak attributed to the band-to-band emission (BtB) as a function of the excitation power for sample A (squares) and sample B (circles). Integrated PL intensities of the HEB (b) and the LEB (c) for both samples. For increasing excitation powers a saturation of the PL emission can be observed. Symbols with distinct fillings denote measurements on different positions on the same sample.

is attributed to the donor-acceptor pair overlapped with the band-to-acceptor recombinations, which are usually not well resolved. Although the precise identification of the shallow impurity cannot be determined, it is worth noting that carbon is often observed as an impurity in samples grown by chemical beam epitaxy [159].

The HEB peak position blue-shifts approximately 15–30 meV as the average excitation power raises from 10 to 500 mW and becomes dominant [cf. Figs. 4.11(b) and (c)]. This large energy shift is a behavior

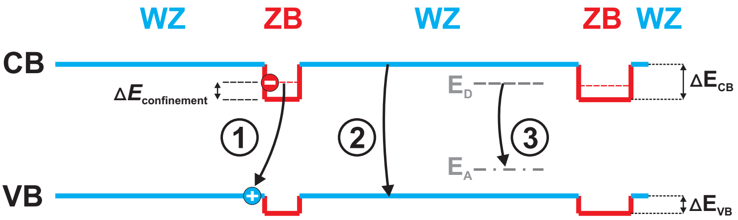

***Figure 4.12.:*** Schematic diagram of the valence band (VB) and the conduction band (CB) of the wurtzite InAs nanowires with zincblende sections. The numbering denotes possible transitions in the InAs nanowires; ① quantum well related recombination, ② band-to-band transition in wurtzite phase and ③ donor-acceptor recombination.

usually observed in quantum wells with type-II band alignment which is attributed to the band bending induced by the carrier accumulation at the interfaces and the band filling effect. Similar blue-shifts have been observed in InP [160, 161] and GaAs [51] nanowires containing wurtzite and zincblende phases, where type-II interfaces between these structures were present. In fact, TEM images of the InAs nanowires show some zincblende stripes in the predominant wurtzite structure along the wire axis forming a quantum well potential profile as depicted in the schematic diagram in Fig. 4.12. It has been predicted theoretically that InAs zincblende/wurtzite superlattices have a type-II band alignment [47, 162, 163] which have a crucial effect on the optical properties of the nanowires [161]. Photoexcited electrons and holes get spatially separated in the zincblende and wurtzite section, respectively. At low excitation powers, these electrons recombine with the holes leading to an emission below both, the zincblende and wurtzite, band gap energies. However, if the carriers are confined within the quantum wells in the zincblende structure, the minimum possible recombination energy corresponds to a transition from the confined ground state in the zincblende conduction band to the top of the wurtzite valence band (transition ① in Fig. 4.12). When the excitation power is increased, state filling of electrons in the zincblende section and band bending result in a blue-shift and broadening of the HEB [see Fig. 4.10(a)]. Thus, the HEB is attributed to the quantum well related emission.

Another effect that may be present in nanowires is the radial confinement. In our case, most of the nanowires have a diameter much larger than the effective Bohr radius such that the radial quantum confinement is negligible. To support this assumption the energy gap between the quantized ground states of the conduction and valence band for an infinite long cylinder according to an overly simplified effective mass model [18, 164] is calculated where the band gap is given by

$$E = E_{\mathrm{g}} + (2\hbar^2\xi^2/d^2)(1/m_e + 1/m_h) \tag{4.3}$$

and $E_{\mathrm{g}}$ is the bulk band gap, $\xi$ the zero-point of the cylindrical Bessel function (2.4048), $d$ the diameter of the nanowires and $m_e = 0.042$ and $m_h = 0.084$ [54] the effective electron and hole masses, respectively. The calculations reveal a band gap difference between nanowires with diameters of 70 nm and 50 nm of approximately 5 meV which is within the error of our measurements. The fraction of the nanowire extension that have diameters smaller than 50 nm located at the nanowire tip corresponds to less than 5% and can be neglected. Furthermore, photoexcited carriers at the tip will most likely diffuse to wurtzite band edges with lower potential in thicker nanowire sections where they will recombine.

Figures 4.13(a) and (b) presents the temperature dependent PL spectra measured for a fixed intermediate excitation power (50 mW) for sample A and sample B, respectively. Under these conditions the LEB is still dominant at low temperature. When the temperature is increased, the LEB decreases rapidly and the HEB becomes dominant, in agreement with the assignation of the peaks to the donor-acceptor pair/band-to-acceptor transition and the excitonic quantum well related recombination. Similar effects have also been observed for bulk InAs [158] and GaAs nanowires [165].

Figures 4.13(c) and (d) display the PL spectra for different excitation powers measured at 100 K for sample A and sample B, respectively. The corresponding PL peak energies for the HEB as a function of temperature for a fixed intermediate excitation power (50 mW) and as a function of different excitation powers measured at 100 K are depicted in Figs. 4.14(a) and (b) for sample A (squares) and sample B (circles), respectively.

A clear blue-shift with increasing temperature is observed. This behavior, which is opposite to the usual reduction of the band gap of semiconductors with increasing temperature [155, 166], may be attributed to the thermal excitation of the confined electrons to higher energy states

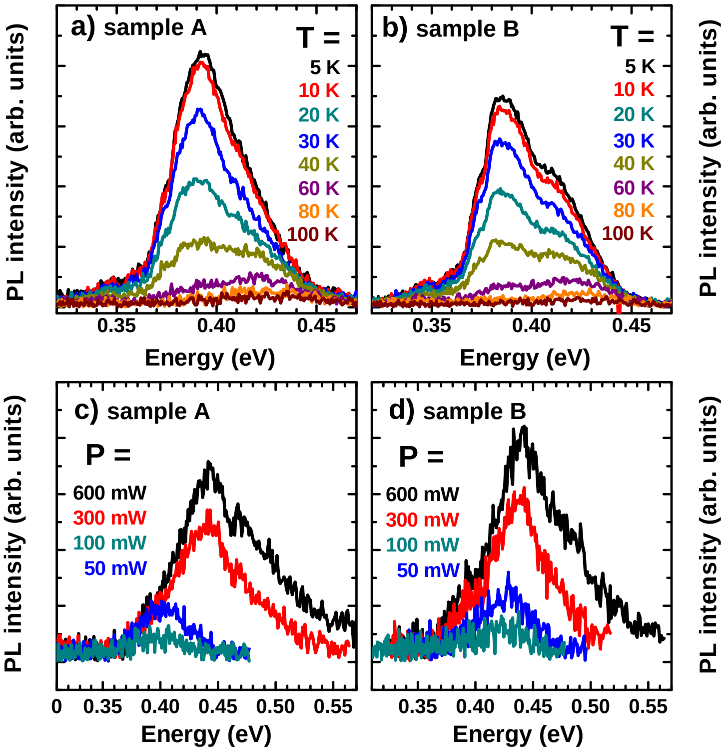

*Figure 4.13.:* PL spectra from sample A (a) and sample B (b) measured at different temperatures. PL spectra from sample A (c) and sample B (d) measured at 100 K for different excitation powers.

in the zincblende phase. In addition, rising the excitation power at 100 K [see Figs. 4.13(c) and (d) and 4.14(b)] further blue-shifts the emission band. This behavior is associated to the band filling of the zincblende quantum well states due to the increased excitation power. This leads to a blue-shift of the emission towards the band gap energy of the wurtzite structure (transition ② in Fig. 4.12) which seems to saturate at high excitation power for both samples suggesting that the saturation energy is the band-to-band transition energy of the wurtzite InAs phase. For high excitation power, the emission energy is determined to be $0.447 \pm 0.010$ eV which is a lower bound for the fundamental band gap of wurtzite InAs at 100 K. Note that due to the water absorption in the spectral range

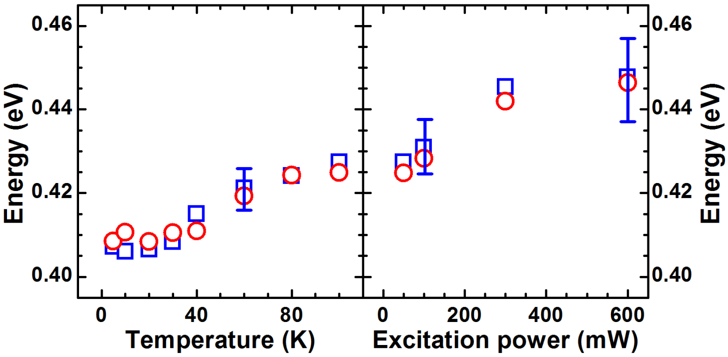

***Figure 4.14.:*** (a) PL peak energies of the HEB of sample A (squares) and sample B (circles) as a function of temperature. (b) PL peak energies at 100 K as a function of excitation power.

between 0.445 eV and 0.485 eV the data has been excluded in the fits leading to larger uncertainties in the determination of the blue-shifted emission energies [cf. error bars in Fig. 4.14(b)]. If it is assumed that the temperature dependence of the band gap of InAs is the same for the wurtzite (WZ) and zincblende (ZB) [156] phases, the lower bound for the wurtzite band gap at 5 K can be estimated as:

$$\begin{aligned} E_{\mathrm{g,5K}}^{\mathrm{WZ}} &= \left(E_{\mathrm{g,100K}}^{\mathrm{WZ}} - k_{\mathrm{B}}T/2\right) + (E_{\mathrm{g,5K}}^{\mathrm{ZB}} - E_{\mathrm{g,100K}}^{\mathrm{ZB}}) \\ &= 0.447\,\mathrm{eV} + 0.015\,\mathrm{eV} = 0.462\,\mathrm{eV} \end{aligned} \tag{4.4}$$

where the term $k_{\mathrm{B}}T/2$ accounts for the thermal excitation and $k_{\mathrm{B}}$ represents the Boltzmann constant. This value is 43 meV higher than that of the zincblende structure and is in good agreement with the available theoretical works which predict a 40 – 66 meV higher value for the wurtzite structure [47, 48, 54]. It is close to the value suggested by KOBLMÜLLER *et al.* [65] who recently observed a PL peak shoulder at 0.50 eV that they attributed to the band transition in the wurtzite segments of predominant zincblende InAs nanowires, and to the experimental values of 0.52 eV [60] and 0.54 eV [59] mentioned before. In addition, the lower bound value is only slightly lower than the observed BtB emission, shown in Figs. 4.10(a) and (b), that may be associated with the band-to-band transition with an average emission energy of 0.488 ± 0.010 eV for high excitation power at $T = 5\,\mathrm{K}$ [cf. Fig. 4.11(a)]. Although the BtB emission energy has been estimated with an elevated error due to the low intensity of the shoulder and the water absorption in the spectra, it corroborates the assignment of the lower threshold for the wurtzite InAs band gap at 5 K. Finally, our results are higher than the PL emission energies of 0.426 eV assigned to the band gap energy with small confinement effect by by Sun *et al.* [155]. These authors have also observed an emission at $0.43 - 0.45$ eV that has been attributed to surface-related effects. Although the pinning of the Fermi level at the surface, which leads to an electron accumulation layer close to the surface, should be present in the nanowires of this work, this is not likely to be the origin for the high emission energy detected for the HEB since the large blue-shift observed for increasing excitation power and increasing temperature cannot be explained by that. These features are rather more consistent with the type-II band alignment of wurtzite and zincblende phases. Furthermore, broad values of the band gap of wurtzite InAs obtained by several groups indicate that distinct effects, such as excess of carriers, lateral confinement, polytypism, surface effects and the substrate may affect the band gap measurements of InAs nanowire ensembles. Due to the low optical efficiency of infrared photodetectors in this spectral range the signal-to-noise may be too low in order to measure individual nanowires to address this point.

## 4.3. Summary

In this chapter, the Raman scattering results on a single wurtzite InAs nanowire and the PL results on wurtzite InAs nanowire ensembles have been presented. Resonant Raman scattering measurements have been performed to determine the $E_1^{\mathrm{G}}$ transition energy of the wurtzite structure to be approximately 100 meV lower than the one in the zincblende phase supported by an ab initio calculation of the electronic band structure for wurtzite and zinc-blende structure from Luis C. O. Dacal. Additional polarized Raman scattering experiments reveal the highest Raman intensity for the TO mode in $x(y,y)\bar{x}$ configuration, where the incident and scattered polarizations are parallel to each other and perpendicular to the nanowire axis. From the polarization dependence, the optical $\mathrm{A_1(TO)}$ and $\mathrm{E_2^H}$ phonon modes of the wurtzite structure could be identified which agrees well with the wurtzite phonon modes calculated by an extended

11-parameter rigid-ion-model from J. R. Madureira. An $E_1$(TO) phonon could not be resolved. A shoulder, detected at the low frequency side of the LO phonon mode, has been assigned to the SO phonon mode which appears only in $x(y,y)\bar{x}$ configuration.

The obtained PL spectra have revealed two main optical emission bands attributed to the donor-acceptor pair transition and to the recombination of carriers in quantum well structures formed by alternating wurtzite and zincblende sections along the nanowire axis. A large blue-shift of the latter, observed when the excitation power is increased, is consistent with a type-II band alignment between the wurtzite and zincblende phases predicted by theoretical works. Additional temperature dependent PL measurements have shown a blue-shift in contrast to the usual reduction of the band gap of semiconductors with increasing temperature. A successive increase of excitation power have revealed a further blue-shift of this band which is attributed to the appearance of the band-to-band transition. From these results, a lower bound for the wurtzite InAs band gap has been estimated to 0.458 eV in agreement with previous works.

In conclusion, these results shed light on the electronic, structural and optical properties of the wurtzite phase in InAs nanowires. The characterization of nanowires is fundamental for the determination of their physical properties and for the application in optoelectronic devices. In the recent years, a lot of work has been published about the physical properties of the wurtzite and zincblende phase in III-V semiconductor nanowires, but still there is much work left to be done in order to get a clear picture of the nanowire properties.

# 5. Acoustic charge transport in single nanowires

The previous chapter has been primarily concerned with the fundamental characterization of the electronic, structural and optical properties of wurtzite InAs nanowires. The following focuses on the application of nanowires and their suitability for the application in optoelectronic devices. For this, GaAs nanowires and (In,Ga)As/GaAs nanowires are considered since their optical emission energies lie in the near-infrared region between 800 nm and 930 nm, where optical detection is much more efficient than in the mid-infrared; a region where InAs exhibits PL due to its narrow band gap.

This chapter presents the manipulation of photoexcited carriers by surface acoustic waves (SAWs). It has been reported that carriers can be controlled in systems placed on a piezoelectric substrate. This approach has been shown in quantum well structures where single electrons [167, 168] as well as electron spins [169–171] have been transported by SAWs. In addition, SAWs have been used to transfer electrically injected carriers in carbon nanotubes [172–174] and GaN nanowires [175]. More recently, the controlled modulation of the PL from individual GaAs nanowires by SAWs has been shown [176]. In this chapter, the obtained results demonstrate the possibility of acoustic transport of photoexcited charge carriers along the axis of single GaAs (sample D) and (In,Ga)As/GaAs (sample E) nanowires to a second location where they recombine under emission of sub-nanosecond light pulses synchronized with the SAW phase. Furthermore, the generation and transport of spins in the nanowire are investigated. The contactless control of the ambipolar transport over micrometer distances and the emission of very short light pulses opens a wide range of nanowire applications in optoelectronic devices. To demonstrate their potential, the realization of a high-frequency source of anti-bunched photons based on the acoustic transport is presented in Ch. 6.

In the first section, the PL results of a single GaAs nanowire, which allows to characterize the investigated nanowire, are presented. In the following, the acoustic transport from photoexcited carriers at one extreme of the nanowire to a remote position is demostrated and the recombination of the carriers along the wire is investigated. Time-resolved PL (TRPL) measurements shed light on the transport process which can be explained by a simple model in agreement with simulations on the acoustic transport. Polarized PL results suggest that transported electrons become trapped in zincblende sections in the nanowire where they recombine and spin-polarized measurements show that electron spins cannot be generated and transported along the nanowire axis. Then, the results of the PL and acoustic transport measurements of an (In,Ga)As/GaAs nanowire are presented and compared with the ones of the GaAs nanowire. In the final section, the results are summarized.

## 5.1. Photoluminescence of single GaAs nanowires

In this section, the GaAs nanowire used for the acoustic transport measurements (see next section) is characterized by PL spectroscopy to get a clear picture of the optical emission from the nanowire since the transport of carriers is demonstrated by detecting the recombination of the transferred electrons and holes. For this, the nanowire has been illuminated using a expanded laser spot, that covers the whole nanowire (see left inset in Fig. 3.13), and the PL was recorded with spatial and spectral resolution providing information about the different emission centers along the nanowire axis.

The PL measurements on single GaAs nanowires were performed with the basic setup described in Fig. 3.13 at low temperature ($T = 20\,\mathrm{K}$). In Fig. 5.1(a), the PL image of a nanowire is displayed. The image shows the spectral (horizontal scale) PL distribution along the nanowire axis (vertical scale) which has a length of approximately 8 µm. The PL is dominated by several emission centers along the nanowire that are most likely induced by defects, impurities and band gap modulations due to stacking faults or wurtzite/zincblende boundaries which are described in more detail in Sec. 5.4. When a SAW is applied, the PL intensity

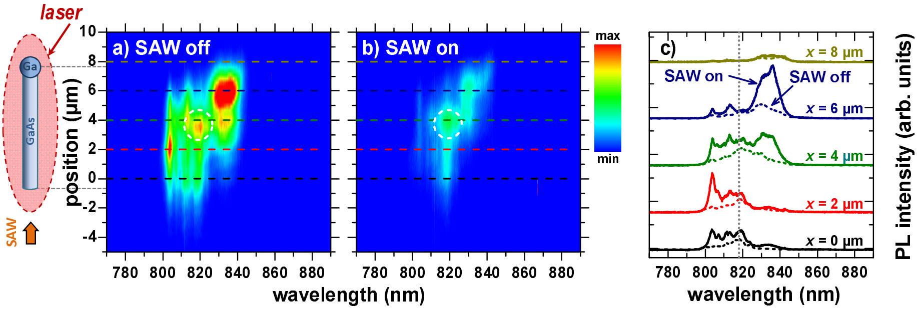

***Figure 5.1.:*** PL images of a single GaAs nanowire illuminated by a expanded laser spot (cf. inset on the left) in the absence (a) and presence (b) of acoustic power. (c) PL spectra integrated around the positions $x = 0, 2, 4, 6$ and $8\,\mu\text{m}$, indicated by the dashed lines in (a) and (b). The dotted line and the dashed circles denote the region where transported carriers recombine (see Sec. 5.2).

is reduced in the whole spectral range [cf. Fig. 5.1(b)]. The reduction is due to the induced spatial separation of electrons and holes by the SAW piezoelectric field, which decreases the radiative recombination probability, as described in Sec. 3.2.3 before. The integrated PL spectra in the absence (solid lines) and the presence (dashed lines) of a SAW ($P_{\text{rf}} = 11\,\text{dBm}$) at the positions $x = 0, 2, 4, 6$ and $8\,\mu\text{m}$, indicated by the dashed lines in (a) and (b), are plotted in Fig. 5.1(c). The reduction of the PL is not uniform across the nanowire. This indicates that the different emission centers have distinct ionization energies. This can be observed, for example, for the region indicated by dashed circles in (a) and (b) and the dotted line in (c). Here, the SAW modulation of the band structure cannot ionize all $e-h$ pairs such that the reduction of the PL signal is relatively small. However, when the acoustic power is further increased almost all radiative recombination centers become quenched due to the efficient carrier separation by the SAW piezoelectric field and mostly nonradiative recombinations take place, as can be observed in Fig. C.2 in the Appendix C where the evolution of the PL for different acoustic powers is shown.

## 5.2. Acoustic charge transport

The acoustic charge transport was studied on the same single GaAs nanowire characterized previously. The nanowire was incidentally aligned with the SAW propagation direction and it was used the same basic setup as in the previous section. In contrast to the expanded laser spot used for the characterization of the nanowire emission centers, the excitation laser was focused tightly (laser spot diameter approximately 1.5 μm) on the bottom end of the nanowire (with respect to the growth direction) in order to photoexcite carriers in a small defined region. The IDT facing this end of the nanowire was used as acoustic power source. In Figs. 5.2(a-i), the PL images of the nanowire for increasing acoustic amplitudes (specified in terms of the nominal rf power $P_{\mathrm{rf}}$ applied to the IDT) are recorded. Without acoustic power, the PL emission is restricted to the region of the excitation laser spot (position G) at $x = 0$ (cf. left inset) and is enlarged due to the diffusion of the photoexcited carriers along the nanowire. When the acoustic amplitude increases, the PL intensity at G

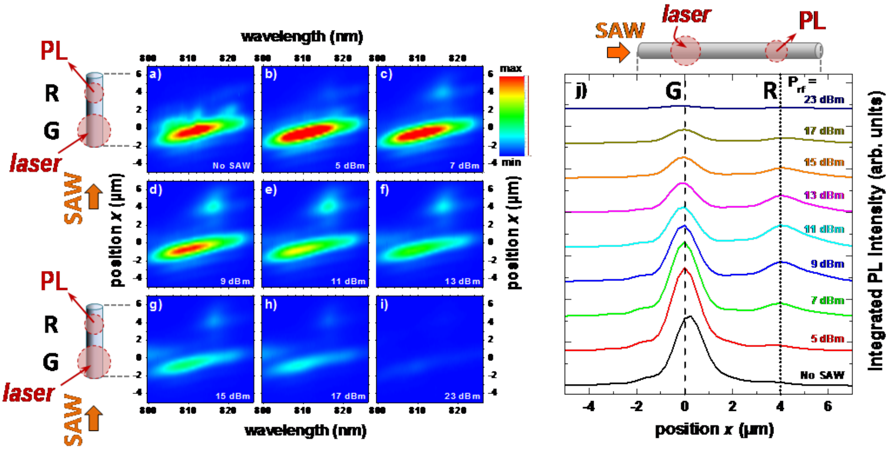

***Figure 5.2.:*** (a-i) PL images of a GaAs nanowire excited by a tightly focused laser beam close to the bottom end of the nanowire (cf. left inset) for different acoustic amplitudes. Acoustic charge transport can be observed for moderate acoustic powers. (j) PL profiles along the nanowire axis integrated from 813.9 nm to 819.1 nm for different acoustic amplitudes at a fixed rf frequency of 226.5 MHz.

reduces and a second emission at a remote position (R) appears a few µm away from G along the SAW propagation direction. This is demonstrated in Fig. 5.2(j) where the PL profiles integrated from 813.9 nm to 819.1 nm for different acoustic amplitudes are depicted. As already mentioned in the last section, the reduction of the emission at G is due to the induced spatial separation of the charge carriers by the SAW piezoelectric field. The emission at R is attributed to the transport of the photoexcited electrons and holes along the nanowire axis and their recombination close to the remote position. For high acoustic amplitudes, the PL intensity is diminished along the whole nanowire as already observed in the last section. The highest transport efficiency is obtained with an acoustic amplitude of 11 dBm for the trap emitting at 816 nm and not, for example, for the emission with highest intensity at 835 nm observed in Fig. 5.1 for homogeneous illumination. This behavior may be due to the fact that the transport efficiency to R is higher since the emission region at R is closer to the illumination area at G.

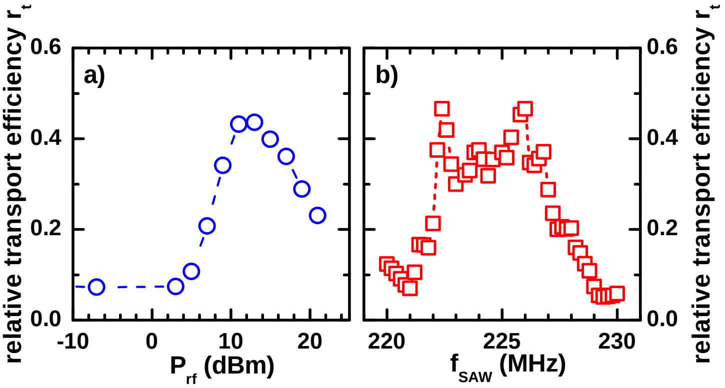

***Figure 5.3.:*** Relative transport efficiency $r_t$ as a function of the rf power $P_{rf}$ (a) applied to the IDTs for a fixed rf frequency of 226.5 MHz and as a function of the rf frequency $f_{SAW}$ (b) for a fixed rf power of 11 dBm.

In order to demonstrate that the transport is caused by the SAW, the relative transport efficiency – defined by

$$r_t = \frac{I_{PL}(R)}{I_{PL}(G) + I_{PL}(R)} \tag{5.1}$$

where $I_{PL}(G)$ and $I_{PL}(R)$ are the PL intensities emitted at the positions G and R – is plotted as a function of the applied acoustic amplitude for a fixed rf frequency of 226.5 MHz and as a function of the rf frequency for a fixed acoustic amplitude of 11 dBm in Figs. 5.3(a) and (b), respectively. From Fig. 5.3(a), it can be observed that the transport occurs at approximately 3 dBm. In addition, transport is only observed for rf frequencies close to approximately 225 MHz which corresponds to the acoustic emission band of the used IDTs at 20 K (cf. Fig. 3.15). Outside this range, the low $r_\mathrm{t}$ values are attributed to carrier diffusion to the remote position.

## 5.3. Time-resolved photoluminescence

After having shown that carriers can be transferred by SAWs along the nanowire in the previous section, the dynamics of this process will be addressed in the following. For this, the same single GaAs nanowire as in the previous sections was investigated with the setup–option A displayed in Fig. 3.13. Short laser pulses (pulse width $\ll T_\mathrm{SAW}$) were used to photoexcite carriers at G and the evolution of the carrier recombination along the nanowire was recorded by a gated CCD camera with a gate time of 500 ps. The piezoelectric potential along the nanowire can be expressed as a function of the position $x$ and time $t$ – measured relative to the arrival time of the laser pulse – by

$$\Phi_\mathrm{SAW}(x,t) = \Phi_\mathrm{SAW,0} \cdot \sin\left[\frac{2\pi}{\lambda_\mathrm{SAW}}x - \frac{2\pi}{T_\mathrm{SAW}}(t+\tau)\right], \tag{5.2}$$

where $\Phi_\mathrm{SAW,0}$ is the potential amplitude. The laser pulse and the SAW were syntonized so that the carriers are photoexcited at G with a well-defined SAW phase specified by $\tau$. For this purpose, the frequency of the rf signal driving the SAW was divided by a factor of 8 and used to trigger the laser. This has been done in order to reduce the high SAW frequency to values that are appropriate for triggering the laser, leading to one laser pulse every eight SAW cycles. To generate carriers with different SAW phases ($2\pi\tau/T_\mathrm{SAW}$) at $t = 0$, the trigger pulse was electrically delayed with respect to the SAW by $\tau$. In the Figs. 5.5 the spatio-temporal PL integrated from 813.4 nm to 819 nm (cf. Fig. 5.2) for a fixed acoustic power of $P_\mathrm{rf} = 11$ dBm and for different values of the SAW phase delay $\tau$ is displayed. At $t = 0$ the laser pulse generates $e-h$ pairs at G which

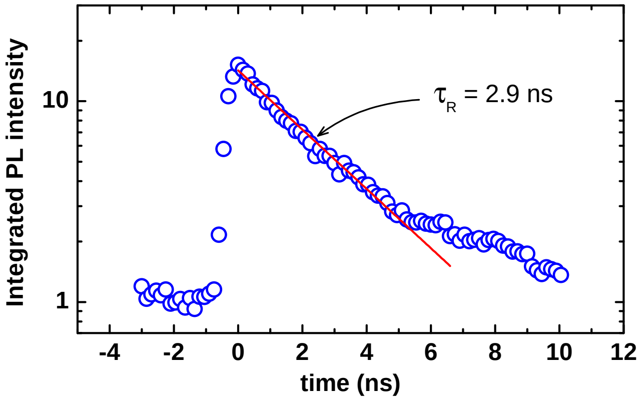

***Figure 5.4.:*** Time decay of PL from the single GaAs nanowire excited by a tightly focused laser beam at one edge of the nanowire.

are transferred by the SAW to the position R where they recombine (as observed before in the last section). The time-resolved plots show an intense PL at the generation site G over more than a half-cycle of the SAW and short recombination pulses at R which are comparable to the time resolution of the gated camera and repeat every half cycle ($T_{\mathrm{SAW}}/2$). The corresponding integrated time-resolved PL profiles at R are plotted in Fig. 5.6(a). The recombination pulses at R are due to the oscillatory motion of the electrons and holes due to the periodic SAW piezoelectric potential and can be observed for time delays exceeding $T_{\mathrm{SAW}}$ (approximately 4.4 ns) which is longer than the PL decay time measured to be approximately $\tau_{\mathrm{R}} = 3\,\mathrm{ns}$ in the absence of acoustic power (see Fig. 5.4).

In order to reproduce the PL dynamics, the acoustic transport in the nanowire was simulated by solving the one-dimensional drift/diffusion equations for the electron ($n$) and hole ($p$) concentrations under the influence of the SAW field as described in the Appendix B. The simulations performed by Alberto García-Cristóbal assume a potential $\Phi(x,t)$ along the nanowire that takes into account two contributions: the SAW piezoelectric potential $\Phi_{\mathrm{SAW}}(x,t)$ along the nanowire given by Eq. 5.2 and a potential well $\Phi_{\mathrm{d}}(x)$ at the remote position R ($x = 4$) which accounts for a trap that capture both electrons and holes. $\Phi(x,t)$ is illustrated along the nanowire in the case of holes for different $\tau/T_{\mathrm{SAW}}$ ratios in Fig. 5.6(b).

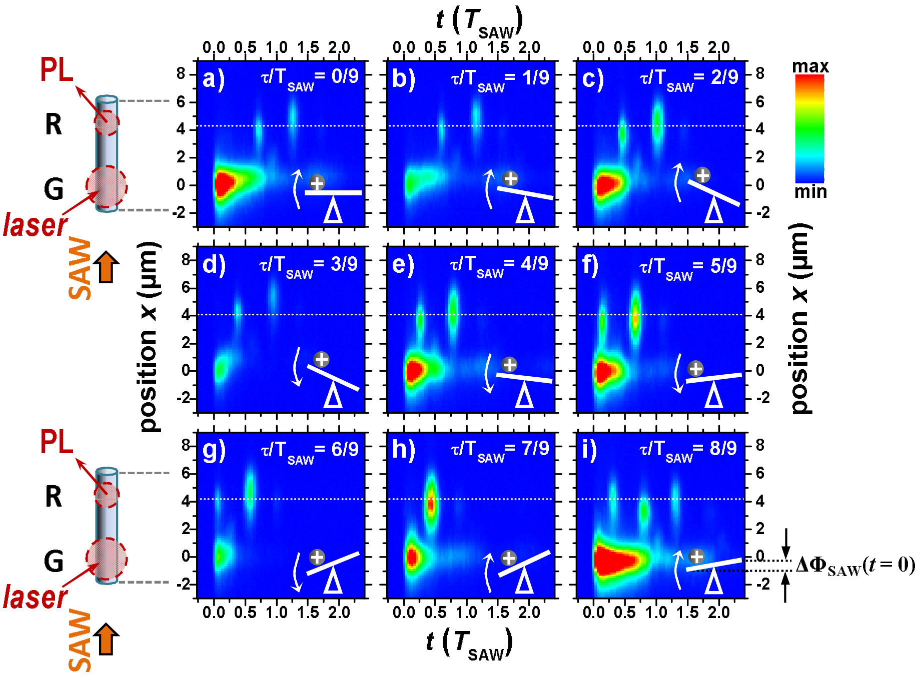

***Figure 5.5.:*** Spatio-temporal PL integrated in the wavelength range from 813.4 nm to 819 nm. On the vertical axis the position $x$ along the nanowire axis and on the horizontal scale the time delay $t$ with respect to the arrival time of the excitation laser pulse are presented. (a-i) The plots were recorded for different SAW phases $\tau/T$. The hole motion is simply modeled by the slide of a ball on a seesaw whose tilt angle oscillates at the SAW frequency as illustrated in the insets. The piezoelectric potential difference $\Delta\Phi_{\mathrm{SAW}}$ at $t = 0$ between G and R is proportional to the height difference between the left and right seesaw ends and the arrows exhibit the direction of motion of the seesaw. The SAW power was fixed for all measurements at $P_{\mathrm{rf}} = 11\,\mathrm{dBm}$.

The holes move periodically according to the gradient of the potential and can be trapped at R. Recombination at R takes place when electrons are subsequently transferred to the trapped holes. Similar considerations are valid for the electrons moving always in opposite direction with respect to the holes. This leads to a motion of holes towards R in one half cycle of the SAW and the transport of electrons to the remote position in the other SAW half cycle. Under these conditions, the remote PL dynamics is governed by the acoustic transport of both electrons and holes along

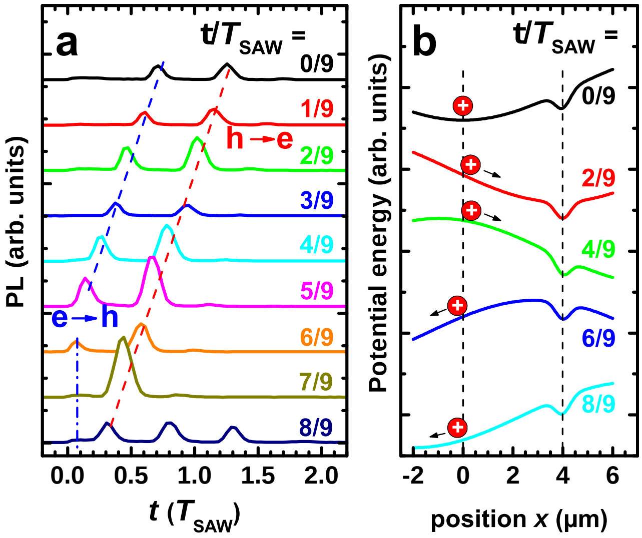

***Figure 5.6.:*** (a) Time-resolved PL profiles integrated at R, indicated by the dotted lines in Fig. 5.5, for different $\tau/T_{\mathrm{SAW}}$ ratios. (b) Potential profiles of the holes $\Phi_{\mathrm{p}}(x, t = 0)$ at the arrival time of the laser pulse used in the simulations. The potential is given for different SAW phases as a function of the nanowire position (length approximately 8 µm). The minimum at $x = 4$ µm is due to the introduced potential well modeling the trap at R. The arrows indicate the direction of the hole motion at $t = 0$.

the nanowire as this potential oscillates with the SAW frequency. These experimental features can essentially be reproduced with the simulations which are presented in Appendix B.

For a straightforward picture of the carrier dynamics, which is consistent with the obtained results, a linear potential variation between G and R is assumed. This is justified by the fact that the distance between G and R ($\sim 4$ µm) is shorter than $\lambda_{\mathrm{SAW}}/4$ [cf. Fig. 5.6(b)]. Under these conditions the hole motion becomes analogous to the slide of a ball on an oscillating seesaw whose difference of end-point heights is proportional to the potential difference $\Delta\Phi_{\mathrm{SAW}}(t) = \Phi_{\mathrm{SAW}}(x = 0, t) - \Phi_{\mathrm{SAW}}(x = 4, t)$, as indicated in the inset of Fig. 5.5(i). The schematic diagrams show the angular position and direction of motion of the seesaw at the arrival time of the laser pulse ($t = 0$). For electrons the motion is directed opposite to the holes, i.e. to the locations of higher potential. In order to observe the recombination pulses at R, transferred carriers need to be trapped in

R until carriers with opposite polarity arrive in a subsequent half-cycle of the SAW. This suspends the spatial separation of the electrons and holes and increases the recombination rate. For $0 < \tau/T_{\mathrm{SAW}} \leq 4/9$, $\Delta\Phi_{\mathrm{SAW}}(t)$ [Figs. 5.5(a-e)] is positive which leads to the motion of holes towards R where they become trapped. After one SAW half-cycle, $\Delta\Phi_{\mathrm{SAW}}(t)$ changes its sign and forces the electrons to move towards R where the first recombination pulse takes place [cf. blue dashed line denoted $e \rightarrow h$ in Fig. 5.6(a)]. Note that not all the photoexcited holes recombine with the electrons since a fraction of them are driven back to G when $\Delta\Phi_{\mathrm{SAW}}(t)$ changes its sign. The second pulse occurs in the following SAW half-cycle when these holes return to R and recombine with electrons that have remained in the trap (red dashed line denoted $h \rightarrow e$). Depending on the excitation conditions, this process can repeat various times leading to additional PL pulses. Interestingly, the second pulses are stronger than the former one ($e \rightarrow h$ pulses), a characteristic that will be discussed below.

For the case $5/9 \leq \tau/T_{\mathrm{SAW}} < 1$, the same approach can be used to qualitatively explain the occurring pulses at R, simply exchanging the role of the electron and the hole. This leads to a first pulse where the electrons, previous transferred and trapped in the first SAW half-cycle, recombine with the holes transported in the subsequent half-cycle of the SAW ($h \rightarrow e$ pulses). However, prior to the arrival of this $h \rightarrow e$ pulse, a further pulse at short time delays ($< 0.3\,\tau/T_{\mathrm{SAW}}$) can be observed. This cannot be attributed only to the carrier motion [vertical blue dashed-dotted line in Fig. 5.6(a)], but can be well-reproduced in the simulations assuming that prior to the arrival of the laser pulse holes are already present in the trap at R (see Appendix B). These holes do not originate from the photoexcitation during a previous laser pulse since, under the used excitation conditions, the remote PL vanishes within times much shorter than the laser repetition rate of 35.5 ns. They may be induced by the ionization of shallow acceptors in the nanowire and subsequent capture in the trap at R.

As mentioned before, the $h \rightarrow e$ pulses are stronger than the $e \rightarrow h$ pulses probably due to the more efficient transport and trapping of the electrons with respect to the holes. In addition, it can be observed in Figs. 5.5(a-i) that the $h \rightarrow e$ and $e \rightarrow h$ pulses appear at slightly different positions on the nanowire. These pulses are, moreover, slightly

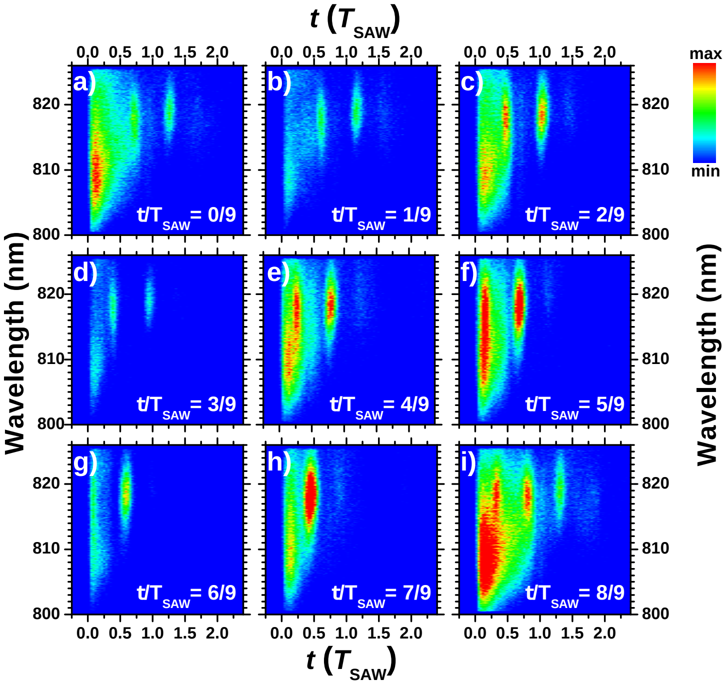

***Figure 5.7.:*** Spectro-temporal PL integrated along the nanowire extension. On the vertical axis the wavelength range and on the horizontal scale the time delay $t$ with respect to the arrival time of the excitation laser pulse are presented. (a-i) The plots were recorded for different SAW phases $\tau/T$. The SAW power was fixed for all measurements at $P_{\mathrm{rf}} = 11\,\mathrm{dBm}$.

shifted in energy, as can be seen in Fig. 5.7 where the spectro-temporal PL integrated along the nanowire extension is shown (analogous to Fig. 5.5 where the PL has been integrated over a spectral range).

A possible explanation for the latter is the modulation of the transition energies induced by the strain field that introduces a band gap variation in the regions of maximum tension and compression as illustrated in Fig. 5.8(a) and (b). The local variations in volume and symmetry of the crystal lattice [Fig. 5.8(a)] induces a strain field that accompanies the piezoelectric field leading to band gap values between $E_{\mathrm{g}}^{\mathrm{max}}$ and $E_{\mathrm{g}}^{\mathrm{min}}$ [Fig. 5.8(b)]. Such a splitting of the band gap has been reported for quantum well structures [178] and quantum dots [179]. This could

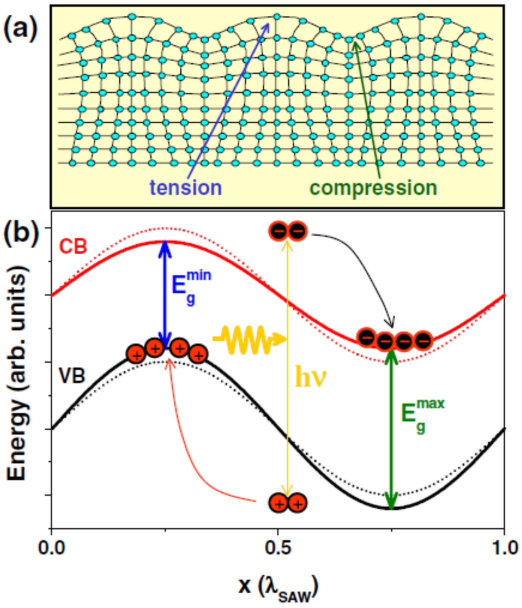

***Figure 5.8:*** (a) Strain field and (b) modulation of the conduction band (CB) and valence band (VB) edges of a semiconductor crystal by a surface acoustic wave. The piezoelectric potential associated with the strain introduces a type-II modulation of the band edges. The regions of compression and tension induced by the strain superimposes a small modulation of the band gap ($E_g$) with maximum and minimum values given by $E_g^{max}$ and $E_g^{min}$, respectively. The diagram in (b) also illustrates the spatial separation of photogenerated carriers by the piezoelectric field (taken from [177]).

explain the different emission energies of the detected PL pulses, but not the distinct positions of the emission on the nanowire. However, an effect of this band gap modulation on these measurements cannot be ruled out and more investigation is needed to clarify this fact. Additional experiments, for example, measuring the emission energies of the pulses as a function of the acoustic amplitude could shed light on this point since an increasing amplitude leads to a higher strain and, thus, to a larger splitting of the band gap values $E_g^{max}$ and $E_g^{min}$.

Another possibility is the recombination from nanowire sections that have different crystal structure. Due to the type-II band alignment [47, 51, 53, 56, 163, 180, 181] of the wurtzite and zincblende phases in GaAs, electrons will diffuse into zincblende sections while holes gets located in the wurtzite section (similar to the case of InAs discussed in Sec. 4.2). This can explain the different position and energy of the observed recombination pulses since recombination pulses happen at distinct crystal sections and their energy depends on the grade of quantum confinement of every section.

In the next section where the polarization characteristics of the emission is investigated, this explanation is discussed in more detail.

## 5.4. Linear polarized emission of the transported carriers

For a more detailed understanding of the recombination processes in the nanowire, polarized PL measurements were carried out. This can shed light on the crystal structure of the nanowires since the polarization of the emitted PL pulses depends on the crystal structure, as described in Sec. 3.2.2. The following results have been obtained from single GaAs nanowires that are different from the one investigated in the previous sections. For these experiments the basic setup was used in combination with option B and a liquid crystal retarder inserted to change the linear polarization of the incident laser beam (see Fig. 3.13). The measurements were performed in the same manner as in the former sections for the acoustic carrier transport where the incident laser beam was tightly focused at one edge of the nanowire. In order to study the emission characteristics of the nanowire, the PL images, which are the summation of the images recorded for the incident laser beam polarized perpendicular and parallel to the wire axis, are displayed in the absence and presence of a SAW in the Figs. 5.9(a) and (b), respectively. In the upper and lower part of the images, the spectrally (horizontal scale) and spatially (vertical scale) resolved nanowire emission polarized parallel and perpendicular to the nanowire axis are represented, respectively. The corresponding spatial PL profiles integrated from 796.6 nm to 823.3 nm are depicted in Figs. 5.9(c) and (d). Without acoustic power [Figs. 5.9(a)], the emission is restricted to the region close to the excitation spot (position G in the diagrams on the left of Figs. 5.9) and is enlarged due to diffusion processes along the nanowire. When a SAW is applied, the PL intensity at G reduces and a second emission at a remote emission (position R) appears a few µm away from G along the SAW propagation direction. These observations are consistent with the ones obtained in the previous sections [cf. Fig. 5.2(a)].

Additional information can be obtained considering the polarization of the PL emission which can deliver insight into the crystallographic structure of the nanowire. Without acoustic power, the broad emission

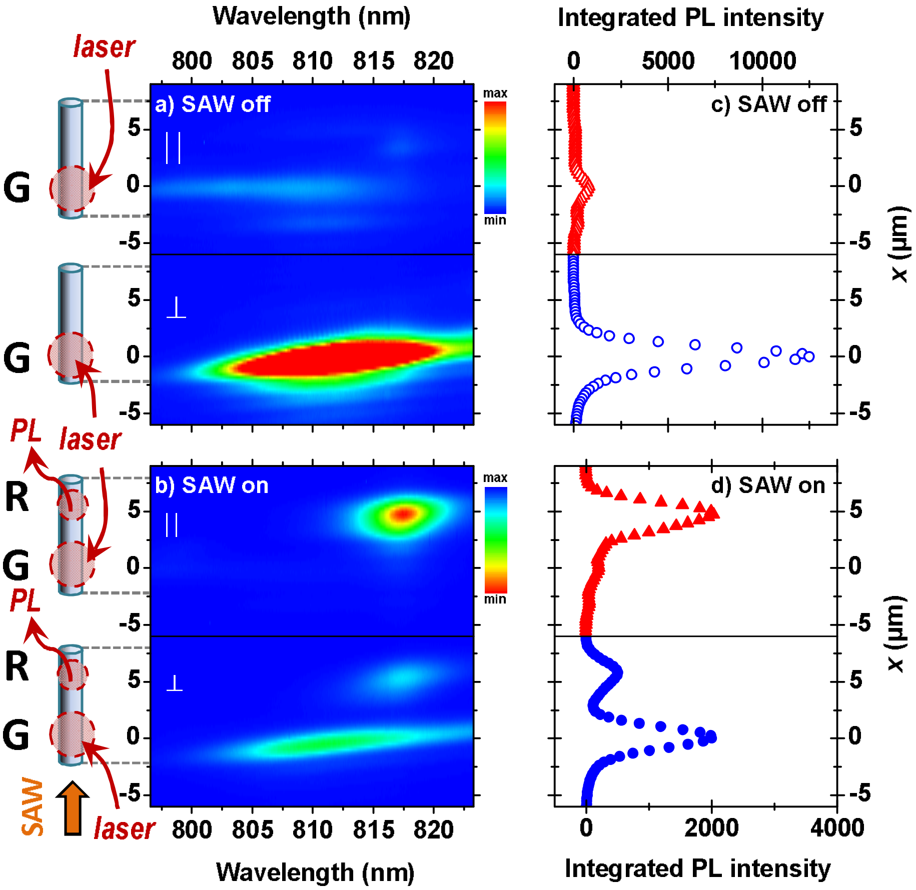

***Figure 5.9.:*** Polarized PL with spatial resolution excited by a tightly focused laser beam recorded in the absence (a) and presence (b) of acoustic power. Each figure is the summation of the PL images recorded for the incident laser beam polarized perpendicular and parallel to the wire axis. ∥ and ⊥ represent the polarized emission with respect to the wire axis. On the right, their corresponding spatial PL intensities integrated from 796.6 nm to 823.3 nm in the absence (c) and presence (d) of a SAW are displayed.

band at G is highly polarized perpendicular to the nanowire axis [see Figs. 5.2(a) and (c)]. When a SAW is applied, the emission at G maintains its polarization behavior while the recombination at R is polarized parallel to the nanowire axis [see Figs. 5.2(b) and (d)]. The emission at G is consistent with the optical selection rules expected for wurtzite GaAs nanowires [51] where the emission at the band edge is dipole allowed only if the electric dipole moment is perpendicular to the wurtzite c-axis (see Sec. 3.2.2). The emission at R, however, does not coincide with these selection rules. Since the recombination of the transported charge carriers take place at a remote position, the crystal structure of that region may be different. Indeed, the emission energy of approximately 818 nm – which is exactly the band gap energy of zincblende bulk GaAs [182] – suggests that recombination takes place in a zincblende region in the upper part of the nanowire, opposite to the acoustic transducer. This is supported by transmission electron microscopy measurements, which reveal a zincblende section in the top region of the nanowires, probably created during the cooling down after growth [183], as previously observed in CBE- and MBE-grown GaAs nanowires [88, 105]. The emission polarized parallel to the nanowire axis at R is consistent with the emission characteristics observed in zincblende GaAs nanowires [26, 184]. Here, the emission is preferentially polarized along the nanowire axis due to the dielectric mismatch between the nanowire and its surrounding (Sec. 3.2.2). The degree of linear polarization, $P = (I_\perp - I_\|)/(I_\perp + I_\|)$ – where $I_\perp$ and $I_\|$ are the PL polarization intensities detected perpendicular and parallel to the nanowire axis, respectively –, at the excitation spot G is approximately $+88\%$ (perpendicular) in the absence of a SAW, whereas at the remote position R the polarization becomes equal to approximately $-70\%$ (parallel) with acoustic power. Similar polarization results have been obtained for all probed nanowires.

In the following, the crystal structure of the nanowire as a possible explanation for the trapping of carriers is considered. The polarized PL results suggest that the trapping of carriers takes place in the zincblende sections of the nanowire. This is plausible for electrons since the band alignment between wurtzite and zincblende phases is type-II, as illustrated in Fig. 5.10(a). The zincblende section acts as a potential sink and traps the acoustically transferred electrons. When in a subsequent half cycle of the SAW the holes arrive, recombination of the $e - h$ pairs in the zincblende section take place ($h \rightarrow e$ pulses, cf. previous section).

This process, however, does not explain the trapping of holes since the zincblende valence band is energetically below the wurtzite valence band [Fig. 5.10(b)]. When photoexcited electrons are transported to R,

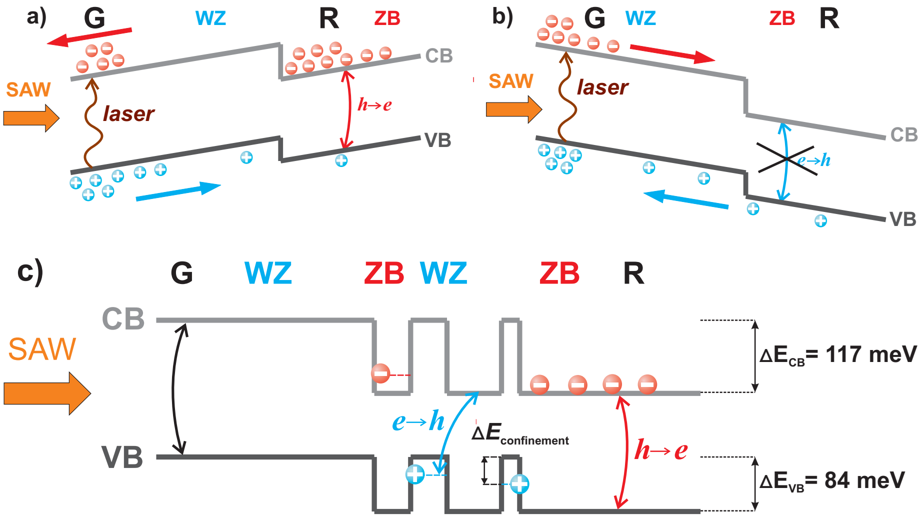

***Figure 5.10.:*** Schematic diagram of the valence band (VB) and the conduction band (CB) of a GaAs nanowire. When a SAW is applied the band edges gets modulated. The carrier motion for two selected SAW phases are presented. In (a), photoexcited holes are transferred to the zincblende section where they recombine with the trapped electrons. In (b), photoexcited electrons are transported to the zincblende section. Recombination gets suppressed since holes, that are previous transferred to R, are not trapped or return to G. (c) Band structure schematic for a GaAs nanowire with different wurtzite and zincblende sections. Thin sections give rise to confined states. Band offset values taken from Ref. [47].

they cannot recombine with holes, since the holes, that previously have been transferred to the zincblende section, could not be trapped or return to the generation point G. This can be explained by the fact that the detected recombination at R only consists of $h \rightarrow e$ pulses. Since the measurements are taken from single nanowires different from the one investigated in the last section, the nanowires most likely differ in their optical properties.

Furthermore, a distinct amount of defects or wurtzite/zincblende layer stacking can give rise to an altered trapping and emission behavior. As mentioned before, a zincblende section is formed at the top of the nanowire after the growth process. The change from wurtzite to zincblende crystal structure, most likely, produces a transition region with alternating wurtzite/zincblende sections close to the top of the nanowires. If such alternating sections between G and R are assumed, holes can be trapped in the wurtzite sections, located between two zincblende sections (stacking faults) as depicted in Fig. 5.10(c). The recombination from trapped holes in the wurtzite phase and electrons that are subsequently transferred can yield recombination pulses ($e \rightarrow h$) that can vary largely in their emission energies if quantum confinement effects in the alternating sections are considered. Due to the type-II band alignment between wurtzite and zincblende phases in GaAs, recombination pulses with energies of 1.5 eV (827 nm) and lower are possible in the absence of quantum confinement effects [47, 56, 180]. If the states are quantized, the emission energies can be higher than the band gap energies of the GaAs phases (e.g. for the zincblende structure the band gap is 1.516 eV/818 nm). This could explain the appearance of $e \rightarrow h$ pulses in the last section which are energetically close to the $h \rightarrow e$ pulses (cf. Fig. 5.7). In addition, the $e \rightarrow h$ pulses appear slightly shifted towards G with respect to the $h \rightarrow e$ ones (cf. Fig. 5.5). This is in agreement with the assumption that the $e \rightarrow h$ pulses come from the transition region with alternating phase sections located adjacent to R. Moreover, the different PL pulse intensities for $h \rightarrow e$ and $e \rightarrow h$ pulses (cf. Fig. 5.5) can be explained by this. Electrons become efficiently trapped in the large zincblende section at R, which lacks quantum confinement effects, and can recombine efficiently with subsequently transferred holes since the transition is vertical (high wave function overlap). In the case of holes, the trapping and transport are probably less efficient because of the lower band offset [cf. Fig. 5.10(c)], the quantized energy states – which diminishes the potential barrier – and the lower hole mobility. In addition, their recombination with transferred electrons, which occupy zincblende states due to the lower conduction band energies, is not vertical, thus, reducing the recombination probability of the $e \rightarrow h$ pulses.

If the GaAs nanowire investigated in this section is considered (Fig. 5.9), the defined PL at R suggests that the emission consists either of a combination of $e \rightarrow h$ and $h \rightarrow e$ pulses or of only one pulse type. The former is similar to the one observed for the nanowire in the previous section which has been discussed in the last paragraph. Since the recombination pulses have similar energies, they cannot be resolved spectrally. In addition, the low PL polarized perpendicular to the wire axis at R – related to the $e \rightarrow h$ pulses since the holes reside in a wurtzite section and selection rules apply which only allow the emission polarized perpendicular to the wire axis – is consistent with the lower PL pulse intensities observed for $e \rightarrow h$ pulses in the last section. The latter suggests that the $e \rightarrow h$ pulses at R are absent. Since the PL at R is mainly polarized parallel to the wire axis (Fig. 5.9), the recombination takes place in the zincblende section leading to $h \rightarrow e$ pulses. The absence of $e \rightarrow h$ pulses can be due to the lack of a transition region mentioned above. For nanowires with no or low amount of alternating wurtzite/zincblende sections, holes cannot be trapped sufficiently and the $e \rightarrow h$ pulse is avoided. Furthermore, in the case of alternating wurtzite/zincblende sections with low or no quantum confinement effects, holes may be sufficiently trapped, but their recombination probably leads to $e \rightarrow h$ pulses with energies beyond the detected wavelength range (796.6 – 823.3 nm) of these measurements.

Altogether, the obtained results suggest that the trapping of acoustically transferred holes and electrons takes place in different crystal sections along the nanowire leading to PL pulses at different emission energies and positions in the nanowire.

## 5.5. Spin polarization during charge transport

The results of the last section suggest that, due to the linear polarized emission characteristics, the nanowires cannot emit circularly polarized light. In the case of zincblende nanowires, this is because of the dielectric mismatch between the nanowire material and its surrounding – leading to emission polarized parallel to the wire axis – while for wurtzite wires the selection rules are the reason – suppressing the emission polarized parallel to the nanowire axis. To further support this conclusion, the acoustic transport of the electron spin along the nanowire has been investigated.

The transport experiments were carried out with the basic setup in combination with option B and C and an inserted liquid crystal retarder (see Fig. 3.13). Here, spin-up and spin-down electrons were generated on one end of the nanowire using right-handed ($\sigma^+$) and left-handed ($\sigma^-$) circularly polarized light, respectively. For simplicity, only the right-handed circularly polarized emission ($I_+$) is considered in the following.

For incident right-handed circularly polarized light ($\sigma^+$), the spatially resolved $I_+$ profiles in absence and presence of an acoustic power of

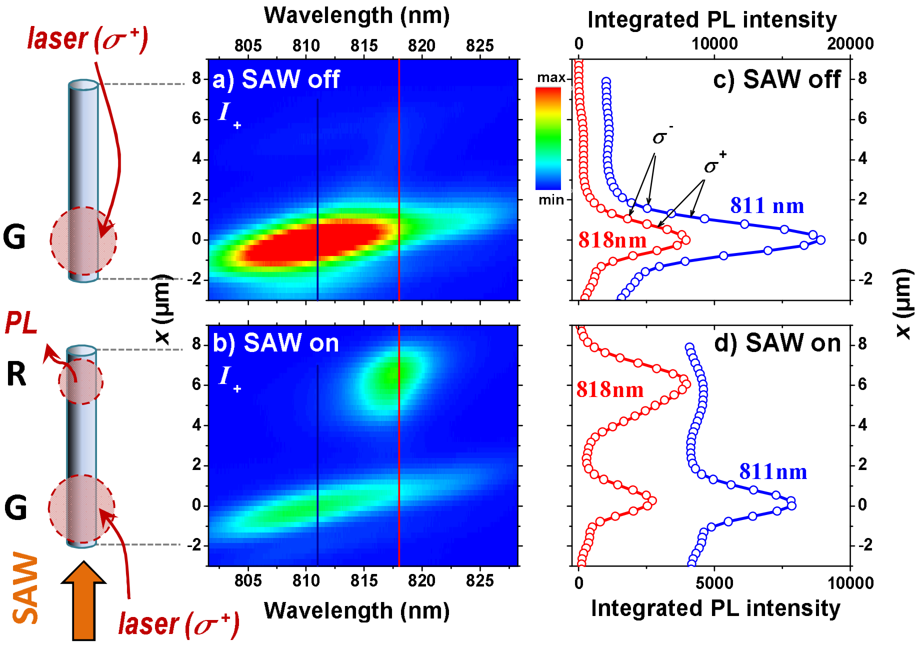

***Figure 5.11.:*** Spatially resolved right-handed circularly polarized PL emission ($I_+$) in the absence (a) and presence (b) of a SAW. The nanowire was excited by a tightly focused, right-handed circularly polarized laser beam ($\sigma^+$). On the right, the PL emission intensities ($I_+$) integrated from 806 nm to 816 nm (blue) and from 813 nm to 823 nm (red) in the absence (c) and presence (d) of an acoustic power of 12 dBm along the nanowire are shown. The solid line and the open circles represent the excitation with an incident laser beam that is right-handed ($\sigma^+$, solid line) and left-handed ($\sigma^-$, open circles) circularly polarized. Spectra were arbitrary shifted.

12 dBm are shown in Figs. 5.11(a) and (b), respectively. Figs. 5.11(c) and (d) present the $I_+$ profiles along the nanowire axis integrated around 811 nm (blue) and 818 nm (red), in the absence and presence of a SAW for $\sigma^+$ (lines) and $\sigma^-$ (circles). Without acoustic power the PL is emitted around 811 nm at the excitation spot G [Fig. 5.11(a)]. No significant difference of $I_+$ for $\sigma^+$ and $\sigma^-$ can be detected indicating that the spin polarization has been lost after excitation. The same picture can be observed when a SAW is applied. A remote spot appears emitting at 818 nm [Fig. 5.11(b)], exhibiting the charge transport as observed in the previous sections, but from Figs. 5.11(c) and (d) it can be seen that $I_+$ is

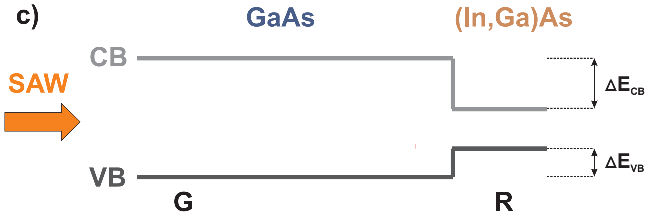

***Figure 5.12.:*** Schematic diagram of the valence band (VB) and the conduction band (CB) of a (In,Ga)As/GaAs nanowire. The type-I band alignment between GaAs and (In,Ga)As leads to a potential sink for electrons and holes.

the same for $\sigma^+$ and $\sigma^-$ excitations (cf. solid lines with open circles) at G and R.

Altogether, the results confirm that the nanowire emission is linear polarized leading to an evenly distributed emission for $\sigma^+$ and $\sigma^-$. Moreover, this suggests that no or only a very small excess of electrons with one spin state has been generated at G. Due to the polarization anisotropy of the absorption (see Sec. 3.2.2), it is very unlikely to excite one spin state with circularly polarized light since the dielectric mismatch between the nanowire and its surrounding strongly suppresses light polarized perpendicular to the nanowire. This is consistent with the observations at G where no difference between $\sigma^+$ and $\sigma^-$ – no matter if a SAW is applied or not – can be observed.

## 5.6. Photoluminescence and acoustic charge transport in single (In,Ga)As/GaAs nanowires

In this section, the results of the PL measurements and the acoustic transport in an (In,Ga)As/GaAs nanowire (sample E) are presented. In contrast to the GaAs nanowire, the (In,Ga)As/GaAs nanowire exhibits a quantum dot-like segment on the top of the nanowires which affects the physical properties of the nanowire. Due to the type-I band alignment between GaAs and (In,Ga)As [185, 186], the quantum dot-like segment acts as a potential sink for electrons and holes which favors the trapping of both electrons *and* holes in the (In,Ga)As sections due to the lower band

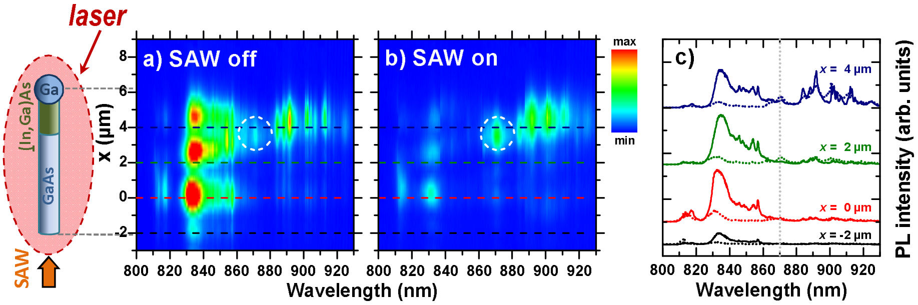

***Figure 5.13.:*** PL images of a single (In,Ga)As/GaAs nanowire illuminated by a expanded laser spot (cf. inset on the left) in the absence (a) and presence (b) of acoustic power. The dashed circles denote the region selected for the autocorrelation measurements. The acoustic wavelength and frequency of $\lambda_{\text{SAW}} = 11.67\,\mu\text{m}$ and $f_{\text{SAW}} = 338.4\,\text{MHz}$ have been used for acoustic excitation with $P_{\text{rf}} = 9\,\text{dBm}$. (c) Spectral lines integrated around the positions $x = 0, 2, 4, 6$ and $8\,\mu\text{m}$, indicated by the dashed lines in (a) and (b).

gap of (In,Ga)As (approximately 860 nm for an In content of $x = 0.05$ at 20 K [187]) compared to GaAs. The conduction band offset ($\Delta E_{\text{C}}$) in relation to the band gap difference ($\Delta E_{\text{g}} = E_{\text{g}}(\text{GaAs}) - E_{\text{g}}(\text{In}_x\text{Ga}_{1-x}\text{As})$) is reported to be in the range of 0.6 – 0.9 [185, 186, 188, 189, and references therein], i.e. the valence band offset is smaller than the conduction band offset (cf. Fig. 5.12).

Furthermore, it alters the PL emission compared with the emission from GaAs nanowires [cf. Fig. 5.1(a)]. In Fig. 5.13(a), the PL emission of a (In,Ga)As/GaAs nanowire illuminated with a defocused laser spot that covers the whole nanowire is displayed. The PL in the lower wavelength range (below 840 nm) is similar to the one observed in pure GaAs nanowires [cf. Fig. 5.1(a)]. The emission lines above 860 nm, however, are absent in sample D. These narrow emission lines are attributed to the incorporation of In in the (In,Ga)As segment leading to localized emission centers at the top of the nanowire. Interestingly, the emission lines, even though with much lower intensity, are extended into the GaAs section of the (In,Ga)As/GaAs nanowires. This could be due to unintentional lateral growth of a thin (In,Ga)As layer on the sidewalls of the GaAs section, as has been reported for axial growth of InAs-GaAs [34], GaAs/InGaAs/GaAs [190, 191] and InGaAs nanowires [63]. However, the

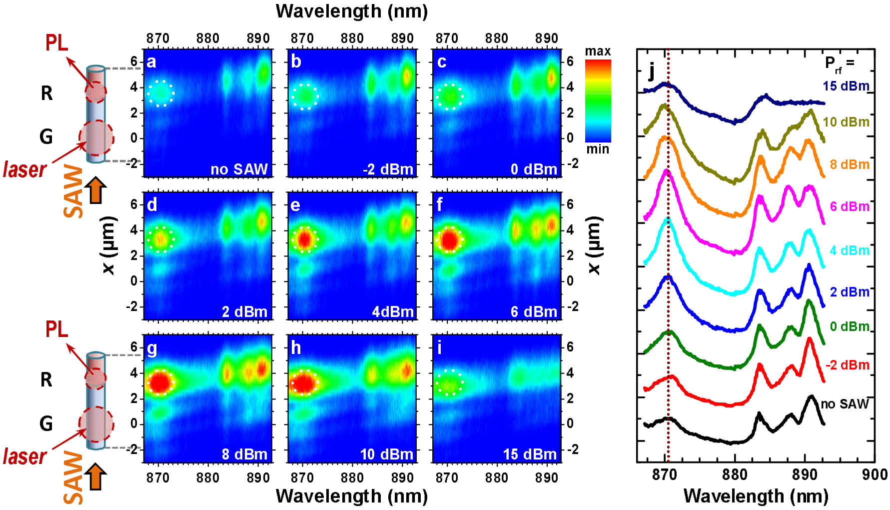

***Figure 5.14.:*** (a-i) PL images of a (In,Ga)As/GaAs nanowire excited by a tightly focused laser beam close to the bottom end of the nanowire of the GaAs section (cf. left inset) for different acoustic amplitudes. Acoustic charge transport can be observed for moderate acoustic powers. (j) PL integrated from −3 to 7.5 µm. The dashed circles in (a-i) and the dotted line in (j) mark the selected emission line for the autocorrelation measurements presented in the next chapter.

spectral shape of these emission lines in the GaAs region is almost the same as in the (In,Ga)As segment indicating that the emission is rather due to a waveguide effect that guides the PL from the (In,Ga)As segment into the GaAs region, transparent in that spectral range [cf. Fig. 5.1(a)].

In Fig. 5.13(b), the PL image under the application of a SAW with an acoustic wavelength, frequency and power of $\lambda_{\mathrm{SAW}} = 11.67\,\mu\mathrm{m}$, $f_{\mathrm{SAW}} = 338\,\mathrm{MHz}$ and $P_{\mathrm{rf}} = 9\,\mathrm{dBm}$, respectively, is depicted. The acoustic modulation broadens the emission lines and reduces the overall PL intensity, similar to the quenching observed in pure GaAs nanowires [cf. Figs. 5.1(a) and (b)]. However, the PL reduction is more pronounced in the lower wavelength range associated with the GaAs section. This is attributed to the higher ionization probability of the carriers in these emission centers. The electrons and holes becomes separated in the type-II band structure modulated by the SAW and are transferred to the (In,Ga)As section where they recombine.

In order to investigate the transport process in these nanowire in more detail, PL and TRPL measurements have been carried out. In the Figs. 5.14(a-i) the PL images for photoexcitation at the GaAs section (G, left insets) with a focused laser spot as a function of the acoustic power are displayed for a shortened wavelength region. The increase in SAW power enhances the remote emission at R (cf. left insets) from the (In,Ga)As segment on top of the nanowire, similar to the behavior observed for GaAs nanowires in Sec. 5.2 due to the charge transport of electrons and holes along the nanowire. The corresponding integrated intensity between $-3$ and 7.5 µm of the PL images are presented in Fig. 5.14(j). The emission line around 870 nm – marked with a dashed circle and a dotted line, respectively – exhibits the highest remote PL emission under acoustic excitation. In addition, this line is spectrally separated from the other emission centers which makes it suitable for the autocorrelation measurements presented in the next chapter. For high acoustic powers ($> 10$ dBm) the PL emission gets quenched over the whole spectral range [see Figs. 5.14(h-i)] due to the strong piezoelectric field which reduces the radiative recombination probability. Furthermore, the emission lines get broadened.

Note that the intensity and the spectral width of the narrow emission lines observed at longer wavelength in the GaAs region depends in the same manner on the acoustic power as the PL emission in the (In,Ga)As section [Figs. 5.14(a-i)]. In particular, the PL intensities of the narrow lines increase at moderate rf powers in contrast to the behavior of the emission of the GaAs-related lines in the shorter wavelength region ($< 840$ µm, cf. Fig. 5.13). To support the assignation of these narrow lines to a waveguide effect, additional measurements, directly exciting the (In,Ga)As section by a focused laser (G = R), were carried out. The PL images were recorded for different light excitation powers, but without applying a SAW, and are presented in Fig. 5.15. Due to the small dimensions of the nanowire, carriers may be excited directly in the GaAs section. However, the experiments verify that the narrow lines follows closely the behavior of the lines detected in the (In,Ga)As segment, thus corroborating the association of the narrow lines to the guiding of the light from the emission centers in the (In,Ga)As segment.

The TRPL measurements provide information about the dynamics of the transport process in the nanowire. Fig. 5.16 and Fig. 5.17 display the

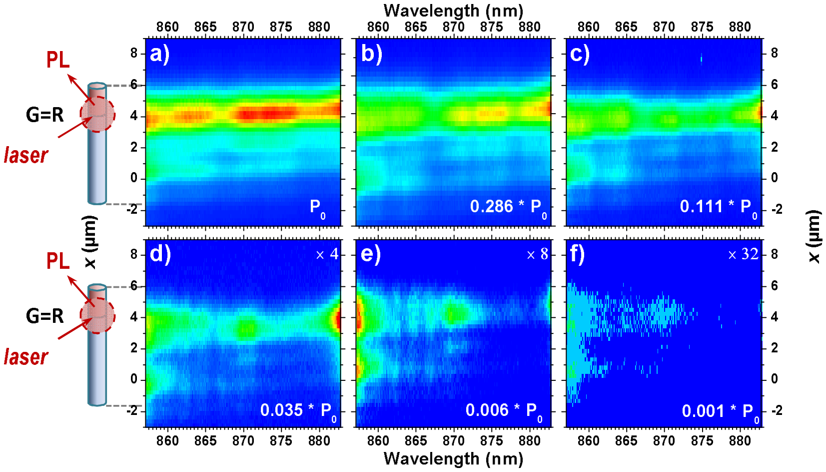

***Figure 5.15.:*** (a-f) PL images of a (In,Ga)As/GaAs nanowire excited by a tightly focused laser beam on the (In,Ga)As section (cf. left inset) for different light excitation powers in terms of $P_0 = 4.68\,\mu\mathrm{W}$.

spatio-temporal PL integrated in the wavelength range from 811.7 nm to 838.2 nm and from 867.1 nm to 892.7 nm, respectively. The plots were recorded for different SAW phases $\tau/T_{\mathrm{SAW}}$. Fig. 5.16, which represents the GaAs-related emission, shows that the PL at the generation site (G) persists over several SAW periods. The same behavior is observed for the (In,Ga)As-related emission presented in Fig. 5.17. The recombination pulses are detected over the whole time scale. The corresponding TRPL profiles integrated at G and R are displayed in Figs. 5.18(a) and (b), respectively. For the dynamics, the same simple physical picture as in Fig. 5.5 – the carrier motion is analogous to the slide of a ball on an oscillating seesaw whose difference of end-point heights is proportional to the potential difference between G and R $\Delta\Phi_{\mathrm{SAW}}(t)$ (see Sec. 5.3) – is considered which is depicted in the insets of Fig. 5.16. Note that at time $t = 0$, when the laser pulse arrives, strong PL intensities are observed at G *and* R. The pulses at R may be attributed to the small distance between G and R ($\sim 3\,\mu\mathrm{m}$) which enables the photoexcitation of carriers near R which can diffuse to the trap and recombine immediately after the laser pulse.

For $0 < \tau/T_{\mathrm{SAW}} \leq 4/9$, $\Delta\Phi_{\mathrm{SAW}}(0)$ (cf. insets of Fig. 5.16) is positive

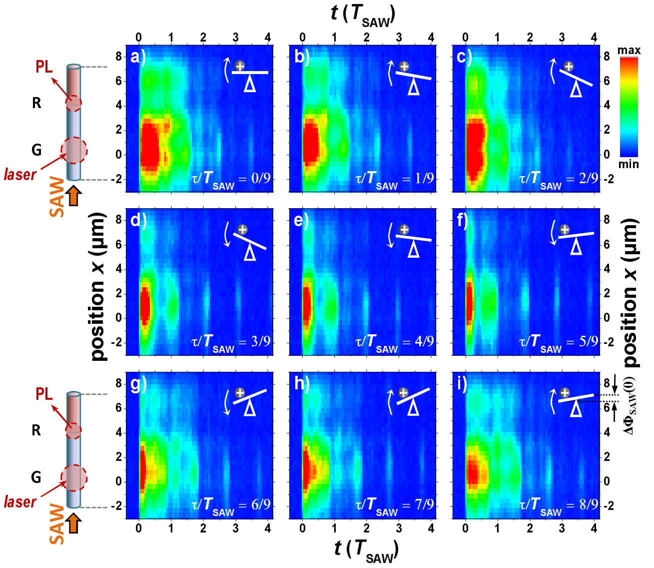

***Figure 5.16:*** Spatio-temporal PL integrated in the wavelength range from 811.7 nm to 838.2 nm. On the vertical axis the position $x$ along the nanowire axis and on the horizontal scale the time delay $t$ with respect to the arrival time of the excitation laser pulse are presented. (a-i) The plots were recorded for different SAW phases $\tau/T_{\mathrm{SAW}}$ and fixed SAW power ($P_{\mathrm{rf}} = 4\,\mathrm{dBm}$).

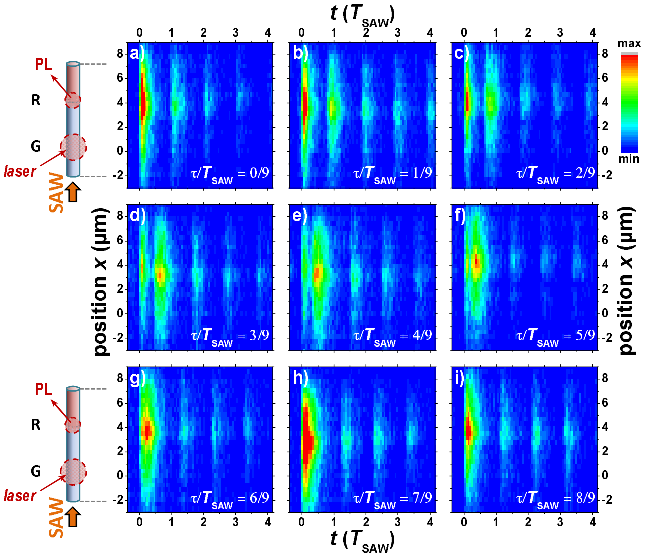

***Figure 5.17:*** Spatio-temporal PL integrated in the wavelength range from 867.1 nm to 892.7 nm. On the vertical axis the position $x$ along the nanowire axis and on the horizontal scale the time delay $t$ with respect to the arrival time of the excitation laser pulse are presented. (a-i) The plots were recorded for different SAW phases $\tau/T_{\mathrm{SAW}}$ and fixed SAW power ($P_{\mathrm{rf}} = 4\,\mathrm{dBm}$).

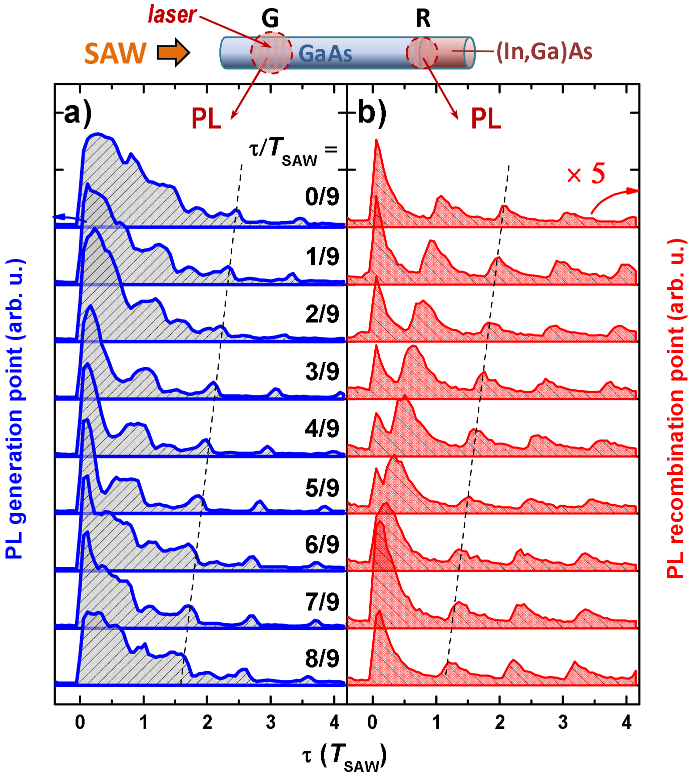

***Figure 5.18.:*** Time-resolved PL profiles integrated at G (a) and R (b) for different $\tau/T_{\mathrm{SAW}}$ ratios.

leading to the motion of one carrier species, say holes, towards R. When $\Delta\Phi_{\mathrm{SAW}}(t)$ changes sign, the holes are driven back to G and the electrons are transferred to R. However, a recombination pulse at R is hardly observed [cf. Fig. 5.17 and Fig. 5.18(b) at $\tau = 1/2\,T_{\mathrm{SAW}}$]. A significant pulse is only detected when $\Delta\Phi_{\mathrm{SAW}}(t)$ changes sign another time ($\tau = 1\,T_{\mathrm{SAW}}$) initiating a further hole motion towards R. This suggests that only one carrier species can be efficiently trapped at R. Recombination of these carriers, previously transferred and trapped at R, takes place when the oppositely charged carriers are driven to the trap. This process repeats many times leading to light pulses every SAW cycle. The same picture can be observed for $5/9 < \tau/T_{\mathrm{SAW}} \leq 1$. The difference is that in the first half cycle the oppositely charged carriers, say electrons, are transported to R [$\Delta\Phi_{\mathrm{SAW}}(t)$ is negative], where they are trapped, and recombination pulses are detected when $\Delta\Phi_{\mathrm{SAW}}(t)$ changes sign for the first time [cf. Fig. 5.17 and Fig. 5.18(b)]. Interestingly, the PL at G is stronger when electrons are transferred towards R. Due to the oscillating motion of carriers along the nanowire axis, holes are driven back from R to G in the same period. This suggests that there exist traps at G which efficiently capture electrons. Thus, a strong PL pulse at G occurs when the holes are driven back to G and recombine with the trapped electrons.

The results show that only one type of charge carriers is efficiently trapped in this (In,Ga)As/GaAs nanowire. As mentioned before, the band alignment between GaAs and (In,Ga)As is of type-I [185, 186], which generally favors the trapping of both electrons and holes in the (In,Ga)As sections of the nanowire. However, since the conduction band offset ($\Delta E_{\mathrm{C}}$) in relation to the band gap difference $\Delta E_{\mathrm{g}}$ is in the range of $0.6 - 0.9$ and $\Delta E_{\mathrm{g}}$ is approximately $70 - 80\,\mathrm{meV}$ for an In content of $x = 0.05$ [187], the valence band offset ($7 - 32\,\mathrm{meV}$) may be too small to capture holes efficiently. The larger conduction band offset rather suggests that electrons are the carrier species efficiently trapped in the nanowire. For an unambiguous assignment, however, more investigation is required.

## 5.7. Summary

In this chapter, the results of the acoustic transport of carriers in GaAs and (In,Ga)As/ GaAs nanowires and their recombination characteristics have been presented. It has been shown that under the high-frequency piezoelectric field of a SAW photoexcited electrons and holes can be transferred along the nanowire axis to a second location where they recombine. The dynamics of the transport have been studied by TRPL spectroscopy. The obtained results reveal sub-nanosecond recombination pulses at a remote position synchronized with the SAW phase.

In the case of GaAs nanowires, additional polarized PL experiments have been carried out. The results together suggest that two types of recombination pulses exist which occur at different positions and energies on the nanowire. The $h \rightarrow e$ pulses are emitted from the zincblende region at R where electrons become trapped and recombine with holes transferred in a subsequent SAW half cycle. This is consistent with the observed emission polarized parallel to the nanowire axis, as expected for zincblende nanowires. The $e \rightarrow h$ pulse are attributed to the recombination of trapped holes in alternating wurtzite/zincblende sections. Due to the type-II band alignment holes can be trapped in small wurtzite sections embedded in zincblende phases. The recombination of these holes with transferred electrons yields PL pulses that are similar in energy to the $h \rightarrow e$ pulses due to quantum confinement effects in the wurtzite sections. These pulses could not be resolved in the polarized PL measurements. This may be due to the proximity of the peak energies or associated to the lack of alternating wurtzite/zincblende sections or the lack of quantized states. The latter leads to the recombination of holes from the wurtzite valence band and electrons from the zincblende conduction band which have emission energies that are lower than the detected wavelength range in these experiments.

Spin polarization-resolved PL measurements have confirmed that the emission is mainly linear polarized and that no excess of one spin polarization can be obtained during the transport process.

The PL results obtained from a (In,Ga)As/GaAs nanowire have revealed that, in comparison with the GaAs nanowires, the growth of an (In,Ga)As segment at the top of the nanowire leads to additional PL emission lines ranging from 800 nm to 930 nm. PL experiments have shown that acoustically transferred carriers can be trapped in this inserted segment. However, the trapping is efficient only for one type of carriers. The type-I band alignment between GaAs and (In,Ga)As and the higher conduction band offset difference, compared to the one for the valence bands, suggest that the trapping in the (In,Ga)As segment is more efficient for electrons than for holes.

In conclusion, the high-frequency contactless manipulation of carriers in single nanowires by SAWs allows to transport photoexcited carriers along the nanowire axis and their recombination on a sub-nanosecond time scale. This opens new perspectives for applications of nanowires in optoelectronic devices which operate at GHz frequencies. The potential of this approach is demonstrated in the next chapter where a high-frequency source of antibunched photons based on the acoustic carrier transport in (In,Ga)As/GaAs nanowires is presented.

# 6. Acoustically driven single-photon emission in single nanowires

In this chapter, the autocorrelation measurements of a GaAs and an (In,Ga)As/GaAs nanowire are presented. The transport experiments presented in the last chapter have revealed that the remote recombination is restricted to a few emission centers. This opens the way for a high-frequency source of antibunched photons based on the acoustic transport of electrons and holes.

In light sources, the emitted photons are typically statistically distributed in a given time interval which leads to noise in optical measurements. In order to suppress the number of photon fluctuations one needs to control the emission of photons in time. Such an ideal light source is able to emit an exact number of photons in a defined time interval making it suitable for optical measurements with very low noise level. In the last few decades, single-photon emitter generating one photon on demand have attracted lots of interest due to the promising applications in the field of quantum information [126].

For the realization of a high-frequency turnstile single-photon source, Wiele *et al.* proposed the pumping of semiconductor quantum dots with SAWs that deliver an alternating sequence of electrons and holes [192]. Based on the pumping of quantum dots with SAWs, Couto *et al.* realized a high-frequency single-photon source in an array of quantum dots embedded in a GaAs quantum well structure [124]. Furthermore, it has been shown that InAs quantum dots embedded in an GaAs microcavity structure can generate a train of single-photon pulses which in the case of a spectrally isolated quantum dot yield a nearly ideal single-photon source [193]. More recently, Claudon *et al.* demonstrated a highly efficient single-photon source in an InAs quantum dot embedded in a GaAs photonic nanowire [38].

Here, an *acoustically driven* high-frequency single-photon source has been realized for the (In,Ga)As/GaAs nanowire investigated in the last chapter. In the following section, the results of the autocorrelation measurements and the demonstration of antibunched photon emission are highlighted. Then, a summary is given.

## 6.1. Photon autocorrelation measurements

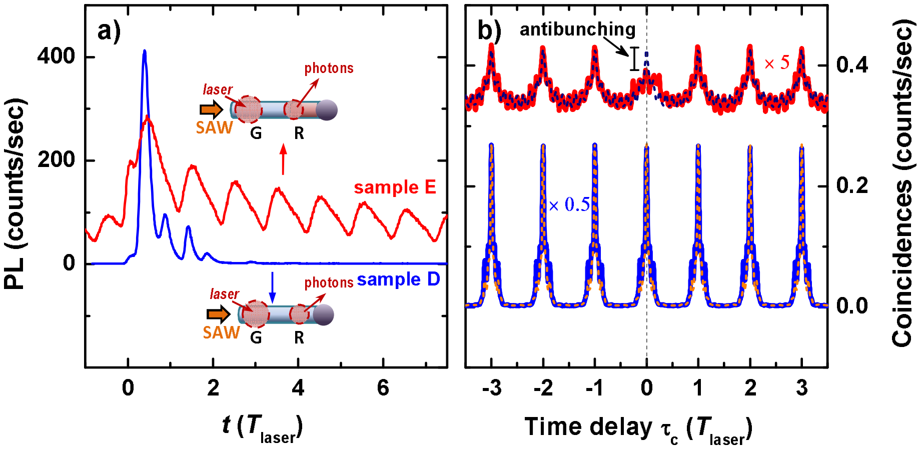

***Figure 6.1.:*** (a) Time-resolved PL at the remote position R of a GaAs nanowire (blue curve, sample D) and an (In,Ga)As/GaAs nanowire (red curve, sample E). Photoexcited carriers at G are transferred acoustically to R where they recombine. (b) Autocorrelation measurements of sample D (blue solid line) and sample E (red solid line) and the corresponding numeric autocorrelations (dashed lines) of the time-resolved spectra from (a). For the measurements the acoustic frequencies $f_{\mathrm{SAW,D}} = 226.8\,\mathrm{MHz}$ and $f_{\mathrm{SAW,E}} = 338.4\,\mathrm{MHz}$ with amplitudes $P_{\mathrm{rf,D}} = 8\,\mathrm{dBm}$ and $P_{\mathrm{rf,E}} = 15\,\mathrm{dBm}$ have been used for sample D and sample E, respectively.

In this section, the realization of a single photon source based on the acoustic transport of photoexcited carriers is presented. As seen in the previous chapter for GaAs and (In,Ga)As/GaAs nanowires, the application of SAWs allows the high-frequency contactless manipulation of photoexcited carriers which can generate light pulses on a sub-nanosecond time scale. This potential can be used for the realization of a high-frequency source of antibunched photons which has been realized for the same (In,Ga)As/GaAs nanowire investigated in the last chapter. For the demonstration that an (In,Ga)As segment at the top of the GaAs nanowires has been necessary to observe photon antibunching, photon autocorrelation experiments have been performed on both the GaAs nanowire (sample D) and the (In,Ga)As/GaAs nanowire (sample E) studied in Secs. 5.1 – 5.3 and Sec. 5.6, respectively, and are presented below.

The photon autocorrelation measurements of the GaAs nanowire and (In,Ga)As/GaAs nanowire were carried out with the Hanbury Brown and Twiss (HBT) setup (see Fig. 3.18) + option D displayed in Fig. 3.13. As in the transport measurements light pulses were focused at G to photoexcite carriers which were transferred acoustically to R along the nanowire axis [cf. Fig. 5.2 (sample D) and Fig. 5.14 (sample E)]. However, for the autocorrelation measurements the PL recombination at R was spectrally filtered to isolate a defined emission line. For the emission centers selected for the analysis – centered at 816 nm and 870 nm for sample D and sample E, respectively –, band pass filters with center wavelengths of 820 nm and 870 nm and a band width of 20 nm have been used. In addition, a second pinhole with 150 μm diameter was put between beam splitter and HBT setup in order to separate spatially the emission at R from other emission centers on the nanowires.

In Fig. 6.1(a), the time-resolved profiles of samples D (pure GaAs) and sample E [(In,Ga)As/GaAs] for a laser pulse arriving at $t = 0$ are presented. The carriers are photoexcited at G and are transferred acoustically to R where they recombine (see insets). The recombination pulses observed in sample E persist over much longer times than the ones detected for sample D. This may be associated with a higher density of trapping centers in the (In,Ga)As/GaAs nanowires which reduces the transport efficiency. Consistent with the previous measurements (Fig. 5.6 and Fig. 5.18), the GaAs nanowire exhibits two defined pulses every SAW cycle while for the (In,Ga)As/GaAs nanowire only one clear pulse (and a shoulder) can be identified which has been explained by the different trapping behavior of transferred electrons and holes.

The corresponding autocorrelation histograms of both samples (solid lines) are displayed in Fig. 6.1(b). The histograms exhibit two periodicities due to the synchronization of the SAW and the laser periods. The short one is attributed to the SAW period ($T_{\mathrm{SAW}}$) and the longer one is related to the laser repitition rate $T_{\mathrm{laser}} = 8T_{\mathrm{SAW}}$. The shape of the histogram of sample D can be reproduced well by the numeric autocorrelation (dashed

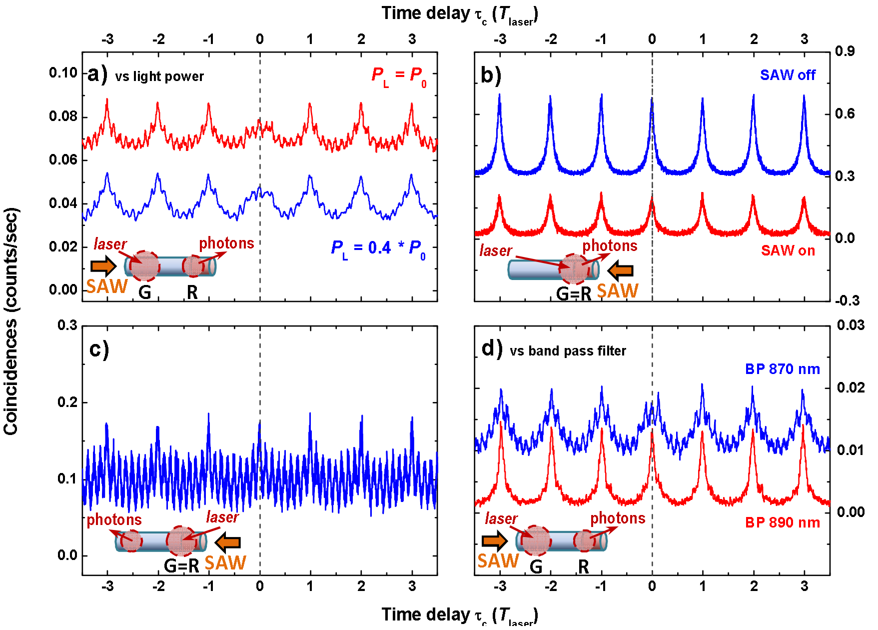

***Figure 6.2.:*** Autocorrelation measurements under different conditions for the same (In,Ga)As/GaAs nanowire. (a) As a function of light power $P_0 = 4.2\,\mu$W. (b) For photoexcitation and detected recombination at the (In,Ga)As segment (G = R, cf. inset) in the absence (blue curve) and presence (red curve) of a SAW. (c) For photoexcitation at the (In,Ga)As segment and detection in the GaAs section. (d) For different band pass filters, 870 nm (blue curve) and 890 nm (red curve).

lines) of the corresponding time-resolved spectra in Fig. 6.1(a). However, the histogram of sample E exhibit a clear reduction in the coincidence rate at the time delay $\tau_c = 0$ which is attributed to the photon antibunching of the emission at R.

To investigate the antibunching effect in more detail, autocorrelation measurements have been carried out for different configurations: i) experiments with different light powers [Fig. 6.2(a)] reveal the same results and does not alter the antibunched emission at R. ii) The direct generation of carriers and the detection of the emission in the (In,Ga)As segment in the absence of a SAW [blue line in Fig. 6.2(b)] does not exhibit an antibunched photon emission. This fact shows the essential role of the acoustic transport for the antibunching in the quantum dot-like structure.

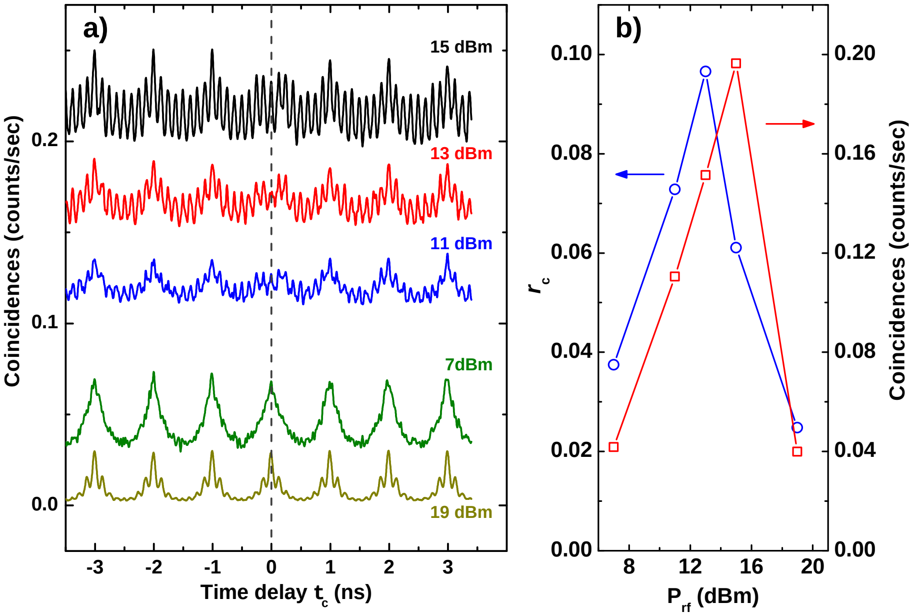

***Figure 6.3.:*** (a) Autocorrelation histograms recorded under the same conditions as for the (In,Ga)As/GaAs nanowire of Fig. 6.1b for different acoustic excitations using a fixed laser intensity. (b) Comparison between the degree of antibunching $r_c$ and average coincidence rate.

The application of acoustic power leads to the same result (red line) even if the detection region is moved to the GaAs region (iii), as can be seen in Fig. 6.2(c). iv) Autocorrelation measurements with different band pass filters – to select a spectral emission range –, but under the same conditions where antibunching has been observed [blue line in Fig. 6.2(d)], reveal that the emission around 890 nm (red line) does not show a measurable antibunching under acoustic excitation. This may be due to the fact that in the spectral range around 890 nm different spectrally not isolated emission lines – from different emission centers – can be observed (Fig. 5.14) which all contribute to the emission signal since the band pass filter has a band width of 20 nm.

To further corroborate the role of the acoustic transport for non-classical light emission, autocorrelation measurements for different acoustic powers have been carried out and are displayed in Fig. 6.3(a). Since the measured coincidences depend on the transport efficiency, the coincidence rate varies strongly with the acoustic power. At $\tau_\mathrm{c} = 0$ the coincidence rate becomes suppressed and the reduction is highest for 13 dBm, which can be seen in Fig. 6.3(b), where the degree of antibunching $r_\mathrm{c}$ (blue circles) and the average coincidence rate (red squares) are depicted. The degree of antibunching is the measured second-order intensity correlation function $g^{(2)}(\tau_\mathrm{c})$ at $\tau_\mathrm{c} = 0$ and represents graphically the reduction of the signal at $\tau_\mathrm{c} = 0$ compared to the signals at $\tau_\mathrm{c} = mT_\mathrm{laser}$ where $m$ is an integer different from zero. According to Eq. 3.27 the average number $n$ of emitted photons can be obtained by $n = 1/r_\mathrm{c}$. From the reduction $r_\mathrm{c} \approx 10\%$ of the coincidence rate $n$ can be estimated to $n = 10$, i.e. that 10 quantum emission centers are present in the detection area. The average coincidence rate – as determined by the average count over the whole time interval – exhibits the same shape as $r_\mathrm{c}$ although the maxima of the curves are slightly shifted. Nevertheless, it shows that the high antibunching levels correlate well with a high transfer efficiency.

## 6.2. Summary

In this chapter, the realization of a high-frequency source of antibunched photons based on the acoustic transport of electrons and holes in an (In,Ga)As/GaAs nanowire has been presented. Photon autocorrelation measurements on the (In,Ga)As/GaAs nanowire have demonstrated the realization of an antibunched photon source. The detection of antibunched photons has been related to the presence of the (In,Ga)As segment. The additional emission lines coming from the (In,Ga)As segment are spread over a wide spectrum with some emission lines well-separated from the others. This provides the possibility to filter a spectrally well-separated emission line, which has been used for the autocorrelation experiments. The spectrally and spatially separation of the emission center reduces the amount of quantum emission centers contributing to the signal and is believed to play a key role for the observation of photon antibunching.

In conclusion, as example for applications of nanowires in optoelectronic devices operating at GHz-frequencies, a source of antibunched photon pulses with high repetition rate based on the acoustically induced pumping of an (In,Ga)As segment embedded in a nanowire has been realized.

However, the number of estimated emission centers (approximately 10) which contribute to the signal is still too high for applications in single-photon sources. Further optimization of these structures will probably provides more efficient GHz-frequency single-photon sources and higher light extraction efficiency, important features for the realization of high bit rates in quantum cryptography.

# 7. Conclusions

In this work, basic research on III-V nanowires has been performed. In particular, the optical properties of wurtzite InAs nanowires have been determined by Raman scattering and PL spectroscopy. In addition, it has been demonstrated the application of III-V nanowires as non-classical photon sources. It has been shown that photoexcited carriers can be transferred to a remote location in the nanowire where the recombination of carriers leads to sub-nanosecond light pulses. This high-frequency contactless manipulation of carriers has been used to realize a source of antibunched photons in (In,Ga)As/GaAs nanowires.

Polarized Raman scattering experiments on a single InAs nanowire have been performed. The polarization dependence of the TO and LO modes has been determined. The highest intensity for the TO mode is obtained in the $x(y,y)\bar{x}$ configuration, where the incident and scattered polarizations are parallel to each other and perpendicular to the nanowire axis. It has been shown that the contribution to the Raman signal comes from the wurtzite $\mathrm{A_1}$(TO) and $\mathrm{E_2^H}$ optical phonon modes, whereas the wurtzite $\mathrm{E_1}$(TO) mode could not be resolved. Additional resonant Raman scattering experiments on the same nanowire have revealed that the electronic $E_1^{\mathrm{G}}$ transition in the wurtzite structure is approximately 100 meV red-shifted with respect to the one for the zincblende phase, a consequence of the predominant wurtzite structure of the nanowire.

PL measurements of InAs ensembles have revealed two main optical emission bands that have been attributed to the donor-acceptor pair overlapped with the band-to-acceptor transitions and recombinations from carriers in quantum well structures formed by alternating wurtzite/zincblende segments. It has been shown that the excitation power dependence of the PL emission, which blue-shifts with increasing excitation intensities, are in agreement with the type-II band alignment between the wurtzite and zincblende structure predicted theoretically. Furthermore, the successive increase of temperature and excitation power leads to a large blue-shift that is attributed to band bending and band filling effects of confined electrons in the few zincblende sections and to the appearance of the band-to-band transition of the wurtzite structure. This allowed to estimate a lower bound for the wurtzite InAs band gap in nanowires (0.458 eV) that is substantially larger than the zincblende bulk band gap (0.415 eV), in agreement with previous reported works.

Further investigation and experiments are needed to provide more detailed information about the Raman modes and the PL spectrum of wurtzite InAs nanowires. Raman scattering measurements at low temperatures could shed light on the exact determination of the $A_1$(TO), $E_1$(TO) and $E_2^H$ optical phonon modes since the linewidth of the Raman modes shrinks with decreasing temperature. Additional measurements with nanowires that are covered with different dielectric materials could clarify the unambiguous assignation of the low frequency shoulder of the LO mode to surface effects.

Additional PL experiments would assist the determination of the wurtzite InAs band gap. For this, nanowires without stacking faults or passivated surface states as observed for GaAs/AlGaAs core-shell nanowires [26], for InAs/InP nanowires core-shell nanowires [194] and, more recently, for InAs nanowires with a passivated surface using organic sulfide octadecylthiol (ODT) [195] may be needed for a clear determination. In addition, PL excitation measurements on wurtzite nanowires could give further evidence to this issue.

Furthermore, surface acoustic waves (SAWs) have been applied to AlGaAs/GaAs core-shell nanowires transferred to a $LiNbO_3$ substrate in order to transport photoexcited carriers along the nanowire axis to a second location leading to remote emission of sub-nanosecond light pulses synchronized with the SAW phase. Two types of light pulses could be identified coming from the recombination of trapped electrons in the zincblende section of the GaAs nanowire and acoustically transferred holes, on the one hand, and probably from the recombination of trapped holes in alternating wurtzite/zincblende sections and acoustically transported electrons, on the other hand. Additional spin polarization-resolved PL measurements have confirmed that the emission is governed by the linear polarization anisotropy.

The high-frequency contactless manipulation of carriers by SAWs has been used to demonstrate the potential of nanowires in optoelectronic devices operating at GHz frequencies. As an example, the realization of a high-frequency source of antibunched photons based on the acoustic transport of electrons and holes in (In,Ga)As/GaAs axial nanowires with AlGaAs shell has been presented. The insertion of an (In,Ga)As segment at the top of a GaAs nanowire leads to additional emission lines over a wide spectral range and has enabled the detection of photon antibunching. In contrast to GaAs nanowires, the PL spectrum of the investigated (In,Ga)As/GaAs nanowire exhibit an emission line that is spectrally well-separated from the others. The spectrally and spatially separation of the emission line by band pass filters and pin holes reduced the amount of contributing emission centers to the signal which is believed to be fundamental for the observation of photon antibunching.

For future work, the introduction of a quantum dot structure embedded in a GaAs nanowire with nearly perfect interfaces or the axial growth of an InAs section after GaAs nanowire growth [34] may improve the transport and trapping efficiencies for electrons and holes. The optimization of the (In,Ga)As/GaAs nanowire structure will provide more efficient GHz-frequency single-photon sources and higher light extraction efficiency, important features for the realization of high bit rates in quantum cryptography.

# A. Surface acoustic waves and their generation

Surface waves are widespread in nature, science and technology, such as water waves, seismic waves or ultrasonic surface waves in a solid. A common feature of all kinds of surface waves is the localization of the energy close to the surface, within a depth of approximately one wavelength, which confines the motion throughout the two-dimensional interface region [196].

Elastic surface waves, also known as *surface acoustic waves*, were explained in 1885 by Lord Rayleigh [66]. A particular type of these SAWs is the *Rayleigh wave*, named after his discoverer, which has been applied in this work and is considered in the following. Unlike bulk waves, where the longitudinal and transversal modes propagate independently with different velocities, the two modes of the Rayleigh waves are coupled. The longitudinal mode with particle displacements parallel to the propagation direction leads to alternating compressions of the crystal lattice while the oscillations of the transversal mode are oriented perpendicular to the propagation direction. Due to the asymmetry of the elastic forces at the surface, the particle motions parallel and perpendicular to the propagation direction are different yielding a elliptically polarized motion in the sagittal plane defined by the normal to the surface and the SAW propagation direction. Since the particles of the surface are less constrained, the velocity at the surface is smaller than in the bulk. Extensive reviews for SAWs can be found, for example, in Refs. [177, 197]

In the beginning, the main interest in SAWs was limited to seismology and geophysics. This changed with the development of interdigital transducers (IDTs) which extended the frequency range into the GHz region and allowed the generation of SAWs on piezoelectric media. An IDT consist of two interlocked comb-like metallic structures which are fabricated on the surface of a piezoelectric surface. If a radio-frequency (rf) voltage is applied, in a manner that neighboring fingers are oppo-

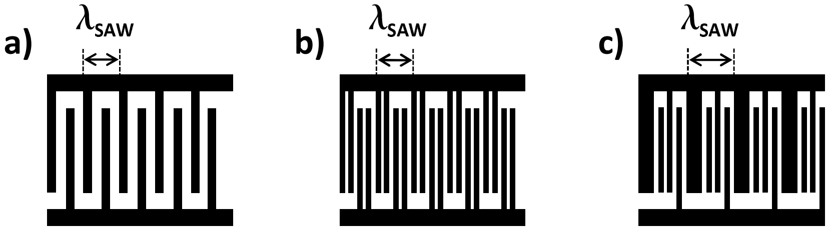

***Figure A.1.:*** Interdigital transducer types: (a) *single-finger* type, (b) *double-electrode* or *split-finger* type and (c) *floating electrode unidirectional transducer* (FEUDT).

site in voltage, an electric field is induced within the substrate which contracts and stretches the surface due to the piezoelectric effect leading to a continuous acoustic wave. In Fig. A.1 three types of IDTs are displayed. In the *single-finger* type [Fig. A.1(a)] each period consist of two fingers with width and separation equal to a quarter of the acoustic wavelength $\lambda/4$. In theses structures, the reflections are large since every finger acts as a reflector at the free-surface/metal interface and the reflector period is $p = \lambda/2$. This fulfills the condition for Bragg reflections where all reflections are superimposed in phase with the Bragg frequency $f_{\mathrm{B}} = v_{\mathrm{SAW}}/2p$, where $v_{\mathrm{SAW}}$ is the phase velocity of the acoustic mode for a certain propagation direction and crystal cut. These reflections can be minimized by using the *split-finger* type displayed in Fig. A.1(b). Every period contains four fingers with width and separation equal to $\lambda/8$ which suppresses the reflections since the Bragg condition is not fulfilled [198]. However, this configuration requires fingers twice as narrow as the ones for single-finger IDTs on operating at the same frequency. In order to control the direction of the generated SAW different unidirectional transducers has been proposed which require internal reflections on the electrodes and a lack of symmetry. In this work we used a floating electrode unidirectional transducer (FEUDT) which is displayed in Fig. A.1(c). In this configuration, the separation and the thin electrodes have a width of $\lambda/10$, whereas every fourth electrode is not connected to the bus bars, referred to as *floating electrode.* The width of the thicker electrodes is $3\lambda/10$. If a SAW encounters the floating electrodes a part of the wave is reflected since the SAW induces a voltage in the floating electrodes which, in turn, generates surface waves again. Due to the reduced symmetry

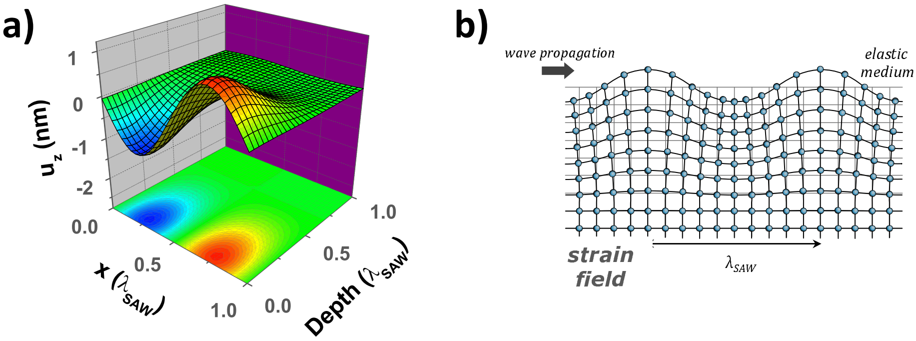

***Figure A.2.:*** (a) Depth dependence of the vertical displacement ($u_z$) along the [110] direction calculated for a Rayleigh SAW propagating on a GaAs(001) crystal (taken from [177]). (b) Strain field of a semiconductor crystal by a SAW.

the reflections are reinforced in one direction and reduced in the other leading to a unidirected SAW wave [199, 200]. Different types of IDTs are used in a variety of signal processing applications such as SAW filters, resonators or sensors in radio, television, mobile communications or even in touchscreen devices.

An important property of a Rayleigh surface acoustic wave is that the wave velocity is approximately $10^5$ times slower than the velocity of electromagnetic radiation in vacuo, and therefore, for the same frequency, the wavelength of the elastic wave is less than the wavelength of the corresponding electromagnetic wave by a factor of $10^5$. This result has immediate importance on the geometry of the resulting device and is the philosophy behind surface wave technology, since the devices themselves can be much smaller than their electromagnetic counterparts.

The SAWs are localized near the surface and consist of the superposition of a longitudinal acoustic mode polarized parallel to the propagation direction of the SAW ($x$-axis) and a transversal mode which is polarized perpendicular to the surface ($z$-axis). This leads to a displacement field $\vec{u}$ with components $\vec{u} = (u_x, 0, u_z)^{\mathrm{T}}$. The spatial distribution of the vertical component of the displacement field $u_z$ for a SAW along the [110] direction on GaAs(001) is shown in Fig. A.2(a) and is taken from [177]. The acoustic amplitude decays from the surface within one wavelength and can reach values up to few nanometers in this case (dependent on square root of acoustic power density) [177]. In Fig. A.2(b) the particle motion in a SAW propagating in an isotropic half-space is illustrated. Along the propagation direction alternating regions of tensile and compressive strain can be observed. Due to the strain and its corresponding piezoelectric potential a dynamic type-II modulation of the electronic band edges is imposed as schematically depicted in Fig. 3.11.

# B. Simulations of acoustic charge transport in nanowires

The simulations were performed by Alberto García Cristóbal, member of our solid state spectroscopy group. The following text is mainly taken from Ref. [iv]:

The simulations of the acoustic transport in the nanowire were carried out by solving the one-dimensional drift/diffusion equations for the electron (n) and hole (p) concentrations under the influence of the SAW field. In order to simulate the excitonic PL maps, the exciton concentration N must also be obtained simultaneously to n and p. The model is a simplified version of that presented in Ref. [201]. In particular, it is assumed that the photoexcited carrier density is sufficiently low to make screening effects negligible. Under these conditions, the drift-diffusion equations for n and p take the form [201]:

$$\frac{\partial n}{\partial t} + \mu_{\mathrm{n}} \frac{\partial}{\partial x}\left(n \frac{\partial \Phi}{\partial x}\right) - \mu_{\mathrm{n}} V_{\mathrm{T}} \frac{\partial^2 n}{\partial x^2} = G - cnp, \tag{B.1a}$$

$$\frac{\partial p}{\partial t} + \mu_{\mathrm{p}} \frac{\partial}{\partial x}\left(p \frac{\partial \Phi}{\partial x}\right) - \mu_{\mathrm{p}} V_{\mathrm{T}} \frac{\partial^2 p}{\partial x^2} = G - cnp, \tag{B.1b}$$

where $\mu_{\mathrm{n}}$ and $\mu_{\mathrm{p}}$ are the electron and hole mobilities, and $V_{\mathrm{T}}$ is the thermal voltage. The rate $G(x,t)$ of photogeneration of electron-hole pairs in the nanowire is taken to mimic the spatial and temporal profile of the laser light impinging on the sample. The term *cnp* is used to represent the rate at which electron-hole pairs are annihilated to form excitons in the ground state, and c is the corresponding exciton formation coefficient. The transport is driven by the potential $\Phi(x,t)$ which, in the simulations presented here, has two contributions, $\Phi(x,t) = \Phi_{\mathrm{SAW}}(x,t) + \Phi_{\mathrm{d}}(x)$. $\Phi_{\mathrm{SAW}}(x,t)$ is the SAW piezoelectric potential along the NW axis and has the form given by Eq. 5.2. In order to simulate the trap at the remote recombination position $x_{\mathrm{r}} = 4\mu\mathrm{m}$, a potential well $\Phi_{\mathrm{d}}(x)$ able to capture both electrons and holes was incorporated.

As discussed in Ref. [201], the various regimes of the acoustically induced charge transport are governed by the dimensionless parameter $\tilde{v}_{\mathrm{n,p}} = 2\pi \left|\Phi_{\mathrm{SAW},0}\right| \mu_{\mathrm{n,p}}/(\lambda_{\mathrm{SAW}} v_{\mathrm{SAW}})$, where $\Phi_{\mathrm{SAW},0}$ and $v_{\mathrm{SAW}}$ are the piezoelectric potential amplitude and wave velocity, respectively. $\tilde{v}_{\mathrm{n,p}}$ is the ratio between the maximum velocity for electrons and holes in the potential and the SAW velocity.

The spatio-temporal dynamics of the exciton concentration $N(x,t)$ is given by the equation:

$$\frac{\partial N}{\partial t} - D_{\mathrm{X}} \frac{\partial^2 N}{\partial x^2} = cnp - \frac{N}{\tau_{\mathrm{X}}} \tag{B.2}$$

where $D_{\mathrm{X}}$ is the exciton diffusion constant and $\tau_{\mathrm{X}}$ is the exciton lifetime for radiative recombination. Here, the measured PL intensities are compared with the calculated exciton recombination rate given by $I_{\mathrm{PL}}(x,t) = N(x,t)/\tau_{\mathrm{X}}$.

The details of the numerical procedure for solving the system of differential equations given by Eqs. B.1 and 5.2 are described in Ref. [201]. The numerical simulations require, among other parameters, the SAW potential amplitude as well as carrier mobilities. For definiteness the typical values $\Phi_{\mathrm{SAW},0} = 0.11$, $\mu_{\mathrm{n}} = 10000$ and $\mu_{\mathrm{p}} = 1000\,\mathrm{cm}^2/\mathrm{Vs}$ are taken, yielding the dimensionless parameters $\tilde{v}_{\mathrm{n}} = 17$ and $\tilde{v}_{\mathrm{p}} = 1.7$, which results in efficient acoustic transport for both types of carriers. The size and depth of the trap potential $\Phi_{\mathrm{d}}(x)$ at $x_{\mathrm{r}} = 4\mu\mathrm{m}$ was assumed to be sufficiently large to prevent carrier extraction by the SAW field. Note that the model can be easily modified to address other situations.

Figure B.1d reproduces the time-resolved PL profiles at R of Fig. 5.6(a) of the main text. These profiles are compared with the simulations performed under the mentioned conditions for intrinsically undoped nanowires (Fig. B.1a). Both sets of curves show a good agreement except for two important differences. For $\tau/T_{\mathrm{SAW}} < 3/9$ the experimental curves show a second remote PL pulse in Fig. B.1d that does not appear in the simulations. The origin of this peak is attributed to the partial detrapping of holes from the traps and their subsequent return to R half a SAW cycle latter, when they recombine with trapped electrons. These second pulses do not appear in the simulations since the deep trapping potential prevents carrier detrapping and forces all carriers to recombine for $t < T_{\mathrm{SAW}}$.

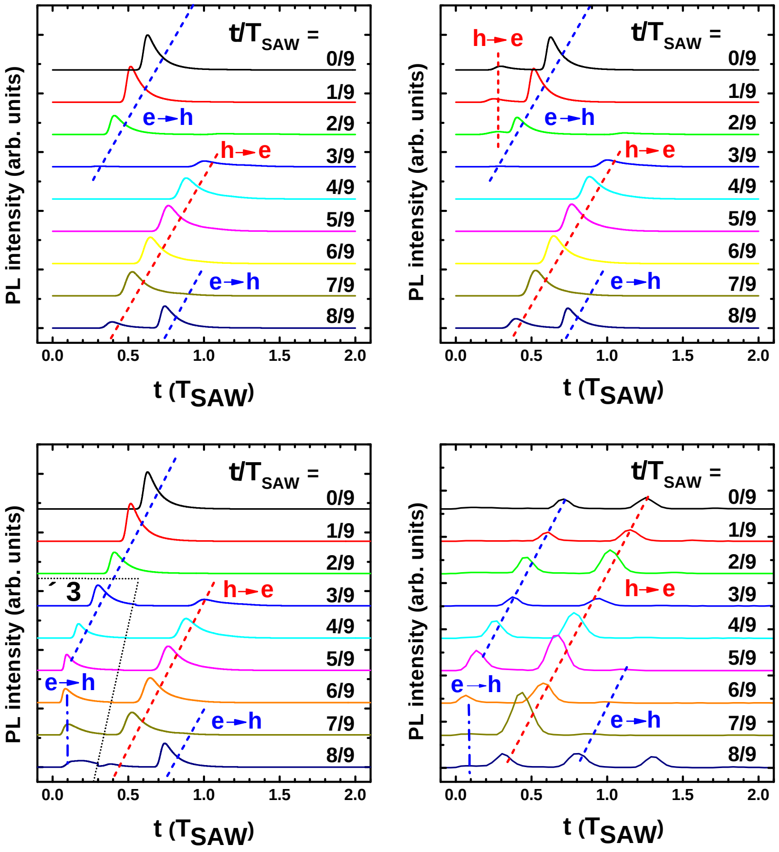

***Figure B.1.:*** Simulation of the time evolution of the remote PL calculated for an intrinsic nanowire (a), assuming the remote trap at R is initially populated by electrons (b) or holes (c) for different phases $\tau/T_{\mathrm{SAW}}$ of the piezoelectric potential at the arrival time of the laser pulses ($t = 0$). (d) Measured profile of the remote PL. Pulses $h \rightarrow e$ denote the recombination events where transported holes recombine with electrons trapped close to R. The same applies for $e \rightarrow h$ pulses, simply exchanging the role of electrons and holes. The initial population of the remote traps by electrons and holes leads to different delays for the pulses indicated by the dash-dotted lines.

In the experiments, PL pulses are also observed at short times $t < 0.4\,T_{\mathrm{SAW}}$ [dot-dashed lines in Fig. B.1(d)]. This pulses could not be reproduced by simulations of intrinsic nanowires carried out for different values of carrier mobilities and amplitudes of the SAW field. They can, however, be reproduced if the traps are assumed to be populated prior to the arrival of the laser pulses. The differences in the simulation results between initial population by holes and electrons are discussed, which are displayed in the simulated profiles of Figs. B.1(b) and B.1(c), respectively.

The overall shape of the PL profiles is very similar in these two cases with the main difference being the pulses at short times indicated by the dot-dashed vertical lines. Note that these pulses arrive at earlier times for initial hole population. The arrival time of these pulses is dictated by the transfer of one type of carriers (electrons or holes) from the illumination area to the populated trap. Due to the higher electron mobility, the transfer is faster when electrons are transferred to a hole-filled trap than when holes need to be transferred. An initial population of the traps with holes leads, therefore, to a better agreement with the experimental dynamics displayed in Fig. B.1(d). An initial hole population is also consistent with the fact that nominally undoped GaAs layers grown under similar conditions were observed to be p-type. The holes, therefore, probably arise from the ionization of acceptor centers in the nanowire.

# C. Additional experimental data

In this section, additional experimental results are presented that support the conclusions taken in the main body of the work. For a better reading of the work, they are excluded from the main body and added in this appendix chapter.

### Additional resonant Raman measurements (Ch. 4)

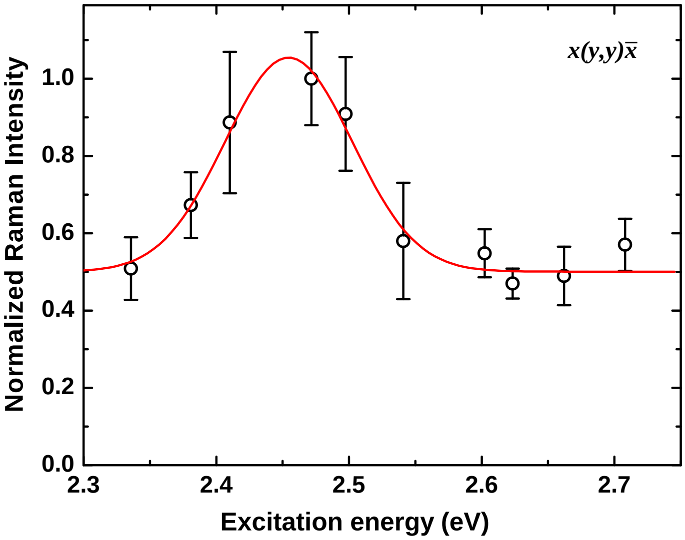

***Figure C.1.:*** Resonant Raman scattering of an InAs nanowire from sample A as a function of the laser excitation energy for the TO mode in $x(y,y)\bar{x}$ polarization configuration (open circles). The solid line represents a Gaussian fit to the data revealing a maximum at 2.45 eV. The standard deviation of at least three measurements is used as error bars.

## Additional PL results (Ch. 5)

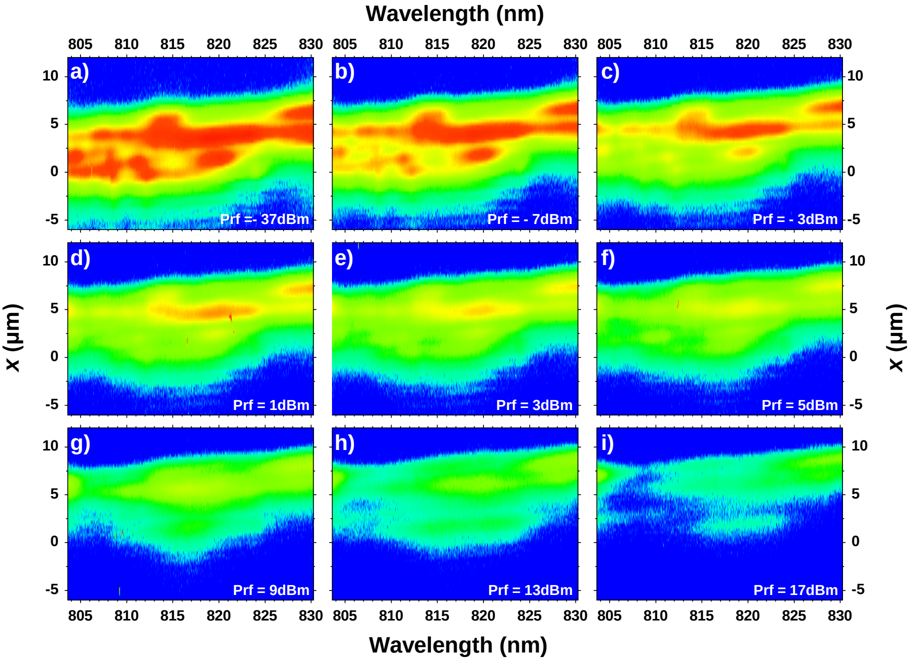

***Figure C.2.:*** (a-i) PL images of a single GaAs nanowire illuminated by a expanded laser spot as a function of acoustic power.

# Resumen en español

Los nanohilos semiconductores están atrayendo una considerable atención debido a su prometedor potencial como bloques de construcción de avanzados dispositivos electrónicos y optoelectrónicos [1]. Han sido propuestos para una amplia gama de aplicaciones que van desde interconectores a elementos de dispositivos activos. Debido a los avances en el crecimiento y las metodologías de fabricación, se crecen los nanohilos de manera muy controlada, lo cual abre nuevas oportunidades hacia la comprensión y la utilización de las propiedades físicas únicas de estos sistemas de baja dimensionalidad.

Este trabajo abarca la caracterización óptica de nanohilos semiconductores III-V y su aplicación para el transporte de carga y emisión de fotones únicos. Los nanohilos de InAs han sido investigados por la dispersión de Raman y la espectroscopia de fotoluminiscéncia (PL). La posibilidad de hacer crecer nanohilos con estructura cristalina diferente de su contraparte de bulk ha despertado mucho interés en sus propiedades ópticas y electrónicas.

Los nanohilos de InAs se han crecido con el método de VLS (*vapor-liquid-solid*) en un sistema de CBE (*chemical beam epitaxy*) utilizando nanopartículas de oro como catalizadores que se dispersan en agua. Tres muestras crecidas a diferentes temperaturas – 420 °C (muestra A), 450 °C (muestra B) and 480 °C (muestra C) – se han analizado. Para la caracterización de los nanohilos, se han realizado estudios de microscopía electrónica de barrido (SEM) y microscopía electrónica de transmisión (TEM) [véase fig 1(Ia-f)]. Los nanohilos de la muestra A tienen forma de aguja, mientras que los nanohilos de las muestras B y C tienen forma de varilla. Los diámetros medios de los nanohilos son 103 ± 22 nm, 71 ± 14 nm y 51 ± 18 nm con una longitud media de 1,5 ± 0,5 µm, 1,9 ± 0,9 µm y 3,4 ± 2,9 µm para la muestra A, B y C, respectivamente (un resumen de los valores se dan en tab. 1).

Los nanohilos de todas las muestras (A, B y C) presentan una estructura predominantemente de wurtzita, en algunos casos la presencia de franjas

| Muestra | diametro | longitud | forma |
|---|---|---|---|
| Sample A | 103 ± 22 nm | 1,5 ± 0,5 µm | forma de aguja |
| Sample B | 71 ± 14 nm | 1,9 ± 0,9 µm | forma de varilla |
| Sample C | 51 ± 18 nm | 3,4 ± 2,9 µm | forma de varilla |

***Table 1.:*** Diametro medio, longitud media y forma de los nanohilos de InAs de las muestras A, B y C.

de zincblenda (*stacking faults*) se ha observado. Todos los nanohilos se crecieron a lo largo de la dirección [0001] (wurtzita) y [111] (zincblenda), respectivamente.

Los nanohilos auto-asistidos de GaAs (muestra D) se crecieron con el método VLS en un sistema de MBE (*molecular beam epitaxy*) y están cubiertos con un revestimiento de $\mathrm{Al_{0.1}Ga_{0.9}As}$ [véase fig 1(II)]. Los nanohilos considerados en este trabajo (muestra D) son de 9 ± 1 µm de largo y se componen de un núcleo de GaAs sin dopar de 106 ± 18 nm recubierto con un revestimiento de 22 ± 9 nm de $\mathrm{Al_{0.1}Ga_{0.9}As}$.

Los núcleos de los nanohilos de (In,Ga)As/GaAs se crecieron en la misma manera que los nanohilos anteriores. Sin embargo, en las últimas etapas de deposición de MBE se exponen un flujo de In y As (muestra E). Esto conduce a una formación de sección corta que contiene inclusiones de In de aproximadamente 300 nm de largo que, en la siguiente, se denota como sección de (In,Ga)As [véase fig 1(III)]. Debido a las condiciones modificadas de crecimiento con MBE, el segmento de (In,Ga)As tiene un diámetro mayor (200 nm), así como una mayor densidad de defectos planares en comparación con la muestra D. La longitud media de los nanohilos de esta muestra es de aproximadamente 7µm.

Los resultados de la dispersión de Raman resonante en un nanohilo individual de InAs con estructura wurtzita se ha realizado para determinar la energía de la transición $E_1^{\mathrm{G}}$ de la estructura wurtzita que es aproximadamente 100 meV menor que la de la fase de zincblenda (véase fig. 2). Este resultado ha sido soportado por un cálculo ab-initio de las bandas electrónicas de la estructura para wurtzita y para zincblenda de Luis C. O. Dacal. Experimentos adicionales de dispersión de Raman polarizado ha revelado la mayor intensidad de Raman para el modo óptico transversal (TO) en configuración $x(yy)\bar{x}$, donde las polarizaciones de la

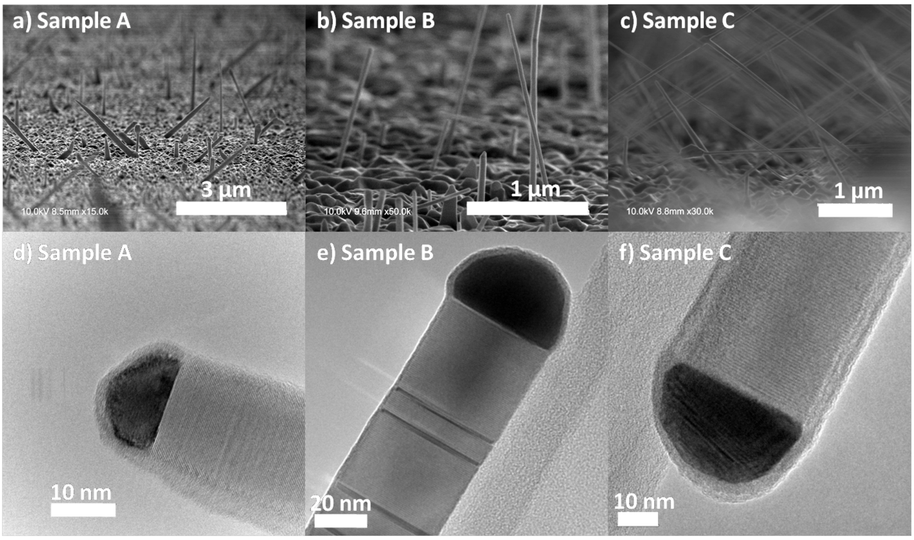

(I) Sample A, B and C

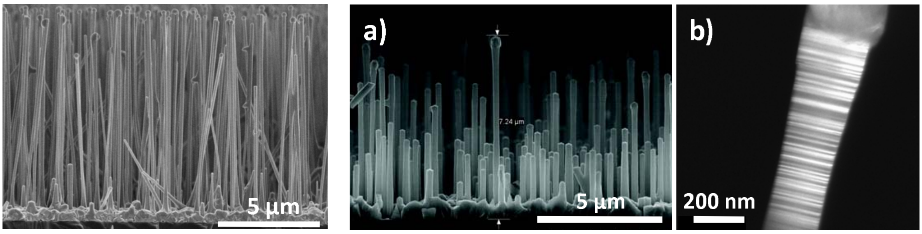

(II) Sample D

(III) Sample E

***Figure 1.:*** (I) Imágenes de SEM de nanohilos de InAs crecidos a 420 °C (Ia), 450 °C (Ib) and 480 °C (Ic). Imágenes correspondientes de TEM de la muestra A (Id), la muestra B (Ie) y la muestra C (If). (II) Imagen de SEM de nanohilos de GaAs (sample D). (IIIa) Imagen de SEM de nanohilos de (In,Ga)As/GaAs (sample E). (IIIb) Imagen de TEM del segmento cerca de la punta del nanohilo.

luz incidente y dispersa son paralelas entre sí y perpendiculares al eje del nanohilo. Desde la dependencia de la polarización, los modos ópticos de $A_1(TO)$ y $E_2^H$ de la estructura de wurtzita se han podido identificar y concuerdan bien con los modos de fonones calculados para la fase wurtzita por un modelo avanzado de iones rígidos de 11 parámetros. El modo $E_1(TO)$ no se pudo resolver. Un hombro, que se detectó en el lado de

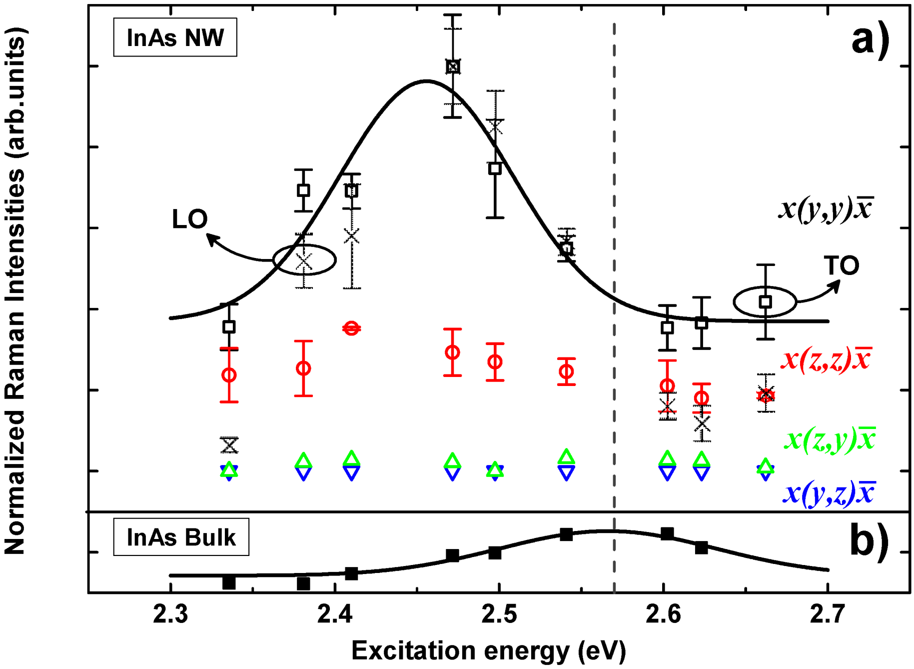

***Figure 2.:*** (a) Raman resonante de un nanohilo individual de InAs en función de la energía de la excitación del láser para el modo TO en las cuatro configuraciones principales de polarización (símbolos abiertos) y para el modo óptico longitudinal (LO) en configuración de $x(y,y)\bar{x}$ (símbolos cruzados, ×). La línea continua representa un ajuste gaussiano a los cuadrados abiertos. La desviación estándar de al menos tres medidas se utiliza como barras de error. (b) Medida de referencia del bulk de InAs (cuadrados rellenos).

baja frecuencia del modo LO, ha sido asignada al modo superficial (SO) que sólo aparece en la configuración $x(y,y)\bar{x}$.

Las medidas de PL de *ensembles* de InAs han demostrado que la banda prohibida de nanohilos de InAs con estructura de wurtzita es sustancialmente mayor que la de zincblenda en bulk (0,415 eV) y un límite inferior para la banda prohibida de wurtzita se ha estimado (0,458 eV). Las medidas están en buen acuerdo con los estudios teóricos disponibles [47, 48, 54]. Los trabajos experimentales obtenidos mediante la extrapolación de las medidas de fotocorriente de nanohilos de $InAs_{1-x}P_x$ [59] y mediante estructuras bidimensionales de wurtzita [60] indican valores de 0,54 eV y 0,52 eV, respectivamente. Un trabajo más reciente sobre nanohilos de InAs, predominante con estructura de zincblenda, indican una banda prohibida de wurtzita de 0,50 eV [65]. Sin embargo, según el conocimiento del autor el valor de la banda prohibida de nanohilos puros de wurtzita no se ha publicado hasta el momento.

Los espectros obtenidos por PL han revelado dos bandas principales de emisión óptica atribuidas a la transición dador-aceptador y la recombinación de portadores en estructuras de pozos cuánticos formados por secciones alternativas de wurtzita y zincblenda a lo largo del eje de los nanohilos. Un gran corrimiento hacia el azul del último, observado cuando la potencia de excitación se incrementa, es coherente con una alineación de banda de tipo-II entre las fases wurtzita y zincblenda predichas por trabajos teóricos. Las medidas adicionales de PL dependientes de la temperatura han mostrado un corrimiento hacia el azul en contraste con la reducción habitual de la banda prohibida de semiconductores con la temperatura creciente [véase fig. 3(a)]. Un sucesivo aumento de la potencia de excitación ha revelado un mayor corrimiento hacia el azul de esta banda que se atribuye a la aparición de la transición banda-banda [véase fig. 3(b)]. A partir de estos resultados un límite inferior para la banda prohibida de wurtzita se ha estimado en 0,458 eV, de acuerdo con los trabajos previos.

Estos resultados arrojan luz sobre las propiedades electrónicas, estructurales y ópticas de la fase wurtzita en nanohilos de InAs. La caracterización de nanohilos es fundamental para la determinación de sus propiedades físicas y para la aplicación en dispositivos optoelectrónicos. En los últimos años, una gran cantidad de trabajos ha sido publicado sobre las propiedades físicas de las fases wurtzita y zincblenda en nanohilos semiconductores III-V, pero aún hay mucho trabajo con el fin de obtener una imagen clara de las propiedades de los nanohilos. Un problema en el caso de InAs es que es un material que – debido a su espacio de banda estrecha – emite en la región del infrarrojo, un rango espectral donde los fotodetectores tienen una eficiencia óptica muy baja. Como ejemplos de la idoneidad para la aplicación de nanohilos en dispositivos optoelectrónicos, se ha considerado nanohilos de GaAs and (In,Ga)As/GaAs que presentan centros de emisión entre 800 nm y 930 nm, donde la detección óptica es mucho más eficiente.

Por lo tanto, para demostrar el potencial de nanohilos en dispositivos

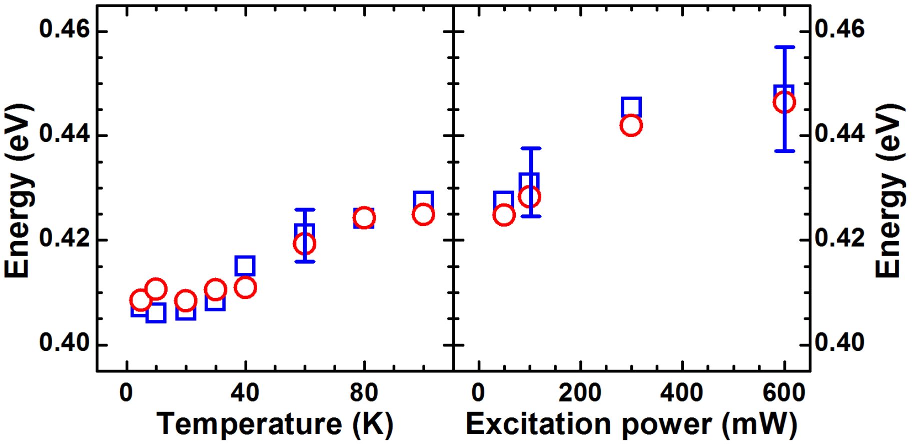

***Figure 3.:*** (a) Energías de PL de la banda de alta energía (HEB) de la muestra A (cuadrados) y B (círculos) en función de temperatura. (b) Energías de la banda de PL en 100 K en función de la potencia de excitación.

optoelectrónicos se han utilizado nanohilos core/shell de GaAs/AlGaAs para el transporte acústico de portadores fotoexcitados a lo largo del eje del nanohilo.

El transporte acústico ha sido realizado por las SAWs. Estas ondas, también conocidas como *ondas elásticas superficiales*, fueron explicadas por Lord Rayleigh en 1885 [66]. Un tipo particular de estas SAWs es la llamada, en honor a su descubridor, *onda de Rayleigh* que se aplicó en este trabajo. Estas SAWs de Rayleigh están localizadas cerca de la superficie y consisten en la superposición de un modo acústico longitudinal polarizado paralelo a la dirección de propagación de la SAW y un modo transversal polarizado perpendicular a la superficie. Esto conduce a regiones alternas de deformación de tracción y compresión a lo largo de la dirección de propagación. Debido a la deformación y su correspondiente potencial piezoeléctrico, se impone una modulación dinámica de tipo-II de las bandas electrónicas que se utiliza para transportar portadores con la velocidad del sonido en estructuras de pozos cuánticos [67–69].

Estas SAWs se han aplicado a nanohilos core/shell de GaAs/AlGaAs, transferidos a un sustrato de $LiNbO_3$, con el fin de transportar portadores fotoexcitados a lo largo del eje del nanohilo a una segunda localización donde la recombinación lleva a la emisión remota de pulsos de luz de

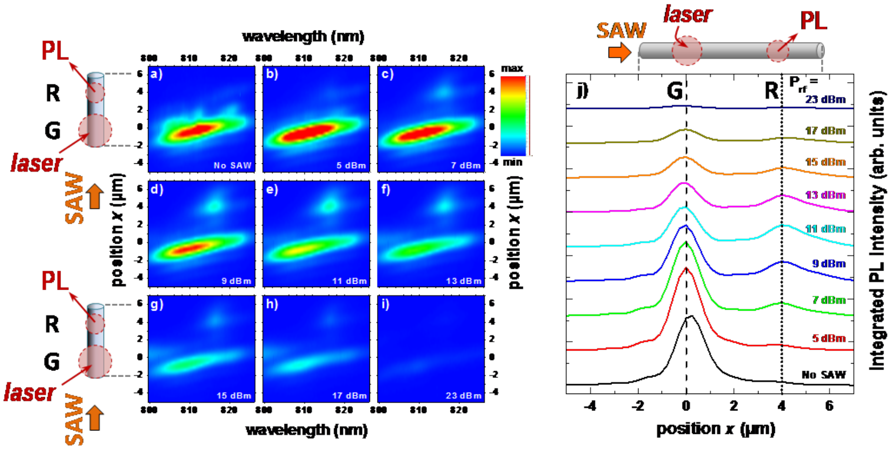

***Figure 4.:*** (a-i) Imágenes de PL de un nanohilo de GaAs excitado por un haz de láser estrictamente enfocado cerca del extremo inferior del nanohilo (véase la inserción de izquierda) para distintas amplitudes acústicas. Trasnporte acústico de portadores se puede observar para potencias acústicas moderadas. (j) Perfil integrado de PL a lo largo del eje del nanohilo de 813,9 nm a 819,1 nm para diferentes amplitudes acústicas con una radio-frecuencia fija de 226,5 Mhz.

sub-nanosegundos sincronizados con la fase de la SAW.

Los resultados del transporte acústico de portadores en nanohilos de GaAs y sus características de recombinación han demostrado que, bajo el campo piezoeléctrico de alta frecuencia de la SAW, electrones y huecos fotoexcitados pueden ser transferidos a lo largo del eje de un nanohilo [véase fig. 4(a-i)]. La dinámica del transporte ha sido estudiada por espectroscopia TRPL. Los resultados obtenidos revelan que los pulsos de recombinación en la posición remota tienen una anchura de sub-nanosegundos y están sincronizados con la fase de la SAW. Con el fin de investigar el comportamiento de recombinación, se han realizado experimentos de PL polarizada. Los resultados en conjunto sugieren que hay dos tipos de pulsos de recombinación que ocurren en posiciones diferentes de los nanohilos. Los pulsos $h \to e$ son emitidos desde la región de la fase zincblenda en R donde los electrones ($e$) quedan atrapados y se recombinan con los huecos ($h$) transferidos después de un ciclo medio de la SAW. Esto es coherente con la emisión observada polarizada paralela

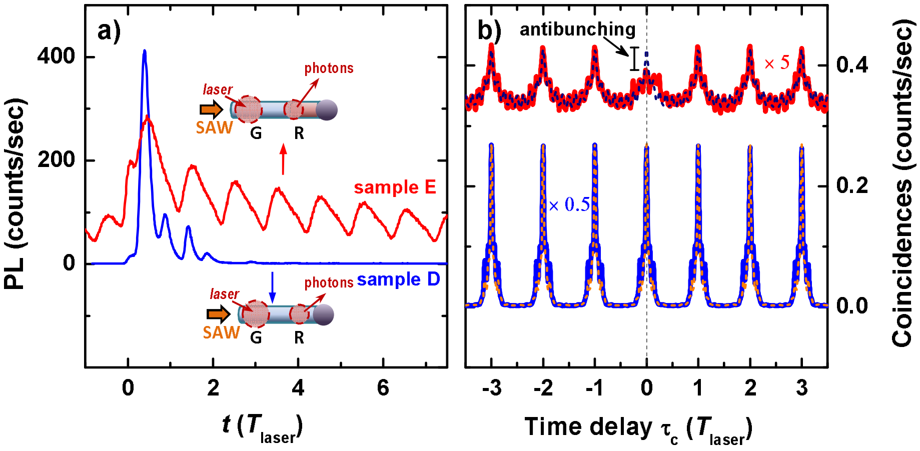

***Figure 5.:*** (a) PL resuelta en tiempo en la posición remoto (R) de un nanohilo de GaAs (curva azul, muestra D) y un nanohilo de (In,Ga)As/GaAs (curva roja, muestra E). Portadores fotoexcitados en G están acústicamente transferidos a R donde recombinan. (b) Medidas de autocorrelación de la muestra D (línea continua azul) y de la muestra E (línea continua roja) y las correspondientes autocorrelaciones numéricas (líneas discontinuas) de los espectros con resolución temporal en (a). Para las medidas se han utilizado las frecuencias acústicas de $f_{\mathrm{SAW,D}} = 226.8\,\mathrm{MHz}$ y $f_{\mathrm{SAW,E}} = 338.4\,\mathrm{MHz}$ con amplitudes de $P_{\mathrm{rf,D}} = 8\,\mathrm{dBm}$ y $P_{\mathrm{rf,E}} = 15\,\mathrm{dBm}$ para la muestra D y E, respectivamente.

al eje del nanohilo, como se esperaba para nanohilos de zincblenda. El pulso $e \rightarrow h$ se atribuye a la recombinación de los huecos atrapados en secciones alternativas de wurtzita/zincblenda. Debido a la alineación de banda de tipo-II los huecos pueden ser atrapados en las secciones pequeñas de wurtzita incluidas en fases de zincblenda. La recombinación de estos huecos con electrones transferidos lleva a pulsos de PL que son similares en energía a los pulsos de $h \rightarrow e$, debido a los efectos de confinamiento cuántico en las secciones de wurtzita. No se pudo observar estos pulsos en las medidas de PL polarizada, lo cual puede estar asociado a la falta de secciones alternativas de wurtzita/zincblenda o la falta de estados confinados. Este último conduce a la recombinación de los huecos de la banda de valencia en la fase wurtzita y los electrones de la banda de conducción en la zincblenda que tienen las energías de emisión más bajas que el rango detectado de longitudes de onda en estos experimentos. Las medidas de de PL polarizada de espín han sugerido que no se ha podido realizar un exceso de espines debido a la anisotropía de polarización de los nanohilos.

La manipulación de alta frecuencia sin contacto de los portadores por la SAW abre nuevas perspectivas para las aplicaciones de nanohilos de dispositivos optoelectrónicos que operan en las frecuencias de GHz. El potencial de este enfoque se demuestra en la realización de una fuente de alta frecuencia de fotones antibunched basados en el transporte acústico de electrones y huecos en nanohilos axiales de (In,Ga)As/GaAs con AlGaAs shell. Los resultados de PL han revelado que, en comparación con los nanohilos de GaAs, el crecimiento de un segmento (In,Ga)As en la parte superior de los nanohilos conduce a otras líneas de emisión que van desde la 800 nm a 930 nm. Experimentos de TRPL han demostrado que portadores que fueron acústicamente transferidos pueden ser atrapados en este segmento insertado. Sin embargo, los métodos de captura son eficaces solamente para un tipo de portadores. Debido a la alineación de banda de tipo-I entre GaAs y (In,Ga)As y la mayor diferencia del offset de la banda de conducción, en comparación con la de las bandas de valencia, la captura en el segmento de (In,Ga)As es más eficiente para los electrones que para los huecos. Las medidas de autocorrelación de fotones en nanohilos de (In,Ga)As/GaAs han demostrado la realización de una fuente de fotones antibunched (véase fig. 5). La detección de fotones antibunched se ha relacionado con la presencia del segmento de (In,Ga)As. Las líneas adicionales de emisión provenientes del (In,Ga)As segmento se extienden sobre un amplio espectro con algunas líneas de emisión bien separadas de las demás. Esto proporciona la posibilidad de filtrar una línea de emisión espectralmente. Lo cual se ha utilizado para los experimentos de autocorrelación. La separación espectral y espacial del centro de emisión se reduce la cantidad de centros cuánticos de emisión que contribuyen a la señal y se cree que desempeñan un papel clave para la observación de antibunching de fotones.

# List of publications and presentations

## Publications related to this thesis:

(i) M. Möller, L. C. O. Dacal, M. M. de Lima, Jr., T. Chiaramonte, M. A. Cotta, F. Iikawa and A. Cantarero, $E_1$ Gap of Wurtzite InAs Single Nanowires Measured by Means of Resonant Raman Spectroscopy,
*AIP Conference Proceedings* **1399** (2011) 473-474.

(ii) M. Möller, M. M. de Lima, Jr., A. Cantarero, L. C. O. Dacal, J. R. Madureira, F. Iikawa, T. Chiaramonte and M. A. Cotta, Polarized and Resonant Raman Spectroscopy on Single InAs Nanowires,
*Physical Review B* **84** (2011) 085318 [+ Erratum **85** (2012) 239904(E)].

(iii) A. Hernández-Mínguez, M. Möller, C. Pfüller, S. Breuer, O. Brandt, M. M. de Lima, Jr., A. García-Cristóbal, A. Cantarero, L. Geelhaar, H. Riechert, H. and P. V. Santos, Carrier Transport in GaAs Nanowires Using Surface Acoustic Waves,
*MRS Proceeding* **1408** (2012) BB10-42.

(iv) A. Hernández-Mínguez, M. Möller, S. Breuer, C. Pfüller, C. Somaschini, S. Lazić, O. Brandt, A. García-Cristóbal, M. M. de Lima, Jr., A. Cantarero, L. Geelhaar, H. Riechert, H. and P. V. Santos, Acoustically Driven Photon Antibunching in Nanowires,
*Nano Letters* **12** (2012) 252-258.

(v) M. Möller, A. Hernández-Mínguez, S. Breuer, C. Pfüller, O. Brandt, M. M. de Lima, Jr., A. Cantarero, L. Geelhaar, H. Riechert, H. and P. V. Santos, Polarized recombination of acoustically transported carriers in GaAs nanowires,
*Nanoscale Research Letters* **7** (2012) 247.

(vi) M. Möller, M. M. de Lima, Jr., A. Cantarero, T. Chiaramonte, M. A. Cotta and F. Iikawa, Optical emission of InAs nanowires,
Submitted to *Nanotechnology*

## Presentations related to this thesis: (* presenting author)

(a) M. MÖLLER*, M. M. DE LIMA, JR., A. CANTARERO, F. IIKAWA, T. CHIARAMONTE AND M. A. COTTA, Raman measurements on InAs single nanowires near the $E_1$ gap,
Poster presentation, *Prominas Workshop of the Convergence of the Conventional Microelectronics and Nanotechnology*, Grenoble (France), September 15-17, 2009.

(b) M. MÖLLER*, M. M. DE LIMA, JR., A. CANTARERO, L. C. O. DACAL, F. IIKAWA, T. CHIARAMONTE AND M. A. COTTA, Raman measurements on InAs single nanowires near the $E_1$1 gap,
Poster presentation, *VI Reunión del Grupo Especializado de Física del Estado Sólido (GEFES2010)*, Zaragoza (Spain), February 3-5, 2010.

(c) M. MÖLLER*, M. M. DE LIMA, JR., A. CANTARERO, L. C. O. DACAL, F. IIKAWA, T. CHIARAMONTE AND M. A. COTTA, $E_1$ gap of wurtzite InAs single nanowires measured by means of resonant Raman spectroscopy,
Poster presentation, *30th International Conference on the Physics of Semiconductors (ICPS2010)*, Seoul (South Corea), July 25-30, 2010.

(d) M. MÖLLER, M. M. DE LIMA, JR., A. CANTARERO, L. C. O. DACAL, F. IIKAWA, T. CHIARAMONTE, M. A. COTTA AND J. R. MADUREIRA*, Polarized and resonant Raman scattering on single InAs nanowires,
Poster presentation, *15th Brazilian Workshop on Semiconductor Physics (BWSP-15*, Juiz de Fora, Minas Gerais (Brazil), April 10-15, 2011.

(e) M. MÖLLER*, M. M. DE LIMA, JR., A. CANTARERO, L. C. O. DACAL, F. IIKAWA, T. CHIARAMONTE AND M. A. COTTA, Excitonic recombination in wurtzite InAs nanowires,
Poster presentation, *Optics of Excitons in Confined Systems (OECS12)*, Paris (France), September 12-16, 2011.

(f) A. HERNÁNDEZ-MÍNGUEZ*, M. MÖLLER, S. BREUER, C. SOMASCHINI, S. LAZIĆ, C. PFÜLLER, O. BRANDT, A. GARCÍA-CRISTÓBAL,

M. M. de Lima, Jr., A. Cantarero, L. Geelhaar, H. Riechert, P. V. Santos, Acoustic charge transport in GaAs nanowires,
Poster presentation, *PDI Topical Workshop on MBE-grown Arsenide Nanowires*, Paul-Drude-Institut für Festkörperelektronik, Berlin (Germany), September 8-9, 2011.

(g) M. Möller*, A. Hernández-Mínguez, S. Breuer, C. Pfüller, O. Brandt, M. M. de Lima, Jr., A. Cantarero, L. Geelhaar, H. Riechert, P. V. Santos, Polarized recombination of acoustically transported charge carriers in GaAs nanowires,
Oral presentation, *Trends in Nanotechnology*, Tenerife (Spain), November 21-25, 2011.

(h) A. Hernández-Mínguez, M. Möller, C. Pfüller, S. Breuer, O. Brandt, A. García-Cristóbal, M. M. de Lima, Jr., A. Cantarero, L. Geelhaar, H. Riechert, P. V. Santos*, Carrier Transport in GaAs Nanowires Using Surface Acoustic Waves,
Poster presentation, *MRS Fall Meeting*, Boston (USA), November 28 - December 2, 2011.

(i) M. Möller, M. M. de Lima, Jr., A. Cantarero*, T. Chiaramonte, M. A. Cotta and F. Iikawa, Optical properties of wurtzite InAs nanowires,
Poster presentation, *VII Reunión del Grupo Especializado de Física del Estado Sólido (GEFES2012)*, Sevilla (Spain), January 25-27, 2012.

(j) M. Möller, M. M. de Lima, Jr.*, A. Cantarero, T. Chiaramonte, M. A. Cotta and F. Iikawa, Optical properties of wurtzite InAs nanowires,
Oral presentation, *Nanospain 2012*, Santander (Spain), February 25-27, 2012.

(k) M. Möller*, M. M. de Lima, Jr., A. Cantarero, T. Chiaramonte, M. A. Cotta and F. Iikawa, Optical properties of wurtzite InAs nanowires,
Oral presentation, *31th International Conference on the Physics of Semiconductors (ICPS2012)*, Zurich (Switzerland), July 29 – August 3, 2012.

Further publications (not related to this thesis):

(I) M. Klevenz, S. Wetzel, M. Möller and A. Pucci, Evaporation and Condensation of SiO and SiO2 studied by Infrared Spectroscopy,
*Applied Spectroscopy* **64** (2010) 298-303.

Further presentations (not related to this thesis):

(A) M. Klevenz*, M. Möller and A. Pucci, Evaporation, condensation and annealing processes of silicate materials studied by IR spectroscopy,
Poster presentation, *5th Planet Formation Workshop*, Braunschweig (Germany), September 19-21, 2007.

(B) M. Möller*, M. Klevenz and A. Pucci, Infrared spectroscopical studies of the evaporation, condensation and annealing process of $SiO_2$,
Poster presentation, *Annual conference of the Deutsche Physikalische Gesellschaft*, Berlin (Germany), February 25-29, 2008.

(C) M. Klevenz*, M. Möller, D. Lattard, M. Trieloff and A. Pucci, Evaporation, condensation and annealing of silicates studied by IR spectroscopy,
Poster presentation, *Annual conference of the Deutsche Physikalische Gesellschaft*, Berlin (Germany), February 25-29, 2008.

(D) S. Wetzel*, M. Klevenz, M. Möller, D. Lattard, M. Trieloff and A. Pucci, Condensation of silicon monoxide studied by infrared spectroscopy,
Poster presentation, *Cosmic Dust Near & Far*, Heidelberg (Germany), September 8-12, 2008.

(E) M. Klevenz*, S. Wetzel, M. Möller, D. Lattard, M. Trieloff and A. Pucci, Evaporation studies on silicates,
Poster presentation, *Cosmic Dust Near & Far*, Heidelberg (Germany), September 8-12, 2008.

(F) S. Wetzel*, M. Klevenz, M. Möller, M. Trieloff and A. Pucci, Condensation of SiO and SiO2 studied by infrared spectroscopy,
Poster presentation, *Planet Formation and Evolution: The Solar System and Extrasolar Planets*, Tübingen (Germany), March 2-6, 2009.

(G) M. Klevenz*, S. Wetzel, M. Möller, M. Trieloff, H.-P. Gail and A. Pucci, Evaporation studies on silicates - First results on SiO vapour pressure,
Poster presentation, *Planet Formation and Evolution: The Solar System and Extrasolar Planets*, Tübingen (Germany), March 2-6, 2009.

# Bibliography

[1] H. J. Joyce, Q. Gao, H. H. Tan, C. Jagadish, Y. Kim, J. Zou, L. M. Smith, H. E. Jackson, J. Yarrison-Rice, P. Parkinson, and M. B. Johnston. III-V semiconductor nanowires for optoelectronic device applications. *Prog. Quant. Electron.*, 35:23–75, 2011.

[2] Kimberly A. Dick. A review of nanowire growth promoted by alloys and non-alloying elements with emphasis on Au-assisted III-V nanowires. *Prog. Cryst. Growth Charact. Mater.*, 54:138–173, 2008.

[3] C. Soci, A. Zhang, B. Xiang, D. P. R. Dayeh, S. A. Aplin, J. Park, X. Y. Bao, Y. H. Lo, and D. Wang. ZnO nanowire UV photodetectors with high internal gain. *Nano Lett.*, 7:1003–1009, 2007.

[4] R. Calarco, M. Marso, T. Richter, A. I. Aykanat, R. Meijers, A. v.d. Hart, T. Stoica, and H. Lüth. Size-dependent photoconductivity in MBE-grown GaN-nanowires. *Nano Lett.*, 5:981–984, 2005.

[5] Y. Cui, Z. Zhong, D. Wang, W. U. Wang, and C. M. Lieber. High performance silicon nanowire field effect transistors. *Nano Lett.*, 3:149–152, 2003.

[6] Jie Xiang, Wei Lu, Yongjie Hu, Yue Wu, Hao Yan, and Charles M. Lieber. Ge/Si nanowire heterostructures as high-performance field-effect transistors. *Nature*, 441:489–493, 2006.

[7] F. Patolsky, G. Zheng, O. Hayden, M. Lakadamyali, X. Zhuang, and C. M. Lieber. Electrical detection of single viruses. *Proc. Natl. Acad. Sci. USA*, 101:14017–14022, 2004.

[8] Y. Cui, Q. Wei, H. Park, and C. M. Lieber. Nanowire nanosensor for highly sensitive and selective detection of biological and chemical species. *Science*, 293:12891292, 2001.

[9] J. Du, D. Liang, H. Tang, and X. P. A. Gao. InAs nanowire transistors as gas senssor and the response mechanism. *Nano Lett.*, 9:4348–4351, 2009.

[10] Xianfeng Duan, Yu Huang, Yi Cui, Jianfeng Wang, and Charles M. Lieber. Indium phosphide nanowires as building blocks for nanoscale electronic and optoelectronic devices. *Nature*, 409:66–69, 2001.

[11] M. S. Gudiksen, L. J. Lauhon, J. Wang, D. C. Smith, and C. M. Lieber. Growth of nanowire superlattice structures for nanoscale photonics and electronics. *Nature*, 415:617–620, 2002.

[12] Xianfeng Duan, Yu Huang, Ritesh Agarwal, and Charles M. Lieber. Single-nanowire electrically driven laser. *Nature*, 421:241–245, 2003.

[13] L. Cao, J. S. White, J.-S. Park, J. A. Schuller, B. M. Clemens, and M. L. Brongersma. Engineering light absorption in semiconductor nanowire devices. *Nat. Mater.*, 8:643–647, 2009.

[14] E. C Garnett, M. L. Brongersma, Y. Cui, and M. D. McGehee. Nanowire solar cells. *Annu. Rev. Mater. Res.*, 41:269–295, 2011.

[15] Y. Huang, X. Duan, Y. Cui, L. J. Lauhon, K.-H. Kim, and C. M. Lieber. Logic gates and computation from assembled nanowire building blocks. *Science*, 294:1313–1317, 2001.

[16] R. Yan, D. Gargas, and P. Yang. Nanowire photonics. *Nat. Photonics*, 3:569–576, 2009.

[17] C. M. Lieber. Nanoscale science and technology: Building a big future from small things. *MRS Bulletin*, 28:486–491, 2003.

[18] M. S. Gudiksen, J. Wang, and C. M. Lieber. Size-dependent photoluminescence from single indium phosphide nanowires. *J. Phys. Chem. B*, 106:4036–4039, 2002.

[19] G. Zhang, K. Tateno, H. Sanada, T. Tawara, H. Gotoh, and H. Nakano. Synthesis of GaAs nanowires with very small diameters and their optical properties with the radial quantum-confinement effect. *Appl. Phys. Lett.*, 95:123104, 2009.

[20] K. Trivedi, H. Yuk, H. C. Floresca, M. J. Kim, and W. Hu. Quantum confinement induced performance in sub-5-nm lighographic Si nanowire transistors. *Nano Lett.*, 11:1412–1417, 2011.

[21] K. S. Yi, K. Trivedi, H. C. Floresca, W. Yuk, H. Hu, and M. J. Kim. Room-temperature quantum confinement effects in transport properties of ultrthin Si nanowire field-effect transistors. *Nano Lett.*, 11:5465–5470, 2011.

[22] H. E. Ruda and A. Shik. Polarization-sensitive optical phenomena in semiconducting and metallic nanowires. *Phys. Rev. B*, 72:115308, 2005.

[23] A. Paul, M. Luisier, and G. Klimeck. Influence of cross-section geometry and wire orientation on the phonon shifts in ultra-scaled Si nanowires. *J. Appl. Phys.*, 110:094308, 2011.

[24] K. W. Adu, Q. Xiong, H. R. Gutierrez, G. Chen, and P. C. Eklund. Raman scattering as a probe of phonon confinement and surface optical modes in semiconducting nanowires. *Appl. Phys. A*, 85:287–297, 2006.

[25] T. Kuykendall, P. Ulrich, S. Aloni, and P. Yang. Complete composition tunability of InGaN nanowires using a combinatorial approach. *Nat. Mater.*, 6:951–956, 2007.

[26] L. V. Titova, T. B. Hoang, H. E. Jackson, L. M. Smith, J. Yarrison-Rice, Y. Kim, H. J. Joyce, H. H. Tan, and C. Jagadish. Temperature dependence of photoluminescence from single core-shell GaAs-AlGaAs nanowires. *Appl. Phys. Lett.*, 89:173126, 2006.

[27] H.J. Joyce, Y. Kim, Q. Gao, H.H. Tan, and C. Jagadish. Growth, structural and optical properties of gaas/algaas core/shell nanowires with and without quantum well shells. In *Nanoscience and Nanotechnology, 2006. ICONN '06. International Conference on*, july 2006.

[28] Z. Gu, P. Prete, N. Lovergine, and B. Nabet. On optical properties of GaAs and GaAs/AlGaAs core-shell periodic nanowire arrays. *J. Appl. Phys.*, 109:064314, 2011.

[29] X. Jiang, Q. Xiong, S. Nam, F. Qian, Y. Li, and C. M. Lieber. InAs/InP radial nanowire heterostructures as high electron mobility devices. *Nano Lett.*, 7:3214–3218, 2007.

[30] W. Lu, J. Xiang, B. P. Timko, Y. Wu, and C. M. Lieber. One-dimensional hole gas in germanium/silicon nanowire heterostructures. *Proc. Natl. Acad. Sci. USA*, 102:10046–10051, 2005.

[31] F. Qian, S. Gradečak, Y. Li, C.-Y. Wen, and C. M. Lieber. Core/multishell nanowire heterostructures as multicolor, high efficiency light-emitting diodes. *Nano Lett.*, 5:2287–2291, 2005.

[32] F. Qian, Y. Li, S. Gradečak, H.-G. Park, Y. Dong, Y. Ding, L.-W. Wang, and C. M. Lieber. Multi-quantum-well nanowire heterostructures for wavelength-controlled lasers. *Nat. Mater.*, 7:701–706, 2008.

[33] K. A. Dick, S. Kodambaka, M. C. Reuter, K. Deppert, L. Samuelson, W. Seifert, L. R. Wallenberg, and F. M. Ross. The morphology of axial and branched nanowire heterostructures. *Nano Lett.*, 7:1817–1822, 2007.

[34] M. E. Messing, J. Wong-Leung, Z. Zanolli, H. J. Joyce, H. H. Tan, Q. Gao, L. R. Wallenberg, J. Johansson, and C. Jagadish. Growth of straight inas-on-gaas nanowire heterostructures. *Nano Lett.*, 11:3899–3905, 2011.

[35] C.-Y. Wen, M. C. Reuter, J. Bruley, J. Tersoff, S. Kodambaka, E. A. Stach, and F. M. Ross. Formation of compositionally abrupt axial heterojunctions in silicon-germanium nanowires. *Science*, 326:1247–1250, 2009.

[36] Y. N. Guo, J. Zou, M. Paladugu, H. Wang, Q. Gao, H. H. Tan, and C. Jagadish. Structural chraracteristics of GaSb/GaAs nanowire heterostructures grown by metal-organic chemical vapor deposition. *Appl. Phys. Lett.*, 89:231917, 2006.

[37] E. D. Minot, F. Kelkensberg, M. van Kouwen, J. A. van Dam, L. P. Kouwenhouven, V. Zwiller, M. T. Borgström, O. Wunnicke, M. A. Verheijen, and E. P. A. M. Bakkers. Single quantum dot nanowire leds. *Nano Lett.*, 7:367–371, 2007.

[38] J. Claudon, J. Bleuse, N. S. Malik, M. Bazin, P. Jaffrennou, N. Gregersen, C. Sauvan, P. Lalanne, and J.-M. Gérard. A highly efficient single-photon source based on a quantum dot in a photonic nanowire. *Nat. Photonics*, 4:174–177, 2010.

[39] J. Heinrich, A. Huggenberger, T. Heindel, S. Reitzenstein, S. Höfling, L. Worschech, and A. Forchel. Single photon emission from positioned GaAs/AlGaAs photonic nanowires. *Appl. Phys. Lett.*, 96:211117, 2010.

[40] M. E. Reimer, G. Bulgarini, N. Akopian, M. Hocevar, M. B. Bavinck, M. A. Verheijen, E. P. A. M. Bakkers, L. P. Kouwenhouven, and V. Zwiller. Bright single-photon sources in bottom-up tailored nanowires. *Nat. Commun.*, 3:737, 2012.

[41] M. Mattila, T. Hakkarainen, M. Mulot, and H. Lipsanen. Crystal-structure-dependent photoluminescence from InP nanowires. *Nanotechnol.*, 17:1580–1583, 2006.

[42] P. Mohan, J. Motohisa, and T. Fukui. Controlled growth of highly uniform, axial/radial direction-defined, individually addressable inp nanowire arrays. *Nanotechnol.*, 16:2903–2907, 2005.

[43] A. Mishra, L. V. Titova, T. B. Hoang, H. E. Jackson, L. M. Smith, J. M. Yarrison-Rice, Y. Kim, H. J. Joyce, Q. Gao, H. H. Tan, and C. Jagadish. Polarization and temperature dependence of photoluminescence from zincblende and wurtzite inp nanowires. *Appl. Phys. Lett.*, 91:263104, 2007.

[44] H. J. Joyce, J. Wong-Leung, Q. Gao, H. Hoe Tan, and C. Jagadish. Phase perfection in zinc blende and wurtzite III-V nanowires using basic growth parameters. *Nano Lett.*, 10:908–915, 2010.

[45] J. Bolinsson, P. Caroff, B. Mandl, and K. A. Dick. Wurtzite-zincblende superlattices in InAs nanowires using a supply interruption method. *Nanotechnol.*, 22:265606, 2011.

[46] G. Jacopin, L. Rigutti, L. Largeau, F. Fortuna, F. Furtmayr, F. H. Julien, M. Eickhoff, and M. Tchernycheva. Optical properties of wurtzite/zincblende heterostructures in GaN nanowires. *J. Appl. Phys.*, 110:064313, 2011.

[47] M. Murayama and T. Nakayama. Chemical trends of band offsets at wurtzite/zincblende heterocrystalline semiconductor interfaces. *Phys. Rev. B*, 49:4710–4725, 1994.

[48] Z. Zanolli, F. Fuchs, J. Furthmüller, U. von Barth, and F. Bechstedt. Model GW band structure of InAs and GaAs in the wurtzite phase. *Phys. Rev. B*, 75:245121, 2007.

[49] J.-M. Jancu, K. Gauthron, L. Largeau, G. Patriarche, J.-C. Harmand, and P. Voisin. Type II heterostructures formed by zinc-blende inclusions in InP and GaAs wurtzite nanowires. *Appl. Phys. Lett.*, 97:041910, 2010.

[50] T. B. Hoang, A. F. Moses, H. L. Zhou, D. L. Dheeraj, B. O. Fimland, and H. Weman. Observation of free exciton photoluminescence emission from single wurtzite GaAs nanowires. *Appl. Phys. Lett.*, 94:133105, 2009.

[51] T. B. Hoang, A. F. Moses, L. Ahtapodov, H. Zhou, D. L. Dheeraj, A. T. J. van Helvoort, B.-O. Fimland, and H. Weman. Engineering parallel and perpendicular polarized photoluminescence from a single semiconductor nanowire by crystal phase control. *Nano Lett.*, 10:2927–2933, 2010.

[52] S.-G. Ihn, M.-Y. Ryu, and J.-I. Song. Optical properties of undoped, Be-doped, and Si-doped wurtzite-rich GaAs nanowires grown on Si substrates by molecular beam epitaxy. *Solid State Comm.*, 115:729–733, 2010.

[53] U. Jahn, J. Lähnemann, C. Pfüller, O. Brandt, S. Breuer, B. Jenichen, M. Ramsteiner, L. Geelhaar, and H. Riechert. Luminescence of GaAs nanowires consisting of wurtzite and zinc-blende segments. *Phys. Rev. B*, 85:045323, 2012.

[54] A. De and Craig E. Pryor. Predicted band structures of III-V semiconductors in the wurtzite phase. *Phys. Rev. B*, 81:155210, 2010.

[55] M. Moewe, L. C. Chuang, S. Crankshaw, C. Chase, and C. Chang-Hasnain. Atomically sharp catalyst-free wurtzite GaAs/AlGaAs nanoneedles grown on silicon. *Appl. Phys. Lett.*, 93:023116, 2008.

[56] M. Heiss, S. Conesa-Boj, J. Ren, H.-H. Tseng, A. Gali, A. Rudolph, E. Uccelli, F. Peiró, J. R. Morante, D. Schuh, E. Reiger, E. Kaxiras, J. Arbiol, and A. Fontcuberta i Morral. Direct correlation of crystal structure and optical properties in wurtzite/zinc-blende GaAs nanowire heterostructures. *Phys. Rev. B*, 83:045303, 2011.

[57] B. Ketterer, M. Heiss, M. J. Livrozet, A. Rudolph, E. Reiger, and A. Fontcuberta i Morral. Determination of the band gap and the split-off band in wurtzite gaas using Raman and photoluminescence excitation spectroscopy. *Phys. Rev. B*, 83:125307, 2011.

[58] B. Ketterer, M. Heiss, E. Uccelli, J. Arbiol, and A. Fontcuberta i Morral. Untangling the electronic band structure of wurtzite GaAs nanowires by resonant Raman spectroscopy. *ACS Nano*, 5:7585–7592, 2011.

[59] J. Trägårdh, A. I. Persson, J. B. Wagner, D. Hessmann, and L. Samuelson. Measurement of the band gap of wurtzite $\mathrm{InAs}_{1-x}\mathrm{P}_x$ nanowires using photocurrent spectroscopy. *J. Appl. Phys.*, 101:123701, 2007.

[60] J. Bao, David C. Bell, F. Capasso, N. Erdman, D. Wei, L. Fröberg, T. Mårtensson, and L. Samuelson. Nanowire-induced wurtzite InAs thin film on zinc-blende InAs substrate. *Adv. Mater.*, 21:3654, 2009.

[61] N. G. Hörmann, I. Zardo, S. Hertenberger, S. Funk, S. Bolte, M. Döblinger, G. Koblmüller, and G. Abstreiter. Effects of stacking variations on the lattice dynamics of InAs nanowires. *Phys. Rev. B*, 84:155301, 2011.

[62] Sadao Adachi. *Properties of Group-IV, III-V and II-VI Semiconductors.* John Wiley & Sons, Ltd, Chichester, 2005.

[63] H. J. Joyce, Q. Gao, J. Wong-Leung, Y. Kim, H. H. Tan, and C. Jagadish. Tailoring GaAs, InAs, and InGaAs nanowires for optoelectronic device applications. *IEEE J. Sel. Top. Quant. Electr.*, 17:766–778, 2011.

[64] Katsuhiro Tomioka, Junichi Motohisa, Shinjiroh Hara, and Takashi Fukui. Control of InAs nanowire growth directions on Si. *Nano Lett.*, 8:3475–3480, 2008.

[65] G. Koblmüller, S. Hertenberger, K. Vizbaras, M. Bichler, F. Bao, J.-P. Zhang, and G. Abstreiter. Self-induced growth of vertical free-standing InAs nanowires on Si(111) by molecular beam epitaxy. *Nanotechnol.*, 21:365602, 2010.

[66] Lord Rayleigh. On waves propagated along the plane surface of an elastic solid. *Proc. London Math. Soc.*, s1-17:4–11, 1885.

[67] S. D. Gaalema, R. J. Schwartz, and R. L. Gunshor. Acoustic surface wave interaction charge-coupled device. *Appl. Phys. Lett.*, 29:82–83, 1976.

[68] M. J. Hoskins, H. Morkoç, and B. J. Hunsinger. Charge transport by surface acoustic waves in GaAs. *Appl. Phys. Lett.*, 41(4):332–334, 1982.

[69] W. J. Tanski, S. W. Merritt, R. N. Sacks, D. E. Cullen, E. J. Branciforte, R. D. Carroll, and T. C. Eschrich. Heterojunction acoustic charge transport devices on GaAs. *Appl. Phys. Lett.*, 52:18–20, 1988.

[70] Guozhong Cao and Dawei Liu. Template-based synthesis of nanorod, nanowire and nanotube arrays. *Adv. Colloid Interface Sci.*, 136:45–64, 2008.

[71] Margit Zacharias, Hong Jin Fan, and Peter Werner. Semiconductor nanowires: From self-organization to patterned growth. *Small*, 2:700–717, 2006.

[72] R. S. Wagner and W. C. Ellis. Vapor-liquid-solid mechanism of single crystal growth. *Appl. Phys. Lett.*, 4(5):89–90, 1964.

[73] C. J. Novotny and P. K. L. Yu. Vertically-aligned, catalyst-free InP nanowires grown by metalorganic chemical vapor deposition. *Appl. Phys. Lett.*, 87:203111, 2005.

[74] B. Mandl, J. Stangl, T. Mårtensson, A. Mikkelsen, J. Eriksson, L. S. Karlsson, G. Bauer, L. Samuelson, and W. Seifert. Au-free epitaxial growth of InAs nanowires. *Nano Lett.*, 6:1817–1821, 2006.

[75] T. Mårtensson, J. B. Wagner, E. Hilner, A. Mikkelsen, C. Thelander, J. Stangl, B. J. Ohlsson, A. Gustafsson, E. Lundgren, L. Samuelson, and W. Seifert. Epitaxial growth of indium arsenide nanowires on silicon using nucleation templates formed by self-assembled organic coatings. *Adv. Mater.*, 19:1801–1806, 2007.

[76] J. H. Paek, T. Nishiwaki, M. Yamaguchi, and N. Sawaki. Catalyst free MBE-VLS growth of GaAs nanowires on (111)Si substrate. *phys. stat. sol. (c)*, 6:1436–1440, 2009.

[77] S. Yu, G. Miao, Y. Jin, L. Zhang, H. Song, H. Jiang, Z. Li, D. Li, and X. Sun. Growth and optical properties of catalyst-free InP nanowires on Si (100) substrates. *Physica E*, in press, 2010.

[78] N. Wang, Y Cai, and R. Q. Zhang. Growth of nanowires. *Mater. Sci. Eng. R*, 60:1–51, 2008.

[79] Matt Law, Joshua Goldberger, and Peidong Yang. Semiconductor nanowires and nanotubes. *Annu. Rev. Mater. Res.*, 34:83–122, 2004.

[80] B. J. Ohlsson, M. T. Björk, M. H. Magnusson, K. Deppert, L. Samuelson, and L. R. Wallenberg. Size-, shape-, and position-controlled gaas nanowhiskers. *Appl. Phys. Lett.*, 79(20):3335–3337, 2001.

[81] Linus E. Jensen, Mikael T. Björk, Sören Jeppesen, Ann I. Persson, B. Jonas Ohlsson, and Lars Samuelson. Role of surface diffusion in chemical beam epitaxy of InAs nanowires. *Nano Lett.*, 4:1961–1964, 2004.

[82] Maria Tchernycheva, Laurent Travers, Gilles Patriarche, Frank Glas, Jean-Christophe Harmand, George E. Cirlin, and Vladimir G. Dubrovskii. Au-assisted molecular beam epitaxy of InAs nanowires: Growth and theoretical analysis. *J. Appl. Phys.*, 102:094313, 2007.

[83] H. D. Park, S. M. Prokes, and R. C. Cammarata. Growth of epitaxial InAs nanowires in a simple closed system. *Appl. Phys. Lett.*, 87:063110, 2005.

[84] Xianfeng Duan and Charles M. Lieber. General synthesis of compound semiconductor nanowires. *Adv. Mater.*, 12:298–302, 2000.

[85] Kimberly A. Dick, Knut Deppert, Lars Samuelson, and Werner Seifert. Optimization of Au-assisted InAs nanowires grown by MOVPE. *J. Cryst. Growth*, 297:326–333, 2006.

[86] Wei Lu and Charles M. Lieber. Semiconductor nanowires. *J. Phys. D: Appl. Phys.*, 39:R387–R406, 2006.

[87] Yiying Wu and Peidong Yang. Direct observation of vapour-liquid-solid nanowire growth. *J. Am. Chem. Soc.*, 123:3165, 2001.

[88] A. I. Persson, M. W. Larsson, S. Stenström, B. J. Ohlsson, L. Samuelson, and L. R. Wallenberg. Solid-phase diffusion mechanism fpr GaAs nanowire growth. *Nat. Mater.*, 3:677–681, 2004.

[89] Kurt W. Kolasinski. Catalytic growth of nanowires: Vapor-liquid-solid, vapor-solid-solid, solution-liquid-solid and solid-liquid-solid growth. *Curr. Opin. Solid State Mater. Sci.*, 10:182–191, 2006.

[90] Y. F. Zhang, Y. H. Tang, N. Wang, C. S. Lee, I. Bello, and S. T. Lee. One-dimensional growth mechanism of crystalline silicon nanowires. *J. Cryst. Growth*, 197:136–140, 1999.

[91] Rui-Qin Zhang, Yeshayahu Lifshitz, and Shuit-Tong Lee. Oxide-assisted growth of semiconducting nanowires. *Adv. Mater.*, 15:635–640, 2003.

[92] W. S. Shi, Y. F. Zheng, N. Wang, C. S. Lee, and S. T. Lee. Oxide-assisted growth and optical characterization of gallium-arsenide nanowires. *Appl. Phys. Lett.*, 78:3304–3306, 2001.

[93] Timothy J. Trentler, Kathleen M. Hickman, Subhash C. Goel, Ann M. Viano, Patrick C. Gibbons, and William E. Buhro. Solution-liquid-solid growth of crystalline III-V semiconductors: An analogy to vapor-liquid-solid growth. *Science*, 270:1791–1794, 1995.

[94] Fudong Wang, Angang Dong, Jianwei Sun, Rui Tang, Heng Yu, and William E. Buhro. Solution-liquid-solid growth of semiconductor nanowires. *Inorg. Chem.*, 45:7511–7521, 2006.

[95] Shadi A. Dayeh, Edward T. Yu, and Deli Wang. III-V nanowire growth mechanism: V/III ratio and temperature effects. *Nano Lett.*, 7:2486–2490, 2007.

[96] M. C. Plante and R. R. LaPierre. Control of GaAs nanowire morphology and crystal structure. *Nanotechnol.*, 19:495603, 2008.

[97] H. Shtrikman, R. Popovitz-Biro, A. Kretinin, L. Houben, M. Heiblum, M. Bukala, M. Galicka, R. Bucko, and P. Kacman. Method for suppression of stacking faults in wurtzite III-V nanowires. *Nano Lett.*, 9(4):1506–1510, 2009.

[98] Kimberly A. Dick, Knut Deppert, Lars Samuelson, and Werner Seifert. InAs nanowires grown by MOVPE. *J. Cryst. Growth*, 298:631–634, 2007.

[99] L. H. G. Tizei, T. Chiaramonte, D. Ugarte, and M. A. Cotta. III-V semiconductor nanowire growth: Does arsenic diffuse through the metal nanoparticle catalyst? *Nanotechnol.*, 20:275604, 2009.

[100] L. E. Fröberg, B. A. Wacaser, J. B. Wagner, S. Jeppesen, B. J. Ohlsson, K. Deppert, and L. Samuelson. Transients in the formation of nanowire heterostructures. *Nano Lett.*, 8(11):3815–3818, 2008.

[101] M. T. Björk, B. J. Ohlsson, T. Sass, A. I. Persson, C. Thelander, M. H. Magnusson, K. Deppert, L. R. Wallenberg, and L. Samuelson. One-dimensional steeplechase for electrons realized. *Nano Lett.*, 2(2):87–89, 2002.

[102] D. Kriegner, C. Panse, B. Mandl, K. A. Dick, M. Keplinger, J. M. Persson, P. Caroff, D. Ercolani, L. Sorba, F. Brechstedt, J. Stangl, and G. Bauer. Unit cell structure of crystal polytypes in InAs and InSb nanowires. *Nano Lett.*, 11:1483–1489, 2011.

[103] Jonas Johansson, Lisa S. Karlsson, Kimberly A. Dick, Jessica Bolinsson, Brent A. Wacaser, Knut Deppert, and Lars Samuelson. Effects of supersaturation on the crystal structure of gold seeded III-V nanowires. *Cryst. Growth Des.*, 9:766–773, 2009.

[104] H. Shtrikman, R. Popovitz-Biro, A. Kretinin, and M. Heiblum. Stacking-faults-free zinc blende GaAs nanowires. *Nano Lett.*, 9(1):215–219, 2009.

[105] F. Glas, J.-C. Harmand, and G. Patriarche. Why does wurtzite form in nanowires of III-V zinc blende semiconductors? *Phys. Rev. Lett.*, 99:146101, 2007.

[106] Shadi A. Dayeh, Cesare Soci, Xin-Yu Bao, and Deli Wang. Advances in the synthesis of InAs and GaAs nanowires for electronic applications. *Nano Today*, 4:347–358, 2009.

[107] S. Breuer, C. Pfüller, T. Flissikowski, O. Brandt, H. T. Grahn, L. Geelhaar, and H. Riechert. Suitability of Au- and self-assisted GaAs nanowires for optoelectronic applications. *Nano Lett.*, 11:1276, 2011.

[108] Peter Y. Yu and Manuel Cardona. *Fundamentals of Semiconductors.* Springer, 2010.

[109] Chihiro Hamaguchi. *Basic Semiconductor Physics.* Springer, 2001.

[110] Hans Kuzmany. *Solid-State Spectroscopy.* Springer Heidelberg Dordrecht London New York, 2009.

[111] M. Cardona and G. Güntherodt, editors. *Light Scattering in Solids II.* Springer, 1982.

[112] R. Loudon. The Raman effect in crystals. *Adv. Phys.*, 13(52):423–482, 1964.

[113] A. Fainstein, B. Jusserand, and V. Thierry-Mieg. Raman scattering enhancement by optical confinement in a semiconductor planar microcavity. *Phys. Rev. Lett.*, 75(20):3764–3767, 1995.

[114] S. Antoci, E. Reguzzoni, and G. Samoggia. Excitonic effects on the $E_1$ and $E_1 + \Delta_1$ transitions in InAs. *Phys. Rev. Lett.*, 24:1304–1307, 1970.

[115] M. Welkowsky and R. Braunstein. Interband transitions and excitonic effects in semiconductors. *Phys. Rev. B*, 5:497–509, 1972.

[116] J. L. Birman. Simplified LCAO method for zincblende, wurtzite and mixed crystal structures. *Phys. Rev.*, 115(6):1493–1505, 1959.

[117] J. Zi, X. Wan, G. Wei, K. Zhang, and X. Xie. Lattice dynamics of zinc-blende GaN and AlN: I. bulk phonons. *J. Phys.: Condens. Matter*, 8:6323–6328, 1996.

[118] T. C. Damen, S. P. S. Porto, and B. Tell. Raman effect in zinc oxide. *Phys. Rev.*, 142:570–574, 1966.

[119] N. S. Orlova. Variation of phonon dispersion curves with temperature in indium arsenide measured by X-Ray thermal diffuse scattering. *phys. stat. sol. (b)*, 119:541–546, 1983.

[120] R. Carles, N. Saint-Cricq, J. B. Renucci, M. A. Renucci, and A. Zwick. Second-order raman scattering in inas. *Phys. Rev. B*, 22(10):4804–4815, 1980.

[121] J. L. Birman. Some selection rules for band-band transitions in wurtzite structure. *Phys. Rev.*, 114(6):1490–1492, 1959.

[122] C. Rocke, S. Zimmermann, A. Wixforth, J. P. Kotthaus, G. Böhm, and G. Weimann. Acoustically driven storage of light in a quantum well. *Phys. Rev. Lett.*, 78:4099–4102, 1997.

[123] C. L. Foden, V. I. Talyanskii, G. J. Milburn, M. L. Leadbeater, and M. Pepper. High-frequency acousto-electric single-photon source. *Phys. Rev. A*, 62:011803(R), 2000.

[124] O. D. D. Couto, Jr., S. Lazić, F. Iikawa, J. A. H. Stotz, U. Jahn, R. Hey, and P. V. Santos. Photon anti-bunching in acoustically pumped quantum dots. *Nat. Photonics*, 3:645–648, 2009.

[125] R. Loudon. *The Quantum Theory of Light.* Oxford University Press, 2000.

[126] M. D. Eisaman, J. Fan, A. Migdall, and S. V. Polyakov. Invited review article: Single-photon sources and detectors. *Rev. Sci. Instrum.*, 82:071101, 2011.

[127] B. Lounis and M. Orrit. Single-photon sources. *Rep. Prog. Phys.*, 68:1129–1179, 2005.

[128] G. Grynberg, A. Aspect, and C. Fabre. *Introduction to Quantum Optics - From the Semi-classical Approach to Quantized Light.* Cambridge University Press, 2010.

[129] R. Hanbury Brown and R. Q. Twiss. Correlation between photons in two coherent beams of light. *Nature*, 177:27–32, 1956.

[130] M. Cardona, editor. *Light Scattering in Solids I.* Springer, 1983.

[131] P. Blaha, K. Schwarz, K. H. Madsen, D. Kvasnicka, and J. Luitz. *WIEN2k, An Augmented Plane Wave + Local Orbitals Program for Calculating Crystal Properties.* Techn. Universität Wien, Austria, 2001.

[132] Fabien Tran and Peter Blaha. Accurate band gaps of semiconductors and insulators with a semilocal exchange-correlation potential. *Phys. Rev. Lett.*, 102(22):226401, Jun 2009.

[133] R. C. C. Leite and J. F. Scott. Resonant surface Raman scattering in direct-gap semiconductors. *Phys. Rev. Lett.*, 22(4):130–132, 1969.

[134] M. A. Renucci, J. B. Renucci, and M. Cardona. Resonance Raman scattering in III-V semiconductors and their alloys. *phys. stat. sol. (b)*, 49:625–631, 1972.

[135] R. Carles, N. Saint-Cricq, J. B. Renucci, A. Zwick, and M. A. Renucci. Resonance raman scattering in inas near the $E_1$ edge. *Phys. Rev. B*, 22(12):6120–6126, 1980.

[136] T. Angelova, A. Cros, A. Cantarero, D. Fuster, Y. González, and L. González. Raman study of self-assembled InAs/InP quantum wire stacks with varying spacer thickness. *J. Appl. Phys.*, 104:033523, 2008.

[137] M. M. Martin. Theory of the one-photon resonance Raman effect. *Phys. Rev. B*, 4:3676–3685, 1971.

[138] R. M. Martin and T. C. Damen. Breakdown of selection rules in resonance Raman scattering. *Phys. Rev. Lett.*, 26(2):86–88, 1971.

[139] I. Zardo, S. Conesa-Boj, F. Peiro, J. R. Morante, J. Arbiol, E. Uccelli, G. Abstreiter, and A. Fontcuberta i Morral. Raman spectroscopy of wurtzite and zinc-blende GaAs nanowires: Polarization dependence, selection rules, and strain effects. *Phys. Rev. B*, 80:245314, 2009.

[140] Otfried Madelung, editor. *Semiconductors - Basic Data.* Springer, 1996.

[141] S. Ushioda, A. Aziza, J. B. Valdez, and G. Mattei. Effects of surface roughness on surface polaritons. *Phys. Rev. B*, 19:4012–4019, 1979.

[142] S. Hayashi and H. Kanamori. Raman scattering from surface phonon mode in GaP microcystals. *Phys. Rev. B*, 26:7079–7082, 1982.

[143] D. Spirkoska, G. Abstreiter, and Font. Size and environment dependence of surface phonon modes of gallium arsenide nanowires as measured by Raman spectroscopy. *Nanotechnol.*, 19:435704, 2008.

[144] Rajeev Gupta, Q. Xiong, G. D. Mahan, and P. C. Eklund. Surface optical phonons in gallium phosphide nanowires. *Nano Lett.*, 3:1745–1750, 2003.

[145] N. Begum, A. S. Bhatti, F. Jabeen, S. Rubini, and F. Martelli. Lineshape analysis of Raman scattering from LO and SO phonons in III-V nanowires. *J. Appl. Phys.*, 106:114317, 2009.

[146] M. Cantoro, A. V. Klekachev, A. Nourbakhsh, B. Sorée, M. M. Heyns, and S. De Gendt. Long-wavelength, confined optical phonons in InAs nanowires probed by Raman spectroscopy. *Eur. Phys. J. B*, 79:423–428, 2011.

[147] Concetta Nobile, Vladimir. A. Fonoberov, Stefan Kudera, Antonio Della Torre, Antonio Ruffino, Gerwin Chilla, Tobias Kipp, Detlef Heitmann, Liberato Manna, Roberto Cingolani, Alexander A. Baladin, and Roman Krahne. Confined optical phonon modes in aligned nanorod arrays detected by resonant inelastic light scattering. *Nano Lett.*, 7:476479, 2007.

[148] Shanna Crankshaw, Linus C. Chuang, Michael Moewe, and Connie Chang-Hasnain. Polarized zone-center phonon modes of wurtzite GaAs. *Phys. Rev. B*, 81:233303, 2010.

[149] Q. Xiong, G. Chen, H. R. Gutierrez, and P. C. Eklund. Raman scattering studies of individual polar semiconducting nanowires: Phonon splitting and antenna effects. *Appl. Phys. A*, 85:299–305, 2006.

[150] L. Ö. Olsson, C. B. M. Anderson, M. C. Håkansson, J. Kanski, L. Ilver, and U. O. Karlsson. Charge accumulation at InAs surfaces. *Phys. Rev. Lett.*, 76:3626–3629, 1996.

[151] C. Affentauschegg and H. H. Wieder. Properties of InAs/InAlAs heterostructures. *Semicond. Sci. Technol.*, 16:708–714, 2001.

[152] S. Buchner and E. Burstein. Raman scattering by wave-vector-dependent LO-phonon-plasmon modes in $n$-InAs. *Phys. Rev. Lett.*, 33:908–911, 1974.

[153] Y. Chen, J. C. Hermanson, and G. J. Lapeyre. Coupled plasmon and phonon in the accumulation layer of InAs(110) cleaved surfaces. *Phys. Rev. B*, 39:12682–12687, 1989.

[154] X. X. Xu, K. H. Yu, W. Wei, B. Peng, S. H. Huang, Z. H. Chen, and X. S. Shen. Raman scattering in InAs nanowires synthesized by a solvothermal route. *Appl. Phys. Lett.*, 89:253117, 2006.

[155] M. H. Sun, E. S. P. Leong, A. H. Chin, C. Z. Ning, G. E. Cirlin, Y. B. Samsonenko, V. G. Dubrovskii, L. Chuang, and C. Chang-Hasnain. Photoluminescence properties of InAs nanowires grown on GaAs and Si substrates. *Nanotechnol.*, 21:335705, 2010.

[156] Z. M. Fang, K. Y. Ma, D. H. Jaw, R. M. Cohen, and G. B. Stringfellow. Photoluminescence of InSb, InAs and InAsSb grown by organometallic vapor phase epitaxy. *J. Appl. Phys.*, 67:7034–7039, 1990.

[157] T. Schmidt, K. Lischka, and W. Zulehner. Excitation power dependence of the near-band-edge photoluminescence of semiconductors. *Phys. Rev. B*, 45:8989–8994, 1992.

[158] P. J. P. Tang, C. C. Phillips, and R. A. Stradling. Excitonic photoluminescence in high-purity InAs MBE epilayers on GaAs substrates. *Semi*, 8:2135–2142, 1993.

[159] C. Thelander, K. A. Dick, M. T. Borgström, L. Fröberg, P. Caroff, H. A. Nilsson, and L. Samuelson. The electrical and structural properties of n-type InAs nanowires grown from metal-organic precursors. *Nanotechnol.*, 21:205703, 2010.

[160] J. Bao, D. C. Bell, F. Capasso, J. B. Wagner, T. Mårtensson, J. Trägårdh, and L. Samuelson. Optical properties of rotationally twinned InP nanowire heterostructures. *Nano Lett.*, 8:836–841, 2008.

[161] K. Pemasiri, M. Montazeri, R. Gass, L. M. Smith, H. E. Jackson, J. Yarrison-Rice, S. Paiman, Q. Gao, H. H. Tan, C. Jagadish, X. Zhang, and J. Zou. Carrier dynamics and quantum confinement in type II zb-wz InP nanowire homostructures. *Nano Lett.*, 9:648–654, 2009.

[162] L. Zhang, J.-W. Luo, A. Zunger, N. Akopian, V. Zwiller, and J.-C. Harmand. Wide InP nanowires with wurtzite/zincblende superlattice segments are type-II whereas narrower nanowires become type-I: An atomistic pseudopotential calculation. *Nano Lett.*, 10:4055, 2010.

[163] T. Akiyama, T. Yamashita, K. Nakamura, and T. Ito. Band alignment tuning in twin-plane superlattices of semiconductor nanowires. *Nano Lett.*, 10:4614–4618, 2010.

[164] J. Li and L.-W. Wang. Comparison between quantum confinement effects of quantum wires and dots. *Chem. Mater.*, 16:4012–4015, 2004.

[165] H. J. Joyce, H. H. Gao, Q. Tan, C. Jagadish, Y. Kim, M. A. Fickenscher, S. Perera, T. B. Hoang, L. M. Smith, H. E. Jackson, J. Yarrison-Rice, X. Zhang, and J. Zou. High purity GaAs nanowires free of planar defects: Growth and characterization. *Adv. Funct. Mater.*, 18:3794–3800, 2008.

[166] Y. P. Varshni. Temperature dependence of the energy gap in semiconductors. *Physica*, 34:149–154, 1967.

[167] J. M. Shilton, V. I. Talyanskii, M. Pepper, D. A. Ritchie, J. E. F. Frost, C. J. B. Ford, C. G. Smith, and G. A. C. Jones. High-frequency single-electron transport in a quasi-one-dimensional GaAs channel induced by surface acoustic waves. *J. Phys.: Condens. Matter*, 8:L531–L539, 1996.

[168] V. I. Talyanskii, J. M. Shilton, M. Pepper, C. G. Smith, C. J. B. Ford, E. H. Linfield, D. A. Ritchie, and G. A. C. Jones. Single-electron transport in a one-dimensional channel by high-frequency surface acoustic waves. *Phys. Rev. B*, 56:15180–15184, 1997.

[169] T. Sogawa, P. V. Santos, S. K. Zhang, S. Eshlaghi, A. D. Wieck, and K. H. Ploog. Transport and lifetime enhancement of photoexcited spins in GaAs by surface acoustic waves. *Phys. Rev. Lett.*, 87(27):276601, 2001.

[170] J. A. H. Stotz, R. Hey, P. V. Santos, and K. H. Ploog. Coherent spin transport through dynamic quantum dots. *Nat. Mater.*, 4:585–588, 2005.

[171] O. D. D. Couto, Jr., F. Iikawa, J. Rudolph, R. Hey, and P. V. Santos. Anisotropic spin transport in (110) GaAs quantum wells. *Phys. Rev. Lett.*, 98(3):036603, 2007.

[172] J. Ebbecke, C. J. Strobl, and A. Wixforth. Acoustoelectric current transport through single-walled carbon nanotubes. *Phys. Rev. B*, 70:233401, 2004.

[173] P. J. Leek, M. R. Buitelaar, V. I. Talyanskii, C. G. Smith, D. Anderson, G. A. C. Jones, J. Wei, and D. H. Cobden. Charge pumping in carbon nanotubes. *Phys. Rev. Lett.*, 95:256802, 2005.

[174] M. R. Buitelaar, V. Kashcheyevs, P. J. Leek, V. I. Talyanskii, C. G. Smith, D. Anderson, G. A. C. Jones, J. Wei, and D. H. Cobden. Adiabatic charge pumping in carbon nanotube quantum dots. *Phys. Rev. Lett.*, 101:126803, 2008.

[175] J. Ebbecke, S. Maisch, A. Wixforth, R. Calarco, R. Meijers, M. Marso, and H. Lüth. Acoustic charge transport in GaN nanowires. *Nanotechnol.*, 19:275708, 2008.

[176] J. B. Kinzel, D. Rudolph, M. Bichler, G. Abstreiter, J. J. Finley, G. Koblmüller, A. Wixforth, and H. J. Krenner. Directional and dynamic modulation of the optical emission of an individual GaAs nanowire using surface acoustic waves. *Nano Lett.*, 11:1512–1517, 2011.

[177] M. M. de Lima, Jr. and P. V. Santos. Modulation of photonic structures by surface acoustic waves. *Rep. Prog. Phys.*, 68:1639–1701, 2005.

[178] T. Sogawa, P. V. Santos, S. K. Zhang, S. Eshlaghi, A. D. Wieck, and K. H. Ploog. Dynamic band-structure modulation of quantum wells by surface acoustic waves. *Phys. Rev. B*, 63:121307, 2001.

[179] J. R. Gell, M. B. Ward, R. J. Young, R. M. Stevenson, D. Atkinson, G. A. C. Jones, D. A. Ritchie, and A. J. Shields. Modulation of single quantum dot energy levels by surface-acoustic-wave. *Appl. Phys. Lett.*, 93:081115, 2008.

[180] D. Spirkoska, J. Arbiol, A. Gustafsson, S. Conesa-Boj, F. Glas, I. Zardo, M. Heigoldt, M. H. Gass, Al. L. Bleloch, S. Estrade, M. Kaniber, J. Rossler, F. Peiro, J. R. Morante, G. Abstreiter, L. Samuelson, and A. Fontcuberta i Morral. Structural and optical properties of high quality zincblende/wurtzite GaAs nanowire heterostructures. *Phys. Rev. B*, 80:245325, 2009.

[181] D. Spirkoska, Al. L. Efros, W. R. L. Lambrecht, T. Cheiwchanchamnangij, A. Fontcuberta i Morral, and G. Abstreiter. Valence band structure of polytypic zinc-blende/wurtzite GaAs nanowires probed by polarization-dependent photoluminescence. *Phys. Rev. B*, 85:045309, 2012.

[182] P. Lautenschlager, M. Garriga, S. Logothetidis, and M. Cardona. Interband critical points of GaAs and their temperature dependence. *Phys. Rev. B*, 35:9174–9789, 1987.

[183] Steffen Breuer. private communications.

[184] T. B. Hoang, L. V. Titova, J. Yarrison-Rice, H. E. Jackson, A. O. Govorov, Y. Kim, H. J. Joyce, H. H. Tan, C. Jagadish, and L. M. Smith. Resonant excitation and imaging of nonequilibrium exciton spins in single core-shell GaAs-AlGaAs nanowires. *Nano Lett.*, 7:588–595, 2007.

[185] D. J. Arent, K. Deneffe, C. Van Hoof, J. De Boeck, and G. Borghs. Strain effects and band offsets in GaAs/InGaAs strained layered quantum structures. *J. Appl. Phys.*, 66:1739–1747, 1989.

[186] G. Arnaud, J. Allègre, P. Lefebvre, H. Mathieu, L. K. Howard, and D. J. Dunstan. Photoreflectance and piezophotoreflectance studies of strained-layer $\mathrm{In}_x\mathrm{Ga}_{1-x}\mathrm{As}$-GaAs quantum wells. *Phys. Rev. B*, 46:15290–15301, 1992.

[187] S. Paul, J. B. Roy, and P. K. Basu. Empirical evidence for the alloy composition and temperature dependence of the band gap and intrinsic carrier density in $\mathrm{Ga}_x\mathrm{In}_{1-x}\mathrm{As}$. *J. Appl. Phys.*, 69:827, 1991.

[188] J.-P. Reithmaier, R. Höger, H. Riechert, A. Heberle, G. Abstreiter, and G. Weimann. Band offset in elastically strained InGaAs/GaAs multiple quantum wells determined by optical absorption and electronic Raman scattering. *Appl. Phys. Lett.*, 56:536, 1990.

[189] J. Leymarie, C. Monier, A. Vasson, and A.-M. Vasson. Optical investigations in (In,Ga)As/GaAs quantum wells grown by metalorganic molecular-beam epitaxy. *Phys. Rev. B*, 51:13274–13280, 1995.

[190] I. Regolin, D. Sudfeld, S. Lüttjohann, V. Khorenko, W. Prost, J. Kästner, G. Dumpich, C. Meier, A. Lorke, and F.-J. Tegude. Growth and chracterisation of GaAs/InGaAs/GaAs nanowhiskers on (111)GaAs. *J. Cryst. Growth*, 298:607–611, 2007.

[191] M. Fukui, Y. Kobayashi, J. Motohisa, and T. Fukui. Spectroscopy and imaging of GaAs/InGaAs/GaAs nanowires grown by selective-area metalorganic vapor epitaxy. *phys. stat. sol. (c)*, 5:2743–2745, 2008.

[192] C. Wiele, F. Haake, C. Rocke, and A. Wixforth. Photon trains and lasing: The periodically pumped quantum dot. *Phys. Rev. A*, 58:R2680–R2683, 1998.

[193] P. Michler, A. Kiraz, C. Becher, W. V. Schoenfeld, P. M. Petroff, L. Zhang, E. Hu, and A. Imamoğlu. A quantum dot single-photon turnstile device. *Science*, 290:2282–2285, 2000.

[194] J. W. W. van Tilburg, R. E. Algra, W. G. G. Immink, M. Verheijen, E. P. A. M. Bakkers, and L. P. Kouwenhouven. Surface passivated InAs/InP core/shell nanowires. *Semicond. Sci. Technol.*, 25:024011, 2010.

[195] M. H. Sun, H. J. Joyce, Q. Gao, H. H. Tan, C. Jagadish, and C. Z. Ning. Removal of surface states and recovery of band-edge emission in InAs nanowires through surface passivation. *Nano Lett.*, 12, 2012.

[196] P. Hess. Surface acoustic waves in materials science. *Phys. Today*, 55:42–47, 2002.

[197] R. M. White. Surface elastic waves. *Proceed. IEEE*, 58:1238–81, 1970.

[198] A. J. de Vries, R. L. Miller, and T. J. Wojcik. Reflection of a surface wave from three types of id transducers. In J. De Klerf, editor, *1972 Ultrasonics Symposium*, pages 353–358. IEEE, New York, 1972.

[199] K. Yamanouchi and H. Furuyashaki. Low-loss SAW filter using internal reflection types of new single-phase unidirectional transducer. *IEEE Ultrasonic Symposium Proc.*, pages 68–71, 1984.

[200] K. Yamanouchi, C. H. S. Lee, K. Yamamoto, T. Meguro, and H. Odagawa. GHz-range low-loss wide band filters using new floating electride type unidirectional transducers. *IEEE Ultrasonic Symposium Proc.*, pages 139–142, 1992.

[201] A. García-Cristóbal, A. Cantarero, F. Alsina, and P. V. Santos. Spatiotemporal carrier dynamics in quatum wells under surface acoustic waves. *Phys. Rev. B*, 69:205301, 2004.

# Acknowledgements

Finally, I would like to thank all the people who accompanied and supported me during my PhD studies and the experts who evaluated this thesis.

In particular, I would like to thank Andrés for the opportunity to realize this PhD work in this research group and the support especially in issues concerning the bureaucratic jungle. Without him, this work would not have been possible. Special thanks I would like to give to Mauricio who always has been willing to help and support the work in the last four years which made the work very pleasant and fruitful. Besides the friendly character, I have got to know one of the walking libraries of Brazilian football history. The coffee breaks were one of the best moments of the day. Furthermore, I would like to thank Ana, Núria and Alberto for their helpfulness during all this time and Ana, in particular, for the arrangements in achieving the contract and the support in the first period of my PhD.

Many thanks to Fernando who initiated the project of the InAs nanowires and who gave me the possibility to pass one fantastic month in his group in Brazil, to Maria, Cheo, Emilio, Miguel, Milton,... who received me very friendly and made my stay brilliant. As well to Monica and Thalita who grow the InAs samples, supported and collaborated in this work.

Many thanks as well to Paulo who made the research in Berlin possible and who gave me the opportunity to work at high level in his very pleasant group. To Alberto, Edgar, Sne, Pawel,... for the nice time and moments in the PDI. Special thanks to Alberto who helped me very much and made my stay very delightful.

I would like to give thanks as well to all my colleagues in the basement offices. Alejandro, the fake murcian, for the jokes, parties and sport discussions, Jaime, Maribel, David, Mari Luz, Eleonora, Pedro (basquet superstar), Antonio, Maria José,...; Everton, for the nice but short time in Valencia and conferences; then, Rafa, Jesús, Josep for the coffee breaks and the lunch time discussions and Pascual and Julian for the help in

laboratory and the excellent mechanical work and, off course, for the splendid Friday morning almuerzos.

Luis and Justino, the Brazilian theoreticians, who made the time very amusing during their sojourn in Valencia, for their collaboration in this work.

I thank very much my parents for the support and patience during my academic studies over the last 12 (!! sounds as it is, long!!) years, my uncle for the support, especially in the beginning of my studies, my sister and rest of my family for the motivation all that time.

Finally, I would like to thank Elena who accompanied me almost the whole period in Valencia and who supported, motivated and sticked by me in good and hard times.

Thank you    Gracias    Danke    Obrigado    Gràcies